Convective Heat Flux Sensor Validation, Qualification and Integration in Test Articles

Brian Edward Earp

Dissertation submitted to the faculty of the Virginia Polytechnic Institute and State University in partial fulfillment of the requirements for the degree of

Doctor of Philosophy
In
Aerospace Engineering

Joseph A. Schetz, Chair
William J. Devenport
K. Todd Lowe
August J. Rolling
Charles F. Wisniewski

August 8th, 2012
Blacksburg, VA

Keywords: Heat Flux, Thermal Instrumentation, Heat Transfer, Schmidt-Boelter, Inverse Heat Flux

Convective Heat Flux Sensor Validation, Qualification and Integration in Test Articles

Brian Edward Earp

ABSTRACT

The purpose of this study is to quantify the effects of heat flux sensor design and interaction with both test article material choice and geometry on heat flux measurements. It is the public domain component of a larger study documenting issues inherent in heat flux measurement. Direct and indirect heat flux measurement techniques were tested in three thermally diverse model materials at the same Mach 6 test condition, with a total pressure of 1200 psi and total temperature of 1188° R, and compared to the steady analytic Fay-Riddell solution for the stagnation heat flux on a hemisphere. A 1/8 in. fast response Schmidt-Boelter gage and a 1/16 in. Coaxial thermocouple mounted in ¾ in. diameter stainless steel, MACOR, and Graphite hemispheres were chosen as the test articles for this study. An inverse heat flux calculation was performed using the coaxial thermocouple temperature data for comparison with the Schmidt-Boelter gage. Before wind tunnel testing, the model/sensor combinations were tested in a radiative heat flux calibration rig at known static and dynamic heat fluxes from 1 to 20 BTU/ft^2/s. During wind tunnel testing, the chosen conditions yielded stagnation point convective heat flux of 15-60 BTU/ft^2/s, depending on the stagnation point wall temperature of the model. A computational fluid dynamic study with conjugate heat transfer was also undertaken to further study the complex mechanisms at work. The overall study yielded complex results that prove classic methodology for inverse heat flux calculation and direct heat flux measurement require more knowledge of the thermal environment than a simple match of material properties. Internal and external model geometry, spatial and temporal variations of the heat flux, and the level of thermal contact between the

sensor and the test article can all result in a calculated or measured heat flux that is not correct even with a thermally matched sensor. The results of this study supported the conclusions of many previous studies but also examined the complex physics involved across heat flux measurement techniques using new tools, and some general guidance for heat flux sensor design and use, and suggestions for further research are provided.

Acknowledgements

I would like to thank Dr. Schetz for all of the help, advice, and patience during my time at Virginia Tech. I would not have made it here without him. My committee has been invaluable in both information and time, and my defense would not have been possible without Dr. Wisniewski stepping in for Lt Col Rolling. The generous monetary and informational support from AEDC, specifically the folks in the ATM Lab, Dr. John Adams and Mr. Wayne Hawkins, made many of the results and testing possible. The computational portion of my work was only completed with the help of Dr. Reese Neel, and for his help, I am quite thankful. There were quite a few occasions when many pieces of this puzzle would not have gone together without the help of my family living in Kentucky, even at their own expense. Lastly, not enough can be said about the love, support, and patience of my wife. Not only did she make sure everything ran smoothly with my mind elsewhere, she brought our two children into the world during this time and managed to make it all look easy. Only with her help, and the two kids understanding that their father is always working and will someday finish, could I have finished the task at hand.

Table of Contents

Acknowledgements ..... **iv**

List of Figures ..... **viii**

List of Tables ..... **xv**

Nomenclature ..... **xvii**

1. Introduction ..... **- 1 -**

1.1 Heat Flux ..... - 1 -

1.1.1 Heat Flux Measurement ..... *- 3 -*

1.2 Heat Flux Measurement Background ..... - 5 -

1.2.1 Direct Measurement ..... *- 6 -*

1.2.2 Indirect Measurement ..... *- 11 -*

1.3 Measurement Study ..... - 15 -

2. Experimental Facilities and Methods ..... **- 19 -**

2.1 Virginia Tech Hypersonic Wind Tunnel ..... - 19 -

2.2 Experimental Set-up ..... - 21 -

2.3 Experimental Uncertainty ..... - 26 -

2.4 Imperfect Gas Effects ..... - 28 -

2.4.1 Imperfect Gas Analytic Method ..... *- 29 -*

2.4.2 Imperfect Gas Results ..... *- 31 -*

2.4.3 Imperfect Gas Conclusions ..... *- 33 -*

2.2 AEDC ATM LAB Calibration Set-up ..... - 34 -

3. Computational and Analytic Methods ..... **- 36 -**

3.1 Computational Method ..... - 36 -

3.2 Analytic Method ..... - 41 -

4. Experimental Results ..... **- 42 -**

4.1 Calibration Results ..... - 42 -

4.1.1 Steady-State Calibration Results ..... *- 43 -*
4.1.2 Dynamic Calibration Results ..... *- 44 -*
4.2 Wind Tunnel Results ..... - 51 -
4.2.1 Coaxial Thermocouple Results ..... *- 56 -*
4.2.2 Fast Response Schmidt-Boelter Gage Results ..... *- 64 -*
4.3 Model Material Comparisons ..... - 67 -
4.3.1 Stainless Steel Hemisphere Model ..... *- 67 -*
4.3.2 Graphite Hemisphere Model ..... *- 69 -*
4.3.3 MACOR® Hemisphere Model ..... *- 71 -*
5. Computational Results ..... - 74 -
5.1 Coaxial Thermocouple Surrogate ..... - 74 -
5.2 Fast Response Schmidt-Boelter Gage Surrogate ..... - 80 -
5.3 Fiber Optic Thermocouple Surrogate ..... - 88 -
5.4 Perfect Sensor ..... - 93 -
6. Experimental and Computational Results Comparison ..... - 99 -
6.1 Stainless Steel Hemisphere Comparison ..... - 100 -
6.2 MACOR® Hemisphere Comparison ..... - 102 -
6.3 Graphite Hemisphere Comparison ..... - 105 -
7. Discussion ..... - 108 -
7.1 Results ..... - 108 -
8. Conclusions ..... - 117 -
8.1 Future Work ..... - 118 -
A. Appendix A: Uncertainty Analysis ..... - 120 -
A.1 Flow Conditions Uncertainty ..... - 122 -
A.2 Inverse Method Heat Flux Prediction Uncertainty ..... - 124 -
A.2.1 Inverse Heat Flux Data Reduction Code Validation ..... *- 125 -*
A.3 Fay-Riddell Analytic Calculation Uncertainty ..... - 126 -

A.4 Heat Flux Measurement Uncertainty ..... - 127 -
References ..... - 129 -

List of Figures

Figure 1-1. Simple Diagram of a Schmidt-Boelter gage. Fig. 1. Concept sketch of Schmidt-Boelter gage. Source: C. T. Kidd and J. C. Adams, "Development of a Heat-Flux Sensor for Commonality of Measurement in AEDC Hypersonic Wind Tunnels," in AIAA Paper No. 2000-2514, 2000, pg. 4[5]. Used under fair use guidelines, 2012. ..... - 6 -
Figure 1-2. Actual fast-response Schmidt-Boelter gage mounted in the stainless steel hemisphere. ..... - 7 -
Figure 1-3. Comparison between the indicated and corrected heat flux for a Schmidt-Boelter gage mounted in MACOR during a Mach 6 test in the Virginia Tech Hypersonic wind tunnel. ..... - 9 -
Figure 1-4. Simple Gardon gage illustration. ..... - 10 -
Figure 1-5. Simple Thermocouple sketch[31]. ..... - 11 -
Figure 1-6. Illustration of a MedTherm Coaxial thermocouple with rear temperature measurement. ..... - 12 -
Figure 1-7. Slug calorimeter sketch. ..... - 13 -
Figure 1-8. Null-point calorimeter sketch. ..... - 14 -
Figure 2-1. Virginia Tech Hypersonic Wind Tunnel. Public Domain. ..... - 19 -
Figure 2-2. Drawing of the VTHST M = 6 Nozzle. Public Domain. ..... - 20 -
Figure 2-3. Reynolds number ranges in the VTHST. ..... - 21 -
Figure 2-4. Experimental Hemisphere model designs for all materials. ..... - 22 -
Figure 2-5. VTHST test fixture with the MACOR® hemisphere/MedTherm Coaxial Thermocouple mounted including pitot and total temperature probes. - 23 -
Figure 2-6. Lay-out of the VTHST including mounting of the test fixture in the tunnel. ..... - 23 -

Figure 2-7. Plot of plenum pressure and stagnation pressure behind the shock for a typical run at Mach 6 in the VTHST. ..... - 25 -
Figure 2-8. Shadow graph of the flow around the hemisphere for a typical run at Mach 6 in the VTHST. ..... - 26 -
Figure 2-9. Uncertainty of the freestream Mach number and total pressure ratio during the VTHST run. ..... - 27 -
Figure 2-10. Gamma changes with Temperature[35]. ..... - 30 -
Figure 2-11. Fay Riddell Quasi-Steady Heat Flux Changes with Imperfect Gas Effects, $M_\infty = 6$ p_0=1200 psi, T_0=1188° R. ..... - 33 -
Figure 2-12. Schematic of the Radiant Heat Flux Calibration Facility at the ATM Lab. ..... - 34 -
Figure 2-13. Calibration test fixture at the ATM Lab. ..... - 35 -
Figure 3-1. Refined grid for CFD Study. ..... - 39 -
Figure 4-1. Temperature results for all materials during calibration at 12 BTU/ft^2/s. ..... - 45 -
Figure 4-2. Inverse heat flux results for all materials during calibration at 12 BTU/ft^2/s. ..... - 46 -
Figure 4-3. Temperature results for all the coaxial type E thermocouple in stainless steel at various heat flux settings. ..... - 47 -
Figure 4-4. Comparison of Inverse Heat Flux methods for the coaxial thermocouple in the stainless hemisphere at 12 BTU/ft^2/s. ..... - 48 -
Figure 4-5. Changes in the geometry and assumptions between inverse heat flux methods and the VTHST. ..... - 49 -
Figure 4-6. Possible external movement of thermal energy from the hemisphere.... - 50 -
Figure 4-7. Spherical and Planar inverse heat flux method comparison for the MedTherm coaxial thermocouple in a stainless steel hemisphere. ..... - 53 -

Figure 4-8. Spherical and Planar, Semi-infinite and finite inverse heat flux method comparison for the MedTherm coaxial thermocouple in a stainless steel hemisphere. ..... - 55 -
Figure 4-9. Coaxial thermocouple temperature comparison across different model materials. ..... - 57 -
Figure 4-10. Coaxial thermocouple heat flux comparison across different model materials. ..... - 58 -
Figure 4-11. FFT of the front and rear temperature for the MedTherm coaxial thermocouple in the stainless steel hemisphere. ..... - 59 -
Figure 4-12. FFT of the front and rear temperature for the MedTherm coaxial thermocouple in the MACOR® hemisphere. ..... - 60 -
Figure 4-13. FFTs of the front temperature data for the MedTherm coaxial thermocouples in the MACOR®, Stainless, and Graphite hemispheres. ..... - 61 -
Figure 4-14. FFTs of the coaxial thermocouple in the stainless steel hemisphere, the pitot tube transducer, and the total temperature probe thermocouple. ..... - 63 -
Figure 4-15. Schmidt-Boelter gage heat flux comparison across different model materials. ..... - 65 -
Figure 4-16. Schmidt-Boelter gage temperature comparison across different model materials. ..... - 66 -
Figure 4-17. Stainless steel model temperature comparison. ..... - 68 -
Figure 4-18. Stainless steel model heat flux comparison. ..... - 69 -
Figure 4-19. Graphite model temperature comparison. ..... - 70 -
Figure 4-20. Graphite model heat flux comparison. ..... - 71 -
Figure 4-21. MACOR® model temperature comparison. ..... - 72 -
Figure 4-22. MACOR® model heat flux comparison. ..... - 73 -
Figure 5-1. Simulated Mach 6 wind tunnel run temperature profile for a modeled chromel sensor with different model materials ..... - 75 -

Figure 5-2. Simulated Mach 6 wind tunnel run heat flux profile for a modeled chromel sensor with different model materials.....- 76 -
Figure 5-3. Temperature and Mach contours at t = 0.5, 1, 1.5, and 2 sec. for a Simulated Mach 6 wind tunnel run with a modeled chromel thermocouple in a stainless steel hemisphere. .....- 77 -
Figure 5-4. Temperature and Mach contours at t = 0.5, 1, 1.5, and 2 sec. for a Simulated Mach 6 wind tunnel run with a modeled chromel thermocouple in a MACOR® hemisphere. .....- 78 -
Figure 5-5. Temperature and Mach contours at t = 0.5, 1, 1.5, and 2 sec. for a Simulated Mach 6 wind tunnel run with a modeled chromel thermocouple in a Graphite hemisphere. .....- 80 -
Figure 5-6. Simulated Mach 6 wind tunnel run temperature profile for a modeled Schmidt-Boelter gage with different model materials.....- 81 -
Figure 5-7. Simulated Mach 6 wind tunnel run heat flux profile for a modeled Schmidt-Boelter gage with different model materials.....- 82 -
Figure 5-8. Temperature and Mach contours at t = 0.5, 1, 1.5, and 2 sec. for a Simulated Mach 6 wind tunnel run with a modeled Schmidt-Boelter gage in a stainless steel hemisphere. .....- 84 -
Figure 5-9. Temperature and Mach contours at t = 0.5, 1, 1.5, and 2 sec. for a Simulated Mach 6 wind tunnel run with a modeled Schmidt-Boelter gage in a MACOR® hemisphere. .....- 86 -
Figure 5-10. Temperature and Mach contours at t = 0.5, 1, 1.5, and 2 sec. for a Simulated Mach 6 wind tunnel run with a modeled Schmidt-Boelter gage in a Graphite hemisphere. .....- 87 -
Figure 5-11. Simulated Mach 6 Wind Tunnel Run temperature profile for a silica fiber with different model materials. .....- 88 -

Figure 5-12. Simulated Mach 6 Wind Tunnel Run heat flux profile for a silica fiber with different model materials. ..... - 89 -
Figure 5-13. Temperature and Mach contours at t = 0.5, 1, 1.5, and 2 sec. for a Simulated Mach 6 wind tunnel run with a silica fiber in a stainless steel hemisphere. ..... - 90 -
Figure 5-14. Temperature and Mach contours at t = 0.5, 1, 1.5, and 2 sec. for a Simulated Mach 6 wind tunnel run with a silica fiber in a MACOR® hemisphere.. - 91 -
Figure 5-15. Temperature and Mach contours at t = 0.5, 1, 1.5, and 2 sec. for a Simulated Mach 6 wind tunnel run with a silica fiber in a Graphite hemisphere. - 93 -
Figure 5-16. Simulated Mach 6 Wind Tunnel Run temperature profile for a perfect sensor with different model materials. ..... - 94 -
Figure 5-17. Simulated Mach 6 Wind Tunnel Run heat flux profile for a perfect sensor with different model materials. ..... - 95 -
Figure 5-18. Temperature and Mach contours at t = 0.5, 1, 1.5, and 2 sec. for a Simulated Mach 6 wind tunnel run with a stainless steel sensor in a stainless steel hemisphere. ..... - 96 -
Figure 5-19. Temperature and Mach contours at t = 0.5, 1, 1.5, and 2 sec. for a Simulated Mach 6 wind tunnel run with a MACOR® sensor in a MACOR® hemisphere. ..... - 97 -
Figure 5-20. Temperature and Mach contours at t = 0.5, 1, 1.5, and 2 sec. for a Simulated Mach 6 wind tunnel run with a Graphite sensor in a Graphite hemisphere. ..... - 98 -
Figure 6-1. Stainless steel model temperature comparison VTHST to CFD with CHT. ..... - 101 -

Figure 6-2. Stainless steel model heat flux comparison VTHST to CFD with CHT.- 102 -
Figure 6-3. MACOR® model temperature comparison VTHST to CFD with CHT.- 103 -
Figure 6-4. MACOR® model heat flux comparison VTHST to CFD with CHT..... - 104 -
Figure 6-5. Graphite model temperature comparison VTHST to CFD with CHT.... - 106 -
Figure 6-6. Graphite model heat flux comparison VTHST to CFD with CHT.. - 107 -
Figure 7-1. Schmidt-Boelter gage heat flux comparison across different model materials. .....- 109 -
Figure 7-2. Schmidt-Boelter gage temperature comparison across different model materials. .....- 110 -
Figure 7-3. Temperature results for all materials during calibration at 12 BTU/ft^2/s. .....- 112 -
Figure 7-4. Spherical and Planar, Semi-infinite and finite inverse heat flux method comparison for the MedTherm coaxial thermocouple in a stainless steel hemisphere. .....- 113 -
Figure 7-5. Coaxial thermocouple heat flux comparison across different model materials. .....- 114 -
Figure 7-6. Coaxial thermocouple temperature comparison across different model materials. .....- 114 -
Figure 7-7. Simulated Mach 6 wind tunnel run heat flux profile for a modeled Schmidt-Boelter gage with different model materials. .....- 116 -
Figure A-1. Uncertainty of Flow properties during a VTHST Run at M = 6...- 124 -
Figure A-2. Inverse Heat Flux Code Validation Plot. .....- 126 -

Figure A-3. Uncertainty in the heat flux data and calculations for the stainless steel hemispheres.....- 128 -

List of Tables

Table 1-1. Material Thermodynamic Properties. ..... - 17 -
Table 2-1. VTHST Flow Property variations. ..... - 20 -
Table 2-2. Summary of the uncertainty for this study from Appendix A. ..... - 28 -
Table 2-3. Flow properties upstream and downstream of a normal shock at test conditions assuming a thermally and calorically perfect gas with γ=1.4. ..... - 31 -
Table 2-4. Flow properties upstream and downstream of a normal shock at test conditions assuming a thermally and calorically perfect gas with γ=1.3689. ..... - 31 -
Table 2-5. Flow properties upstream and downstream of a normal shock at test conditions assuming a thermally perfect and calorically imperfect gas with γ=1.3689. ..... - 32 -
Table 2-6. Percentage change in flow properties between perfect gas and imperfect gas assumptions ..... - 32 -
Table 3-1. Properties of the materials used in the CFD Simulations. ..... - 40 -
Table 4-1. Results for Schmidt-Boelter gages in all materials during static calibration at 3 and 12 BTU/ft^2/s. ..... - 43 -
Table 4-2. The time constants for the three Schmidt-Boelter gages in their hemispheres. ..... - 49 -
Table 4-3. Temperature and calculated inverse heat flux comparison between dynamic calibrations of a temperature sensor mounted in MACOR® sitting in a stainless steel block and a MACOR® block. ..... - 51 -
Table 4-4. VTHST flow conditions for this study. ..... - 51 -
Table 4-5. Percentage of the energy that is the apparent noise. ..... - 64 -
Table 7-1. Results for Schmidt-Boelter gages in all materials during static calibration at 3 and 12 BTU/ft^2/s. ..... - 111 -
Table A-1. Sensors used in the VTHST. ..... - 120 -

Table A-2. Average uncertainty calculated for this study. .....- 122 -
Table A-3. Calculated uncertainties for this study. .....- 128 -

Nomenclature

Symbol	Meaning
α	= thermal diffusivity
ε	= surface emissivity
κ	= local velocity gradient
ρ	= density
τ	= time constant
τ^*	= characteristic time measure of the integrated energy deficiency inherent in the gage response
μ	= dynamic viscosity
σ	= Stefan-Boltzmann constant
a	= thermal diffusivity
b	= molecular-size constant
c	= intermolecular-force constant
c_p	= specific heat at constant pressure
c_v	= specific heat at constant volume
D	= hemisphere diameter
G	= tunnel mass flow rate
h	= specific enthalpy or heat transfer coefficient
k	= thermal conductivity
M	= Mach number
m	= mass
p	= pressure
Pr	= Prandtl number
q	= dynamic pressure

q'' = wall heat flux

r = hemisphere radius

Re = Reynolds number

T = temperature

t = time

u = specific internal energy

V = freestream

v = specific volume

x = dimension

Subscripts

Symbol	Meaning
0	= total/stagnation property
1	= property in front of a shock
2	= property in front of a shock
∞	= freestream property
e	= property at the edge of the boundary layer
max	= maximum tunnel condition
min	= minimum tunnel condition
r	= reference conditions
s	= surface condition
surr	= surrounding condition
w	= property at the wall

1. Introduction

Throughout their flight profiles, both air and aerospace vehicles experience high thermal energy transfer into many of their components. The transfer of thermal energy is referred to as "heat transfer", and it is the rate of this transfer, divided by the area of transfer, that is known as "heat flux", q_w''[1]. By studying heat flux on components, as opposed to simply the temperature, it is possible to predict future temperatures and conditions because heat flux is a measurement of energy flux. High heat flux drives the design and life-cycle of the high-speed and high-temperature test and flight community within the aerospace world, as well as the component development by aerospace propulsion engineers. The high heat flux present in the hypersonic regime drives material choice, flight regime, and the fatigue cycle of many parts. It can also be the cause of failure, minor or catastrophic, predicted or not. Because of this, aerospace engineers desire the ability to predict and monitor the heat flux environment present on various components in their system. Knowledge of the heat flux environment allows the engineer to choose the proper material at each location on the system, predict the necessity of active or passive cooling, determine the flight envelope, determine maintenance schedule, document and monitor the thermal management system on the vehicle, and most of all, try to prevent the catastrophic failure of the system. The purpose of this study is to quantify the effects of heat flux sensor design and interaction with both test article material choice and geometry on heat flux measurements.

1.1 Heat Flux

The primary principle that defines heat flux is the first law of thermodynamics which that states energy must be conserved. There are three ways that thermal energy can be transferred. Those three "modes" of thermal energy transfer are convection, radiation, and conduction[2].

Conduction is "heat transfer through stationary materials by electrons and phonons"[1]. The transfer of thermal energy always occurs from regions of high temperature to regions of low temperature and is in fact driven by random molecular motion[2]. Equation 1.1 is known as Fourier's Law of thermal conduction. If it is determined that the conduction is only taking place in one-dimension, an assumption known as 1-D, equation 1.1 can be simplified to equation 1.2.

$$q^{"}_{conduction} = -k\nabla T \tag{1.1}$$

$$q^{"}_{conduction} = -k\frac{\partial \mathrm{T}}{\partial \mathrm{x}} \tag{1.2}$$

In equation 1.1, ∇, is an operator that is used to specify the partial derivative of temperature in each direction. In equations 1.1 and 1.2, *k* is the thermal conductivity of the medium. Conduction can take place within any medium, solid or fluid, or between media, with the only requirement being a difference in temperatures. If the medium is, or media are, at uniform temperature heat transfer due to conduction will be zero. As the temperature difference increase, so does heat transfer by conduction.

Convection is the transfer of thermal energy, generally from a fluid to another medium, due to the relative motion and temperature mismatch between the two media. It is in fact a combination of "conduction and bulk fluid motion"[2]. Convection can only occur if there is motion and a temperature difference between the fluid and the second medium. The heat transfer due to convection increases as the velocity increases and/or the temperature difference increases. The equation for heat flux due to convection is defined by Newton's law of cooling, but modified due to the kinetic energy that is dissipated in the boundary layer of high-speed flow[3].

$$q^{"}_{convection} = h(T_s - T_{aw}) \tag{1.3}$$

In equation 1.3, *h* is the heat transfer coefficient which depends on the geometry of the convection problem, the properties of the fluid flow in the problem, and the thermal

properties of the fluid itself[2]. The two temperatures are the temperature of the surface, T_s, and the adiabatic wall temperature, T_{aw}.

Radiation is the transfer of thermal energy simply due to a difference in temperature. It differs from conduction in that there does not have to be a second solid or fluid present for the transfer from the environment to the medium to occur[1]. Equation 1.4 is the heat flux due to radiation from a very "large enclosure" to a small medium or object[2].

$$q^{"}_{radiation} = \varepsilon\sigma({T_s}^4 - {T_{surr}}^4) \tag{1.4}$$

ε is the emissivity of the surroundings and is assumed to be the same as the absorbtivity of the medium/object[2]. σ is the Stefan-Boltzmann constant and the subscripts *S* and *surr* refer to the properties of the surface of the medium/object and the "large enclosure".

From the first law of thermodynamics and the knowledge of the three modes of heat transfer, the basic equation of heat flux is derived as shown by Diller[1].

$$m\, c_p \frac{\partial T}{\partial t} = q_{convection} + q_{radiation} + q_{conduction} \tag{1.5}$$

In studying heat transfer, the heat flux on the surface is the quantity that is most useful. By the 1st law, heat flux on the surface in the fluid is equal to the heat flux on the surface in the solid of interest. In equation 1.5 it is important to note that the rate of temperature change is affected by the combination of the mass and specific heat, m and c_p, of the system. This effect is not trivial, creating a delay in thermal changes to the system and is known as the "thermal capacitance" of the system[1].

1.1.1 Heat Flux Measurement

The two methods for measuring convective heat flux involve variations and simplifications of equation 1.1[1]. In the first method, sometimes called the direct method, all transfer within the material is assumed to be via conduction and a difference

between two temperatures is measured along with knowledge of the distance between the two temperatures and the thermal conductivity of the solid. For this method to be accurate, the conduction must be assumed to be 1-D, the heat flux must be steady, and the thermal conductivity and the distance must be accurately known or the sensor must be calibrated [1]. Equation 1.6 is the equation defining this method.

$$q_w{}'' = -k\frac{(T_1 - T_2)}{\delta} \tag{1.6}$$

δ is the distance between the two temperature measurements, where T_1 is a measurement closer to the surface, and T_2 is deeper into the material. For unsteady heat flux measurements equation 1.6 must be modified to account for the lag due to the lumped capacitance of the sensor[4],[5].

In the second method, a transient temperature on the surface of the test article is used to calculate the heat flux on the surface. This technique is generally called an inverse method. To accomplish this calculation, equation 1.5 is combined with equation 1.7 which is the conduction equation for materials that can be assumed to be homogeneous with constant properties[1].

$$\frac{\partial T}{\partial t} = a\nabla T \tag{1.7}$$

In this equation, a is the thermal diffusivity of the test article. The least complicated calculation for heat flux requires assuming that the conduction is taking place in one-dimension. Cook and Felderman developed equation 1.8 for a fixed time step to solve for a transient heat flux based on a transient wall temperature in 1966[6]. Care must be taken, since the inverse method is ill-posed mathematically.

$$q_w{}''(t_n) = 2\sqrt{\frac{k\rho c_p}{\pi \Delta t}}\sum_{i=1}^{n}\frac{T_i - T_{i-1}}{\sqrt{n-i}+\sqrt{n+1-j}} \tag{1.8}$$

The results from equation 1.8 can be problematic and many researchers have investigated modifications or other methods for calculating a transient heat flux from a transient wall

temperature as summarized by Seymour[7] and Walker and Scott[8]. The inverse technique used in this study was developed by Walker in 1995[9].

The method developed by Walker and Scott[9] is called the "Simple-Inverse Method". This method is very stable with less induced noise compared to other inverse methods[8].

The "Simple-Inverse Method" assumes a semi-infinite substrate[9]. Depending on the thickness and thermal diffusivity of the material chosen for a test, this may or may not be a valid assumption. Diller offered equation 1.9 in reference [1] as a quick method for checking when the error on the inverse heat flux calculation assuming semi-infinite will be greater than 1%.

$$t = 0.3\frac{\delta^2}{a} \tag{1.9}$$

Where δ is the thickness of the material and a is the thermal diffusivity.

1.2 Heat Flux Measurement Background

The field has a rich prior literature, and much of it is summarized by Neumann, Neumann et. al., Diller, and Childs et. al. in many publications and books [1],[10],[11],[12],[13],[14],[15],[16],[17]. Many papers and publications have been written about both direct[4],[5],[18],[19],[20],[21],[22] and indirect [18],[23],[24],[25],[26],[27],[28],[29],[8],[9],[30] heat flux measurement techniques and their problems. There are many cases where measurements were later found to be subject to large errors due to the problems involved in measuring heat flux[11]. The many problems with material choice, sensor type, assumptions, and geometry in the measurement of heat flux are summarized thoroughly by Neumann and Neumann et. al.[11],[12]. In Table 34.1 of the Heat Flux chapter from The Measurement, Instrumentation and Sensors Handbook , Diller covers the range of direct and indirect heat flux sensors available or in research[1].

1.2.1 Direct Measurement

In this study, the direct sensor of choice is the well-known Schmidt-Boelter gage which is based on equation 1.6. A Schmidt-Boelter gage consists of a wire wound around a thermal insulator and another metal in order to create a thermopile measuring the difference between the front and rear junctions[5]. This concept is show in Figure 1-1 and a picture of one of the fast response Schmidt-Boelter gages used in this study is shown in Figure 1-2.

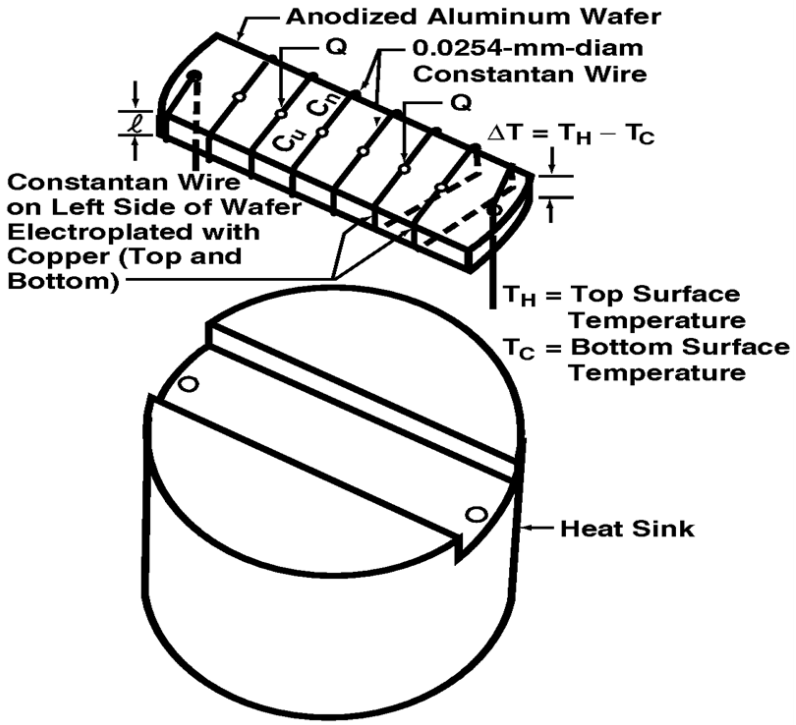

Figure 1-1. Simple Diagram of a Schmidt-Boelter gage. Fig. 1. Concept sketch of Schmidt-Boelter gage. Source: C. T. Kidd and J. C. Adams, "Development of a Heat-Flux Sensor for Commonality of Measurement in AEDC Hypersonic Wind Tunnels," in AIAA Paper No. 2000-2514, 2000, pg. 4[5]. Used under fair use guidelines, 2012.

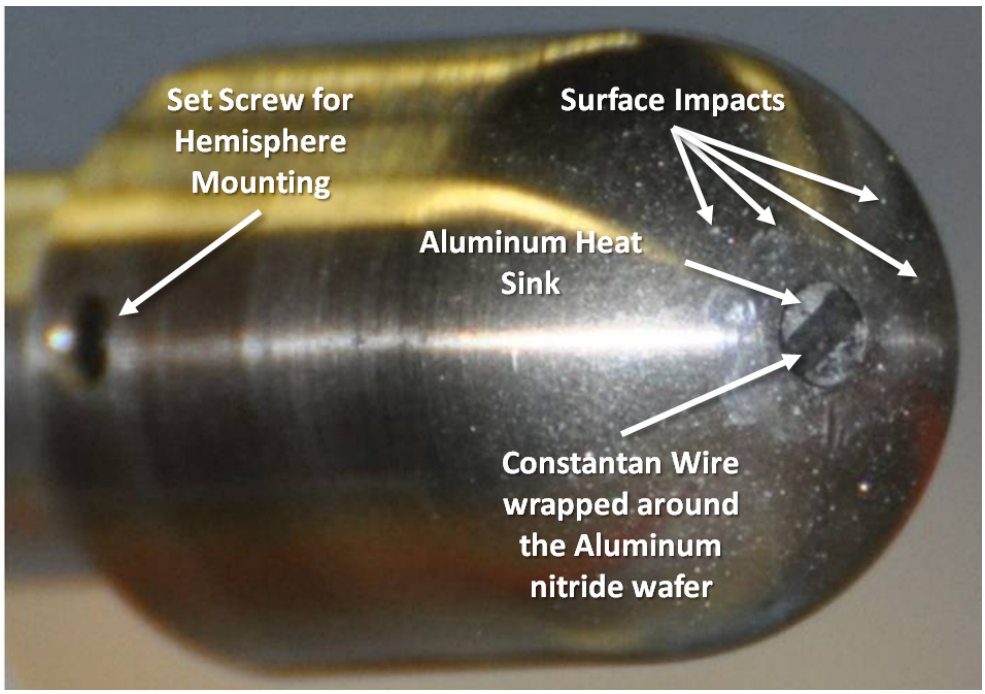

Figure 1-2. Actual fast-response Schmidt-Boelter gage mounted in the stainless steel hemisphere.

As documented in the simple sketch, the wire in most cases is made of Constantan and plated with Copper, and the wafer is anodized Aluminum. The actual sensors used in this study included Stycast 2782 Epoxy to hold the wire to the wafer, an Aluminum nitride wafer, and an air gap between the wire epoxy combination on the lower surface, and an Aluminum heat sink.

While equation 1.6 is the steady-state equation for the operation of an ideal Schmidt-Boelter gage, the actual sensor will be in a dynamic environment were the thermal capacitance of the sensor must be taken into account. Kidd and Adams developed a technique to use a calibration derived "characteristic time measure of the integrated energy deficiency inherent in the gage response", τ^*, to correct from measured heat flux to actual heat flux[5]. First the quantity R(t) is found which is a ratio between the measured heat flux and the applied heat flux as shown in equation 1.10.

$$R(t) = {q''_{w,meas}}/{q''_{w,input}} = 1 - e^{-({t}/{\tau})^n} \tag{1.10}$$

From there, τ^* can be solved by using equation 1.11 and an integration technique such as Newton shooting or Newton-Raphson method to find n[5].

$$\tau^* = \int_0^\infty (1 - R(t))\ dt = \frac{\tau}{n}\Gamma\left(\frac{1}{n}\right) \tag{1.11}$$

Once the characteristic time measure has been determined, equation 1.12 can be used to find the actual heat flux on the wall from the heat flux indicated by the Schmidt-Boelter sensor[5].

$$q''_{w,corr} = q''_{w,ind} + \tau^* \left({dq''_{w,ind}}/{dt} \right) \tag{1.12}$$

Figure 1-3 illustrates what the correction in equation 1.12 looks like on one of the wind tunnel runs in this study. The indicated heat flux is the solid black line and the dashed red is the corrected heat flux. The blue line is the percentage difference between the two. For this study, the indicated heat flux was within $^{+}/_{-}$ 5% throughout the on-condition wind tunnel run. The reason for the minor variation is that the heat flux is not varying rapidly during this wind tunnel run.

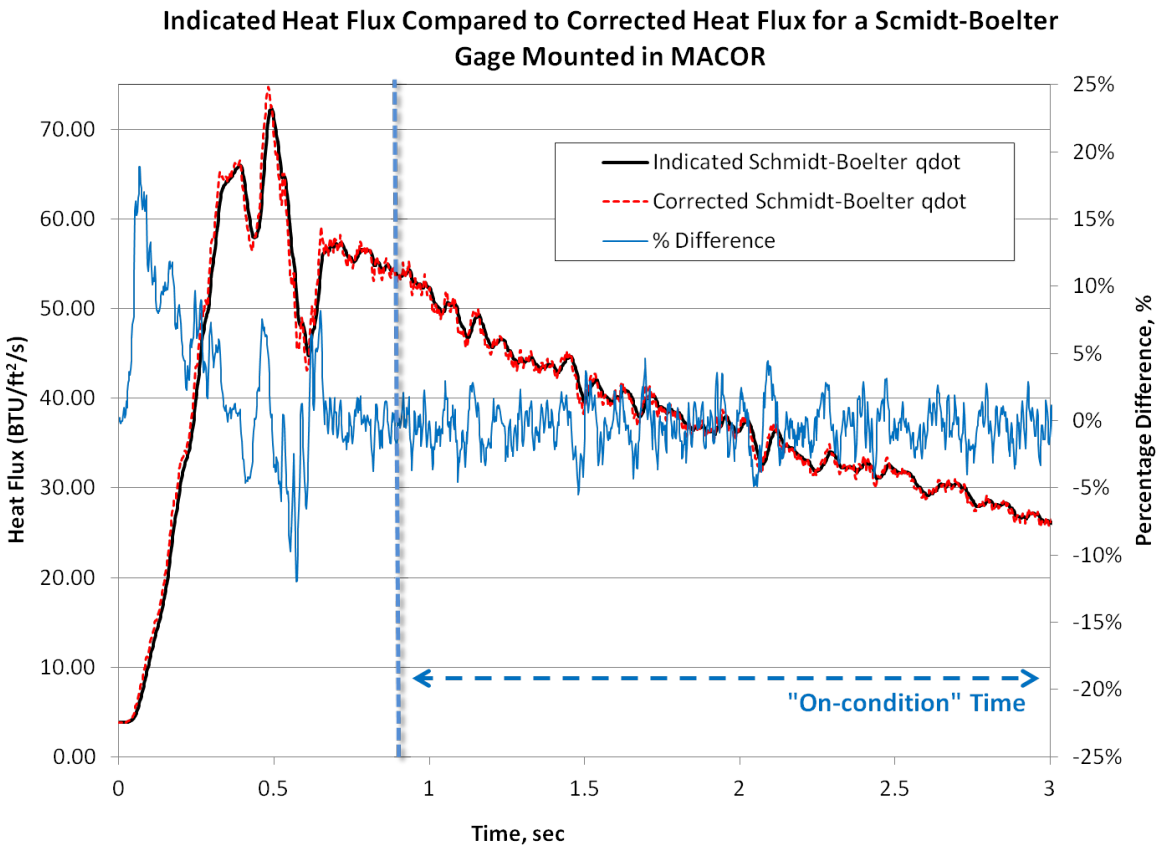

Figure 1-3. Comparison between the indicated and corrected heat flux for a Schmidt-Boelter gage mounted in MACOR during a Mach 6 test in the Virginia Tech Hypersonic wind tunnel.

A variation on the ideas employed in the Schmidt-Boelter gage is the microfoil heat flux sensor. In the microfoil sensors, alternating strips of 2 different metal foils are wrapped around an insulator and welded to form thermocouple junctions on either side[1],[11]. Similar to the Schmidt-Boelter gage, these junctions form 2 thermopiles, and the difference between these junctions provides the ΔT in equation 1.6. Also similar to the Schmidt-Boelter gage, this heat flux sensor must undergo static and dynamic calibration to determine the response to a steady heat flux, and the thermal capacitance of the sensor.

A range of micro-machined heat flux sensors have been studied and summarized by various researchers for high heat flux and temperature environments [21],[1]. They are created by using a sputtering technique to apply the conducting material as well as the

thermal insulator[1]. These sensors are generally very small and on the order of 2 μm thick which allows for rapid response to transients. They are also capable of measuring extremely high heat fluxes with temperature bounds above 1950° R [1].

A Gardon Gage is a circular foil based sensor that relies upon the difference in temperature between the center of the sensor where there is a junction between a thermocouple wire and constantan foil, and the outer edge of the sensor where there is a second junction between the constantan foil and a thermocouple wire[1]. Figure 1-4 illustrates the basic geometry of the Gardon gage.

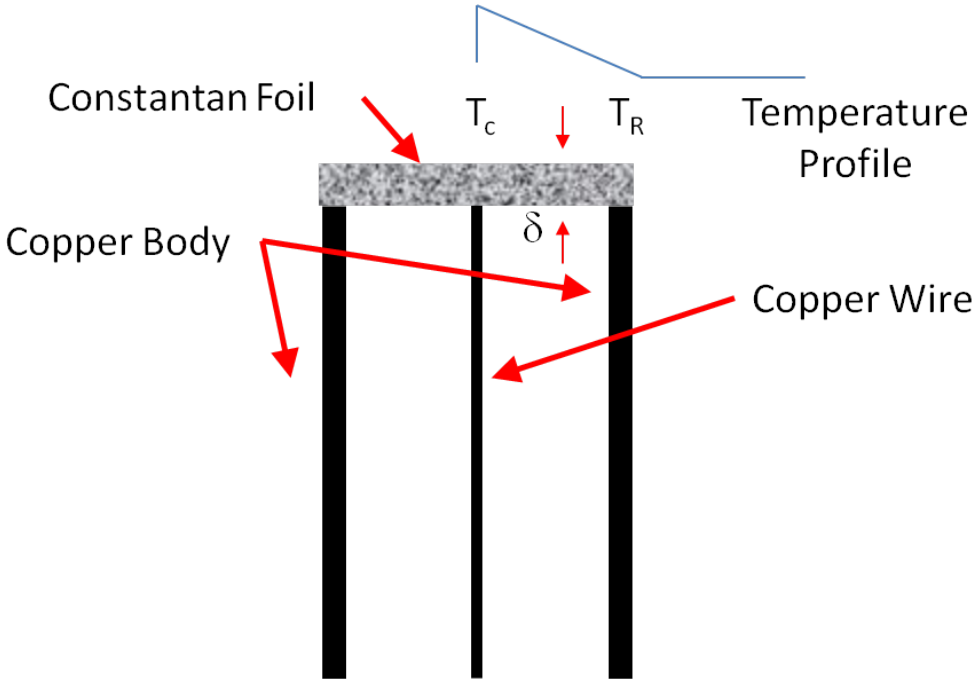

Figure 1-4. Simple Gardon gage illustration.

The Gardon gage is robust and simple in both construction and use[1]. The problems with this sensor are the relatively large size in reference to most measurement locations in the aerospace realm, the requirement of a cooled sensor for high heat flux which creates a temperature mismatch between the sensor and the surrounding material, and the requirement for a uniform radial temperature gradient which means this sensor provides erroneous readings in studies involving convective heat transfer due to flow asymmetries[1],[11].

1.2.2 Indirect Measurement

In this study, the indirect sensor of choice is the well-known Coaxial Thermocouple. The coaxial thermocouple has a long history of use for indirect heat flux studies [1],[8],[9],[10],[11],[12],[13],[18],[24]. Because the surface of the sensor can be sanded to be flush with a curved surface, the coaxial thermocouple is a common choice for leading edge and stagnation heat flux on small radii [10],[11],[12]. The coaxial thermocouple works on the same principles as a regular thermocouple, notably that if wires of two different metals are joined at two locations, the voltage can be measured as shown in Figure 1-5 and will vary with the difference in temperature between junction 1 and 2[31].

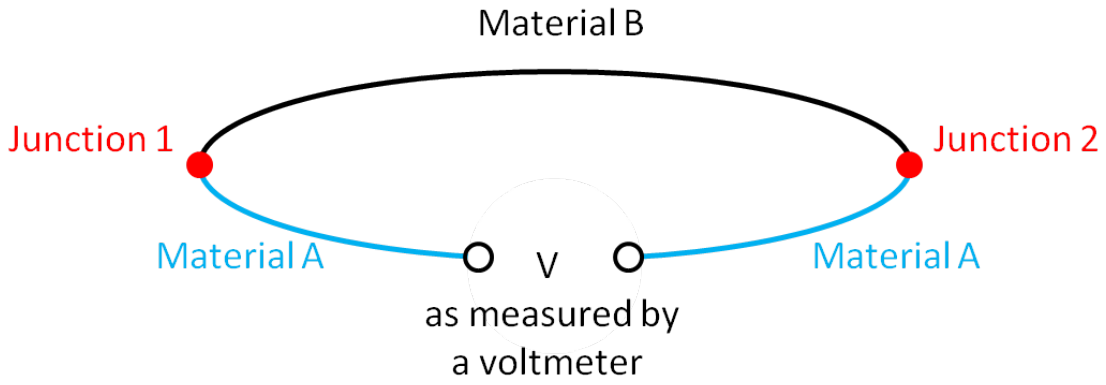

Figure 1-5. Simple Thermocouple sketch[31].

The coaxial thermocouple simply uses a metal wire in the middle that is surrounded by an insulator. Around that insulator a metal foil of a second type is wrapped[1]. Figure 1-6 is an illustration of a coaxial thermocouple partially created by MedTherm.

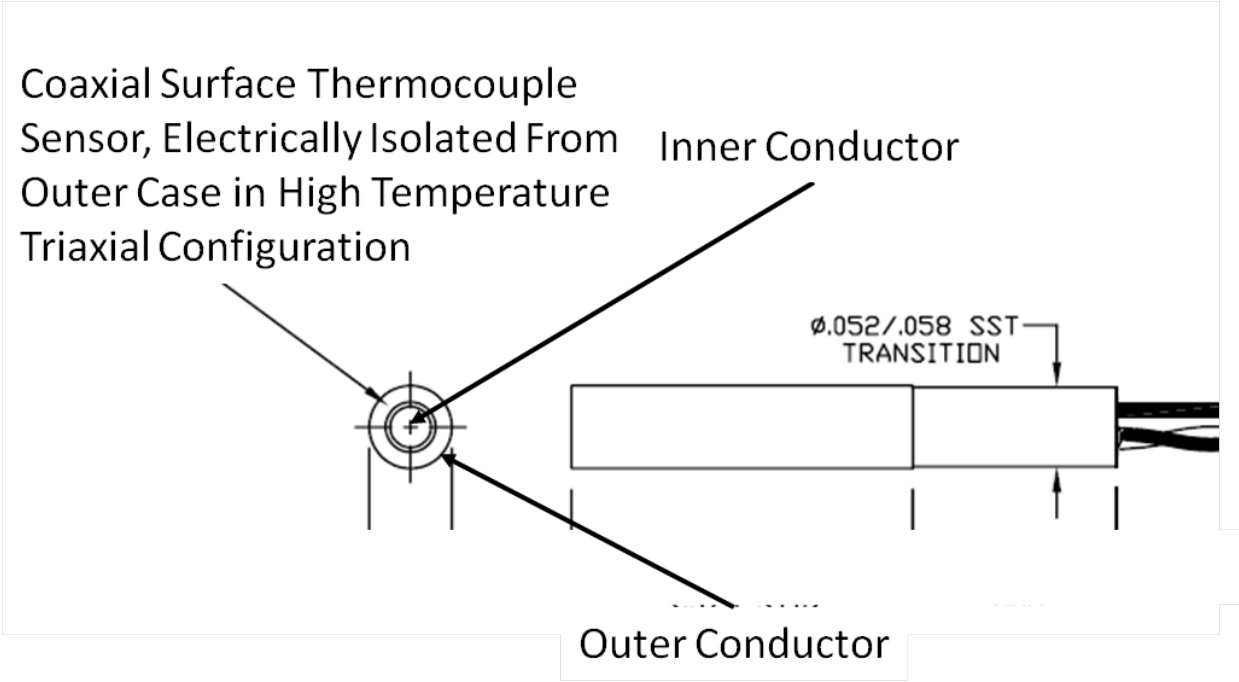

Figure 1-6. Illustration of a MedTherm Coaxial thermocouple with rear temperature measurement.

The thermocouple in this study was a $^{1}/_{16}$ in. MedTherm Type E Coaxial Thermocouple. This Type E coaxial thermocouple uses a Constantan center wire with a Chromel P sheath. In order to calculate a heat flux, method 2 from section 1.1.1 must be used. In this study, the "Simple Inverse Method" created by Walker and Scott in 1995[9] is used to calculate the transient wall heat flux from the transient wall temperature measurement. Verification of the Walker code was performed with two other inverse heat flux codes covered in references [32] and [18].

Another indirect measurement technique that many researchers[1],[10],[11][12],[13],[17],[23],[26],[22] have used in heat flux studies is the calorimeter, including the slug, null-point types, and thin-film types. The "calorimeter is a device for measuring the amount of absorbed thermal energy"[1]. The slug calorimeter, as shown in Figure 1-7, assumes that the "slug" of material will respond instantaneously so that the entire mass is only one temperature.

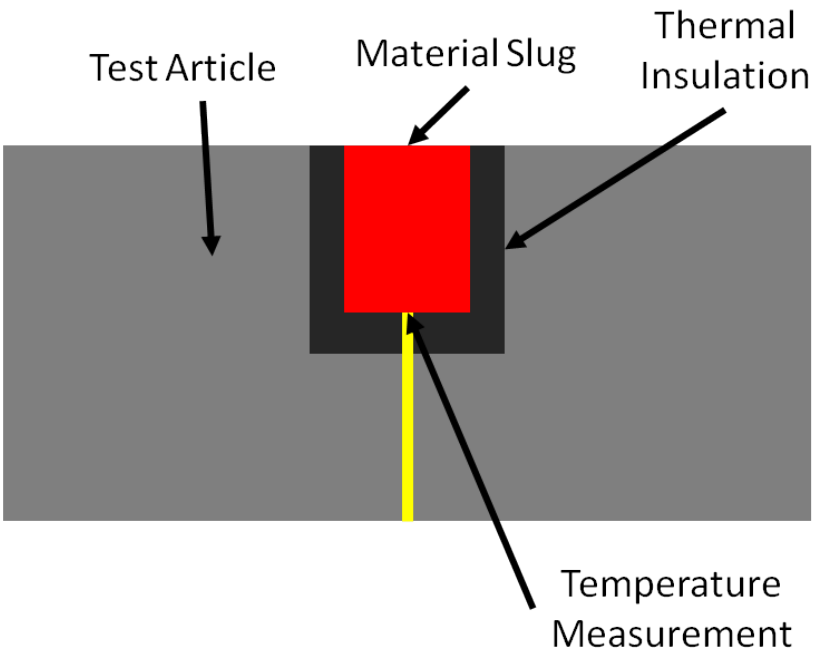

Figure 1-7. Slug calorimeter sketch.

Similar to equation 1.5, equation 1.13 is the basic equation for a slug calorimeter, and if the insulation is good, the losses can be near zero[31].

$$q_w{}^{"} = m\, c_p \frac{dT_m}{dt} - k_l \Delta T \tag{1.13}$$

Where T_m is the temperature of the slug and k_l is the loss coefficient and ΔT is the temperature difference between the test article and the slug[31]. The problem is that the response time on slug calorimeters is very slow[1]. For highly transient heat flux environments, this is a problem. To overcome this, the null-point calorimeter was created[11]. Figure 1-8 is a sketch of a null-point calorimeter.

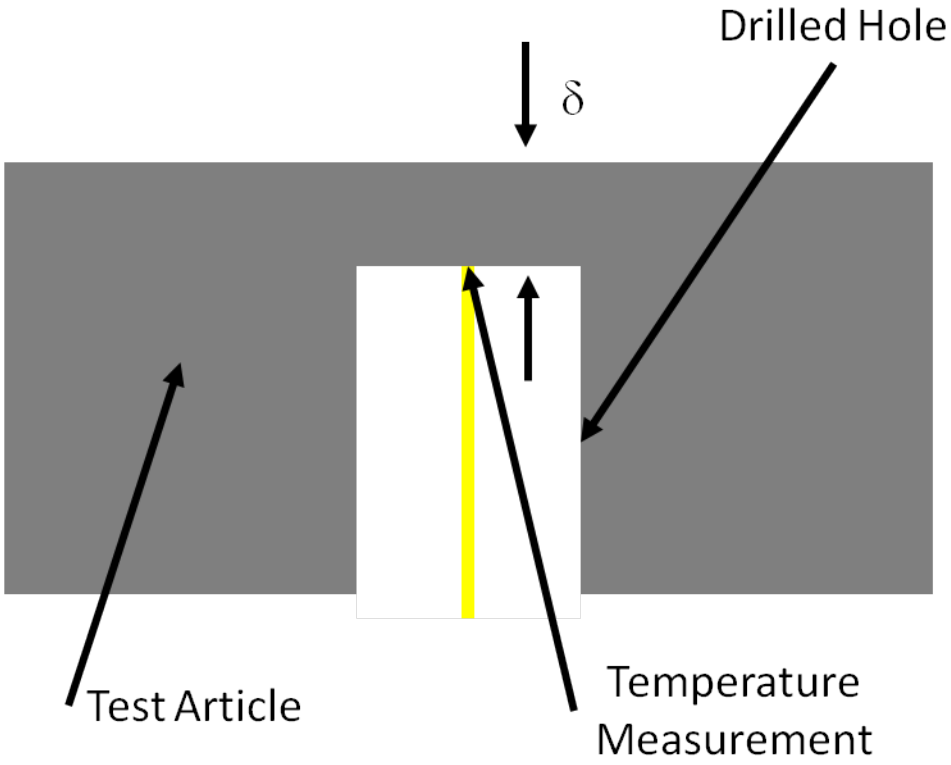

Figure 1-8. Null-point calorimeter sketch.

The null-point calorimeter is simply used with equation 1.6 to recover the wall temperature and then one of the many inverse methods is used to calculate transient[11],[22],[17],[23],[26]. A thin film calorimeter takes the above techniques and puts the temperature measurement behind a thin-film of known thermal properties and thickness. This film can coat the entire test article to give whole aircraft heat flux measurements[1],[13],[11].

A newer sensor that has shown promise in measuring temperature for indirect heat flux calculations is the fiber optic temperature sensor [25],[27],[28],[29],[30]. Fiber optic temperature sensors use the principle of extrinsic Fabry-Perot interferometry (EFPI) in order to measure temperature[25]. Light is transferred along the fiber and reflects off both the end of the fiber and the end of a sensor wafer fused to the end of the fiber. EFPI uses the pattern formed by these two reflections to measure the difference between them. As the sensor wafer expands or contracts and the index of refraction changes due to changes in

temperature, the reflected patterns change[25]. Precise calibration of these EFPI temperature devices can give uncertainties of less than 0.1° R and resolution of 0.01° R. Unfortunately calibration throughout the entire range of the sensor in 0.1° increments is time consuming and requires a calibration thermocouple that is more accurate than the desired uncertainty so the normal uncertainty is more like 1° R and could be as much as 9° R[29]. In the computational part of this study, a fiber optic temperature sensor was simulated. This sensor was included for the five potential positives it brings.

1. The possibility of very low uncertainty[29]
2. High temperature capability[30]
3. Very small
4. High data acquisition rate for good frequency resolution[25]
5. Extremely small response time[29]

1.3 Measurement Study

Since many troublesome issues have been identified for convective heat flux measurements in high-speed flows, this study was designed to address some of the main puzzles [1],[10],[11],[12],[13],[14],[15],[16],[17].

The issues present in heat flux measurement are material matching, test article scale and geometry, calibration, and installation. The issue with material matching is that a sensor with thermal properties different than the test article will affect the flow, and measure the heat flux present on the sensor itself, not the surface in which it is mounted. Test article scale and geometry is a problem because hypersonic leading edge radii, turbine blades, and hypersonic wind tunnel models are small but heat flux sensors are large. The installation of a heat flux sensor that has a radius of 1/16 in. to measure the stagnation heat flux on a leading edge radius of 0.25 in. is extremely hard simply because of space. Moreover the blunt sensor and air gaps behind the sensors can change the flow and lead to incorrect heat flux measurement. The majority of calibration facilities are radiation based and the heat flux environment is steady and spatially uniform. Most measurement

situations involve convective heat flux that is time and spatially transient. Lastly, the thermal contact between the sensor and the test article can greatly change the thermal resistance, and small details like proper depths and thicknesses can change the heat flux measurement and calculations. Even if all the other issues are solved, a sensor that is not in contact with the test article or that is at the wrong depth will not measure the correct heat flux.

Serious measurement errors have been documented post-test due to many of the above issues[11],[12]. Neumann et. al. in reference [12] presents multiple tests which document poor sensor choice in type and material, poor installation, and poor geometry for the chosen sensors. A specific example illustrating the issues with measuring heat flux is the Space Shuttle program's thermal instrumentation during the 1980s[12]. The issues present in that program included thin-film calorimeters that had an unknown film thickness due to improper installation, radiometers installed in a high ablative region affecting the measurements, and heat flux sensors mounted in an insulative environment resulting in a large material mismatch [12]. In the material mismatch, a high thermal conductivity sensor was mounted in a low thermal conductivity surface which led to the sensor measuring affecting the flow, and measuring the heat flux of the sensor, not the surface. This resulted in an error of up to 179% [12].

This study, in an effort to further the understanding of measuring heat flux, quantifies direct and indirect sensor designs for heat flux measurements within various test article materials. A test condition was chosen which has an analytic solution. The quasi-steady analytic solution for stagnation point of a hemisphere in hypersonic flow was derived by Fay and Riddell in 1958[33]. Further, the test model diameter of ¾ in. was chosen specifically to increase the heat flux at the stagnation point. This test condition was then run in the Virginia Tech Hypersonic Wind tunnel (VTHST) with $M_\infty = 6$, $T_{0\infty} = 1188°$ R, and $p_{0\infty} = 1200$ psi, and a computational fluid dynamic model was run using conjugate heat transfer at the chosen condition to aid in the understanding of the test results.

As a part of the study, all sensors were put into the Radiative Heat Flux Calibration system at the Aero-Thermal Test Materials Lab (ATM Lab) at Arnold AFB in Tullahoma, TN. The sensors were calibrated in the actual housing that they will be tested in to try to ascertain the effect of the various sensor designs and test article materials on the calibration.

The models were made of three different materials which were chosen both for their use in the aerospace flight and testing community, and for their large variation in thermal conductivity and thermal diffusivity. The three materials are Graphite, 304 Stainless Steel, and MACOR®. Stainless steel makes up many parts of fight vehicles as well as being the material of choice for high-speed wind tunnel models. MACOR®, a ceramic that can be machined made by Corning Inc., has been gaining wider use in high-speed wind tunnel models and its thermal diffusivity is roughly an order of magnitude lower than stainless steel. Graphite was chosen because its thermal characteristics are very similar to many carbon matrix composites (CMC) and carbon-carbon which are used in both high-speed flight and test systems. Graphite's thermal diffusivity is roughly an order of magnitude greater than stainless steel. Table 1-1 documents the characteristics of the chosen materials.

	ρ	c_p	k	α
	kg/m^3	J/kg/K	W/m/K	$W/m^2/J$
Graphite	1822	915.1	125.68	7.54E-05
304SS	7800	460	17.9	4.99E-06
MACOR	2520	795.5	1.47	7.33E-07

Table 1-1. Material Thermodynamic Properties.

In Table 1-1, α is the thermal diffusivity for the material which can be calculated with ρ, c_p, and k. The chosen heat flux sensors were the 1/8 in. fast response Schmidt-Boelter sensor made by the ATM lab, and a Dual Temperature 1/16 in. Chromel/Constantan

Coaxial Type-E thermocouple made by MedTherm with a second temperature measurement at 3/10 in. below the surface. The Schmidt-Boelter provides a changing voltage based on measured heat flux by outputting the difference in two thermopiles, one on the front of an insulator and one on the back[5]. There is also a Type-E thermocouple at the back of the Schmidt-Boelter. The MedTherm Coaxial Thermocouple provides a time-varying temperature at the surface that is used with the "Simple Explicit Inverse Method", created by Walker and Scott in 1995, to calculate the heat flux on the hemisphere[9].

This study documents error in heat flux measurement results from:

1) Test Article to sensor material mismatch
2) Test article and sensor external and internal geometry, and scale
3) Sensor installation details
4) Differences between heat flux environments in a calibration rig and the actual test.

It is broken into the following pieces:

- Chapter 2 covers the methods for the wind tunnel and calibration experiments
- Chapter 3 covers the computation and analytic methods
- Chapter 4 covers the experimental results
- Chapter 5 covers the computational results
- Chapter 6 compares the experimental and computational results
- Chapter 7 discusses the results
- Chapter 8 discusses the conclusions, and future work in this topic
- Appendix A is the uncertainty analysis for this study

2. Experimental Facilities and Methods

2.1 Virginia Tech Hypersonic Wind Tunnel

The Virginia Tech Hypersonic Wind Tunnel (VTHST) is a Mach 2-7 capable blow-down facility. This wind tunnel was obtained through a close and long-term collaboration with the Institute of Theoretical and Applied Mechanics of the Russian Academy of Sciences in Novosibirsk, Russia. Figure 2-1 is a schematic of the layout of the tunnel. A high pressure compressor supplies air to charge the storage bottles sitting in the frame at the bottom of Figure 2-1. When the tunnel is started, a special fast-acting valve opens to release the air into the plenum chamber. After exiting the plenum chamber the air enters one of the six fixed contour nozzles based on the required Mach number. From the nozzle the air enters the 100 mm diameter test section and then exits out through the diffuser. A special control valve maintains constant total pressure within 10% throughout a run which can last from 1-3.5 sec. When the experiment requires a Mach number above 4, the electric heater shown on the upper left-hand side of Figure 2-1 raises the total temperature to prevent liquefaction, and up to 800 K if required[34]. Details of the contoured nozzle assembly for the higher Mach numbers are shown in Figure 2-2.

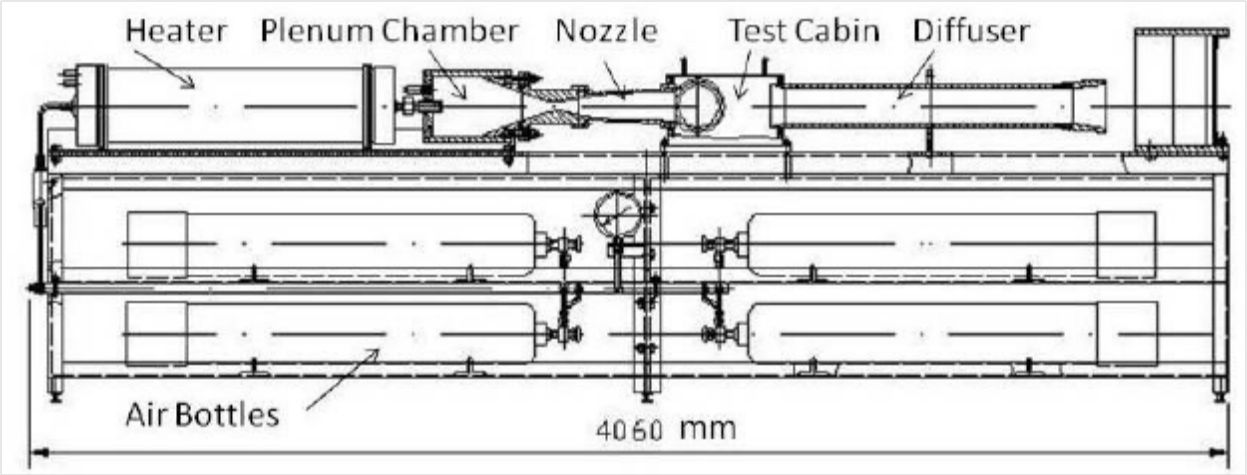

Figure 2-1. Virginia Tech Hypersonic Wind Tunnel. Public Domain.

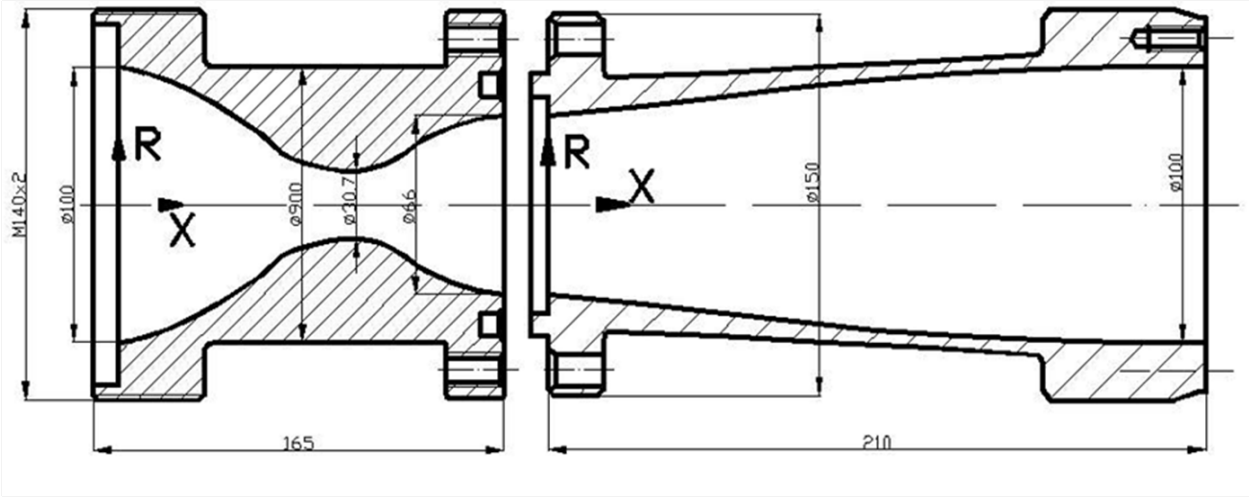

Figure 2-2. Drawing of the VTHST M = 6 Nozzle. Public Domain.

Table 2-1 documents the range of flow parameters at various Mach numbers. The nozzle exit diameter is 100 mm and the Test Cabin arrangement permits the use of relatively large models, especially at higher Mach numbers. The high total pressure levels attainable result in rather large Reynolds numbers as shown in Figure 2-3 where the characteristic length for the Reynolds number, *d*, is simply set to 1 (meter or foot based on the chosen units)[34].

M	P0min	P0max	Pmin	Pmax	T0min	T0max	Tmin	Tmax	ρ0max
	atm	atm	atm	atm	K	K	K	K	kg/m3
2	1.5	5.6	0.1917	0.7143	290.0	800.0	69.6	444.4	6.598
3	5.0	11.7	0.1361	0.3175	290.0	800.0	67.5	285.7	13.786
4	12.0	27.1	0.0790	0.1786	290.0	800.0	64.5	190.5	31.931
5	30.0	60.5	0.0567	0.1143	376.4	800.0	62.7	133.3	54.922
6	70.0	125.3	0.0443	0.0794	504.4	800.0	61.5	97.6	84.882
7	125.0	150.0	0.0302	0.0362	644.7	800.0	59.7	74.1	79.501
M	ρ0min	ρmax	ρmin	Gmin	Gmax	Remin	Remax	q min	q max
	kg/m3	kg/m3	kg/m3	kg/s	kg/s	1/m	1/m	atm	atm
2	0.641	1.518	0.147	0.824	5.097	5.082E+05	7.200E+06	0.537	2.000
3	2.136	1.051	0.163	1.300	5.036	9.253E+05	9.221E+06	0.858	2.000
4	5.125	0.883	0.142	1.243	4.665	1.218E+06	1.314E+07	0.885	2.000
5	12.814	0.623	0.145	1.267	3.722	1.804E+06	1.245E+07	0.992	2.000
6	29.898	0.441	0.155	1.361	3.068	2.713E+06	1.082E+07	1.117	2.000
7	53.390	0.207	0.139	1.374	1.837	3.351E+06	5.940E+06	1.035	1.243

Table 2-1. VTHST Flow Property variations.

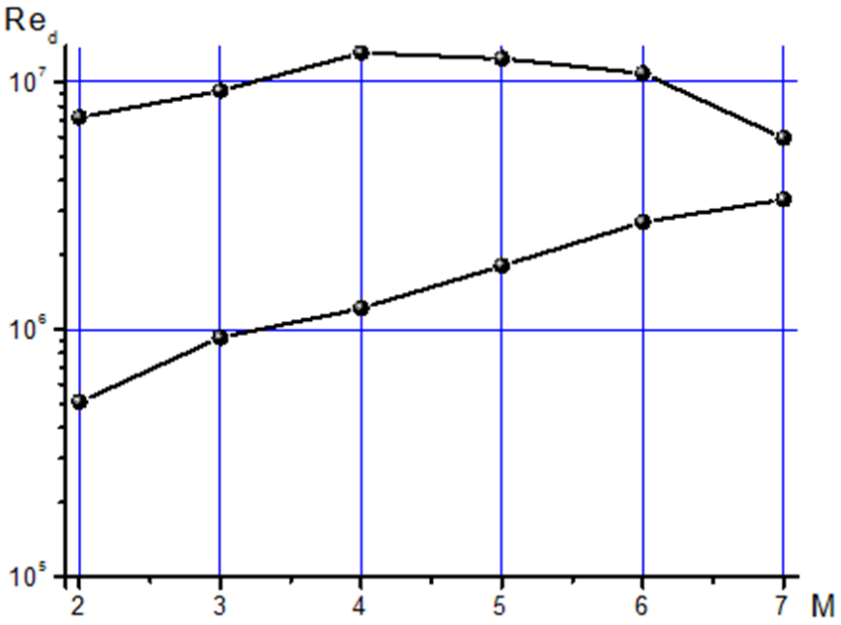

Figure 2-3. Reynolds number ranges in the VTHST.

2.2 Experimental Set-up

Testing in the Hypersonic Wind Tunnel for this study was performed using the Mach 6 nozzle (4.53% uncertainty) with a stagnation pressure of 1200 psia (0.05% uncertainty) and a stagnation temperature of 1188° R (0.015% uncertainty). The hemisphere model diameter is 0.75 in., chosen as the best combination of high heat flux (small diameter) and model integration (large diameter), and the cylinder behind the hemisphere is 0.75 in. long and 0.75 in. in diameter. The geometry of the various models is shown in Figure 2-4. The stainless steel models are made of one piece of stainless steel, as shown on the left side of Figure 2-4. The MACOR® and graphite hemispheres consisted of a hemisphere of the preferred material that duplicates the hemisphere portion of the stainless model. The hemisphere sits in a cylinder of stainless steel as depicted in the upper right of Figure 2-4. The stainless cylinder was implemented because the machined threads for the set screws on the model might not have held up in a solid graphite or MACOR® model.

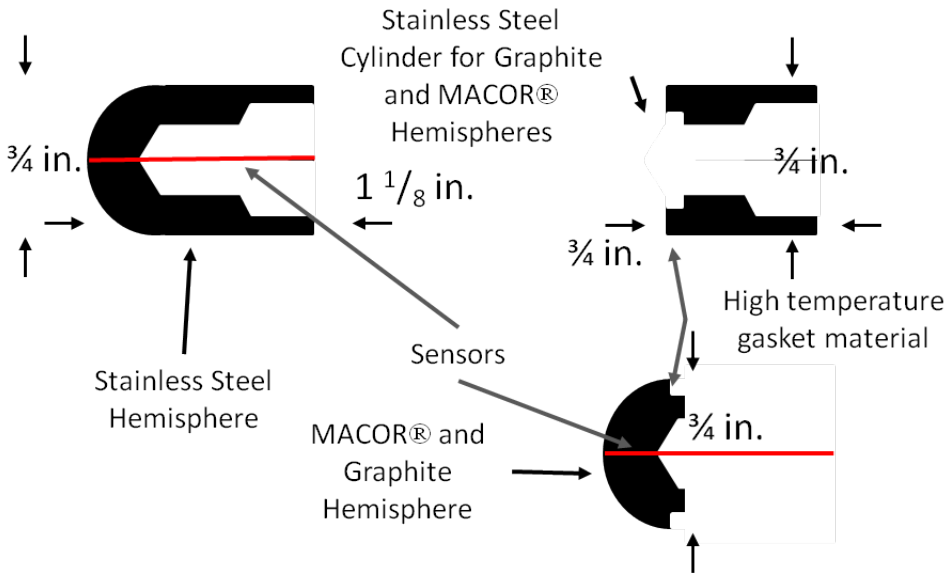

Figure 2-4. Experimental Hemisphere model designs for all materials.

The test fixture that is installed into the VTHST is shown in Figure 2-5. Also shown are the pitot tube and total temperature probe which measure p_{02} and T_{02} respectively. Figure 2-6 illustrates how the test fixture is mounted in the VTHST as well as a close up of the MACOR® hemisphere in the tunnel. Also shown are some of the components making up the shadow graph equipment used in each wind tunnel run.

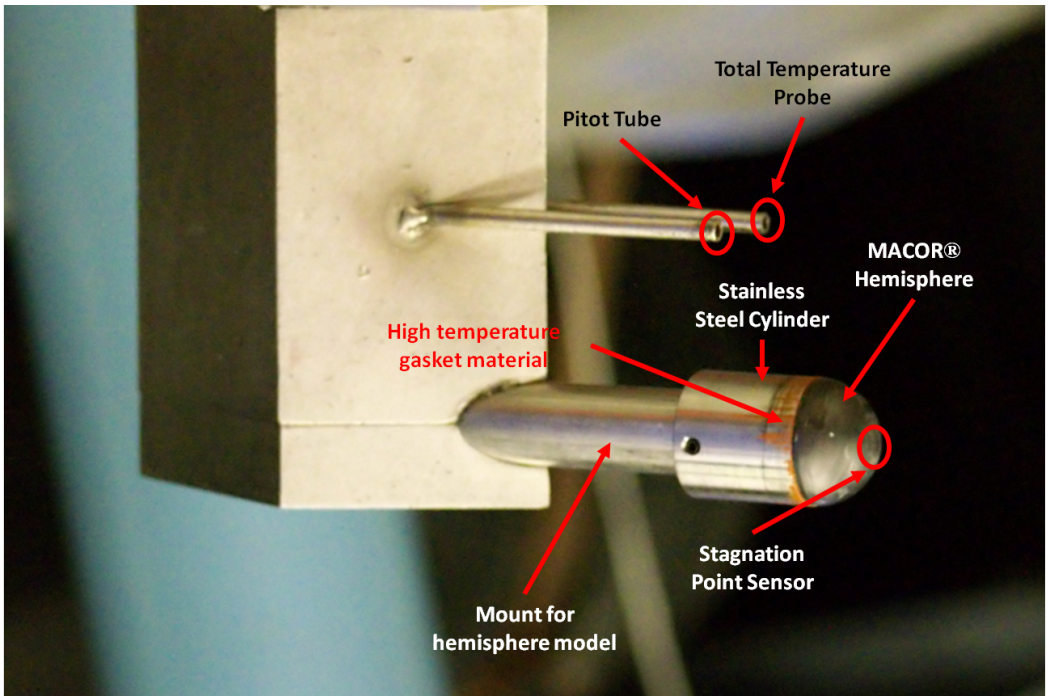

Figure 2-5. VTHST test fixture with the MACOR® hemisphere/MedTherm Coaxial Thermocouple mounted including pitot and total temperature probes.

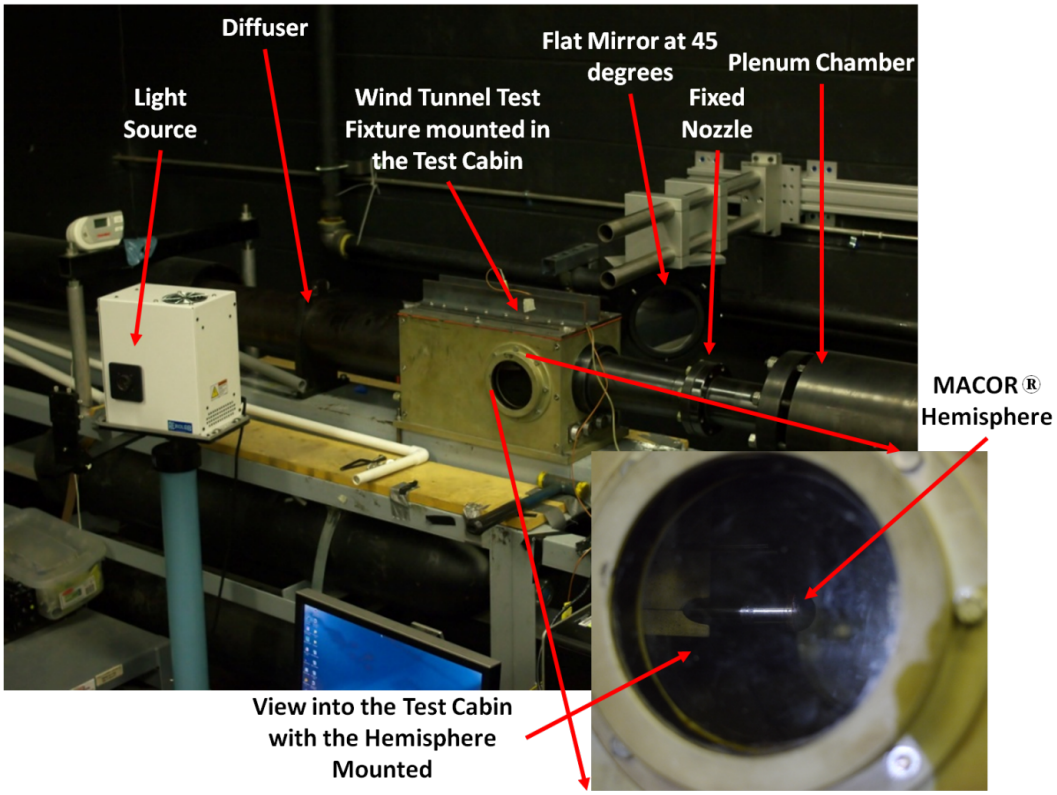

Figure 2-6. Lay-out of the VTHST including mounting of the test fixture in the tunnel.

When each sensor was mounted in its hemisphere, special care was taken to match the mounting adhesive to the material properties of the hemisphere. For example, the adhesive used to mount the sensors in the graphite hemispheres was 98% graphite. Similarly, the adhesives for the MACOR® and stainless steel duplicate their thermodynamic properties. This was done to try to eliminate material mismatches due to the adhesive.

The run time for these tests is 3 seconds. The "on-condition" time occurs after a 0.8 second start-up transient and lasts 2.2 second as shown in Figure 2-7. During this time the plenum pressure has a total variance of +/- 3% with a standard deviation of 1.2 psi and maximum fluctuations (peak to peak) on the order of 5 psi. The stagnation pressure measured behind the normal shock in the pitot probe varies by +/- 7% with a standard deviation of 1.9 psi and maximum fluctuations (peak to peak) on the order of 8 psi. In order to attain the 1188° R stagnation temperature, the heater is run at 1571° R. The reason the temperature settings appear so precise is that the actual settings on the VTHST are metric. In fact, the temperature setting for the heater is 600° C, and only varies 1/2° C once the heater is stable, which converts to roughly 1571° R. The VTHST is designed to have a 665 K stagnation temperature at that heater setting, which measured 1188° R during the actual VTHST runs. Mach 6 tests in the HST require a minimum 1050° R heater to prevent liquefaction. During the test the plenum pressure, stagnation pressure behind a normal shock, stagnation temperature, and a video of a shadow graph set-up are recorded along with the data from the sensors.

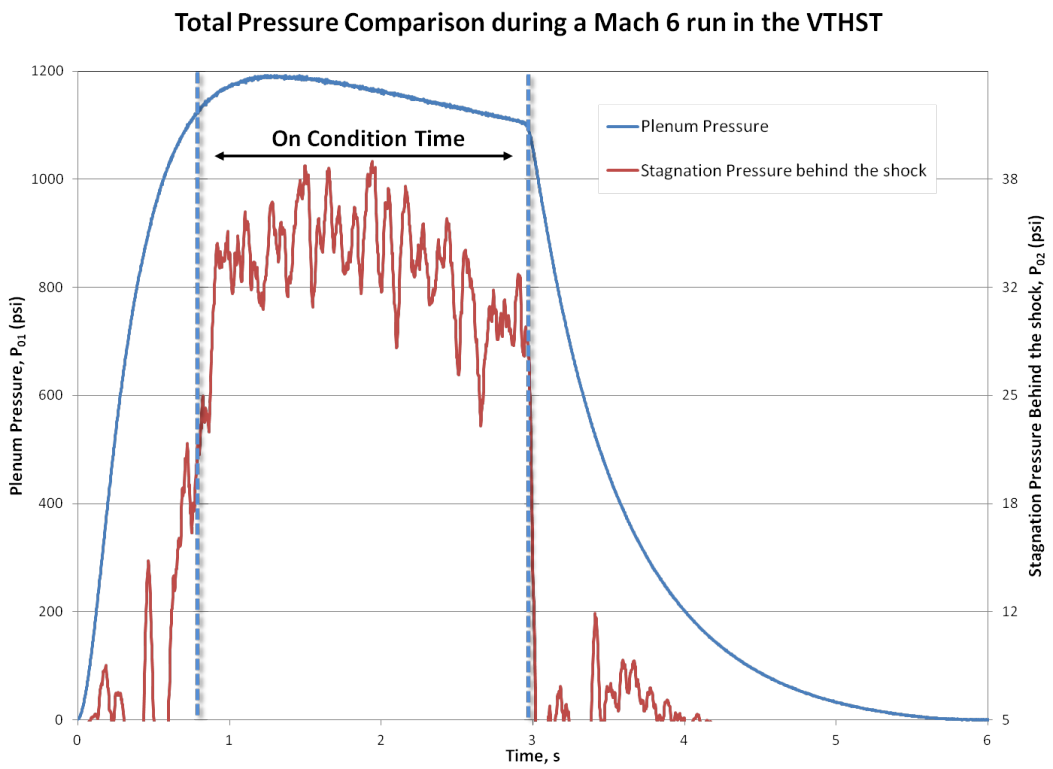

Figure 2-7. Plot of plenum pressure and stagnation pressure behind the shock for a typical run at Mach 6 in the VTHST.

Because of the large variation in the thermal diffusivity between the hemisphere materials, equation 1.9 is used to determine the length of time that the semi-infinite assumption will be valid for the inverse heat flux calculation. Assuming constant heat flux, the semi-infinite assumption for the MACOR® hemisphere with the lowest thermal diffusivity will be valid for over 23 seconds. At 3.5 seconds the semi-infinite assumption will no longer be valid for the stainless steel hemispheres. Lastly, the Graphite hemisphere only last 0.23 seconds before the semi-infinite assumption is not valid.

Figure 2-8 shows a typical shadow graph for the Mach 6 runs in the VTHST. Shadow graphs were taken of every wind tunnel run to insure tunnel start and Mach 6 flow conditions.

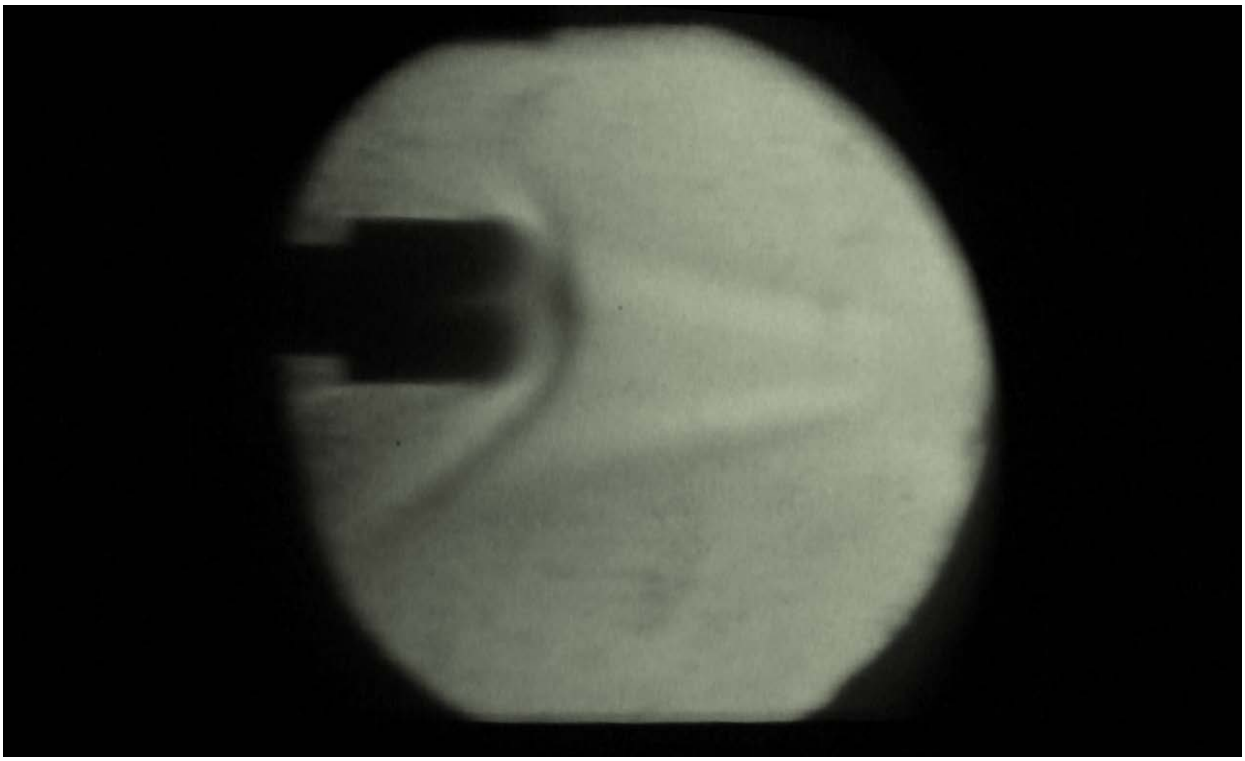

Figure 2-8. Shadow graph of the flow around the hemisphere for a typical run at Mach 6 in the VTHST.

2.3 Experimental Uncertainty

A discussion of the uncertainty for all parts of this study is included in Appendix A. Figure 2-9 shows the uncertainty on the measurement of Mach number throughout the on-condition time of a VTHST wind tunnel run for this study.

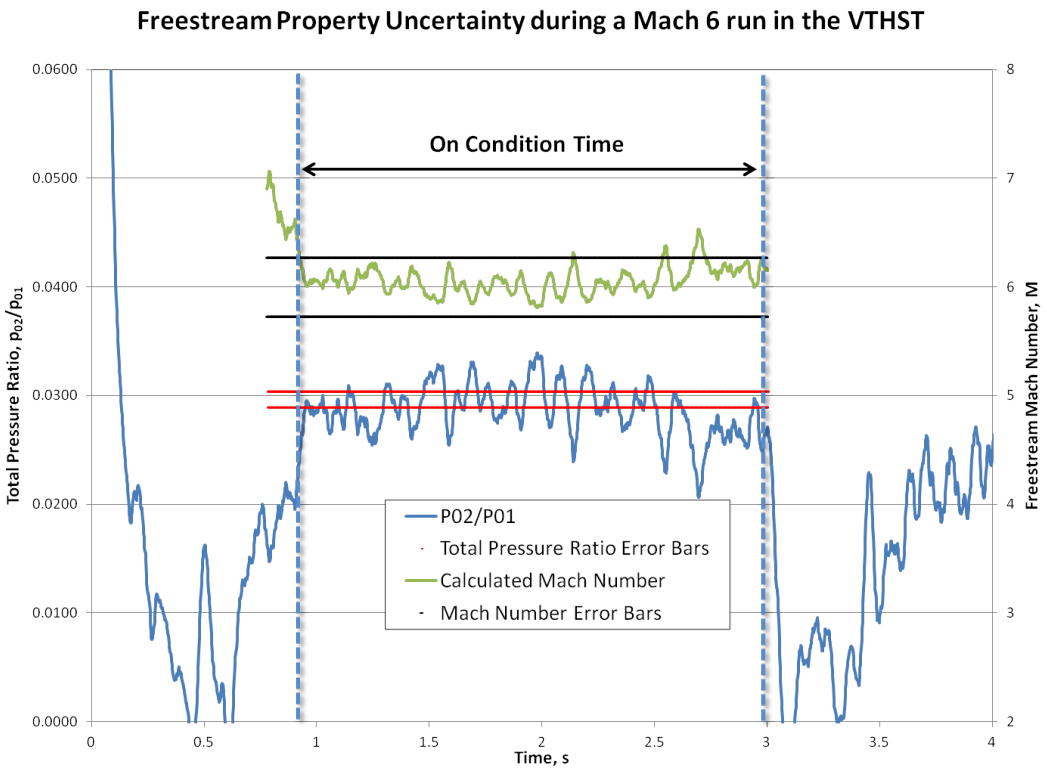

Figure 2-9. Uncertainty of the freestream Mach number and total pressure ratio during the VTHST run.

The uncertainty on the calculation of the inverse heat flux[9] as well as the uncertainty for the AEDC Schmidt-Boelter gages are derived in Appendix A. Table 2-2 is a summary of the uncertainties for this study. Note that the uncertainties between the two measurements are very large at 13.18% and 16.41% respectfully, but a large percentage of this is due to the uncertainty of the material properties and ratio of specific heats. Also the uncertainty calculations for the inverse heat flux method can not accurately capture the inaccuracies that arise due to invalid assumptions such as a measurement that involves two or three-dimensional conduction and a finite solid with multiple depths and complex internal geometry.

Measurement	Parameter	Uncertainty
Flow Total Pressure Ratio	p_{02}/p_{01}	2.44%
Flow Mach Number	M_∞	4.53%
Inverse Heat Flux Calculation	q_w''	9.84%
Fay-Riddell Calculation	q_w''	13.14%
Schmidt-Boelter Gage Heat Flux	q_{wSB}''	13.18%
Coaxial Thermocouple Inverse Heat Flux	q_{wIn}''	16.41%

Table 2-2. Summary of the uncertainty for this study from Appendix A.

2.4 Imperfect Gas Effects

In high Mach number wind tunnel flows, as well as in high Mach number flow around an aircraft, thermal and caloric imperfections have an effect on the environment that is under study. The magnitude of these changes, as well as when and how they occur, changes the design points of many of the structures and functions on a hypersonic vehicle. The types of material required for structures, as well as the cooling requirements for the vehicle, can change radically due to these differences in the properties on the vehicle between ideal and real conditions.

So called real gas effects take into account the caloric and thermal imperfections, as well as gaseous imperfections that occur due to disassociation. For most hypersonic flows in wind tunnels and on flight vehicles, the total temperature of the flow remains below 5000° R, and the gaseous imperfections can be ignored[35]. In fact, while the gas is not calorically or thermally perfect, for the flows with total temperatures below 5000° R the properties can be calculated ignoring thermal imperfections due to their negligible effects[35].

The Virginia Tech Hypersonic Wind Tunnel (VTHST) is capable of Mach numbers up to Mach 7 and total temperatures up to 1400° R. At the test conditions for this experiment, M_∞ = 6 and $T_{0\infty}$ = 1188° R, the flow is in the range of caloric imperfections. These imperfections do have an effect on the properties within the flow, and a study was performed to ascertain the magnitude of the effects. It is important to note that larger wind tunnels such as the Arnold Engineering and Development Center's Tunnel 9 are capable of much higher total temperatures and Mach numbers such that even imperfect gas assumptions are not valid. In many of these tunnels the calculations must include all the disassociation and reactions involved in a real gas. The CFD program chosen for this study, GASP, has full real gas calculation capability.

2.4.1 Imperfect Gas Analytic Method

For a thermally and calorically perfect gas, equation 2.1 and 2.2 are used to close the Navier-Stokes Equations.

$$p = \rho RT \tag{2.1}$$

$$u = c_v T + u_r \tag{2.2}$$

where p is pressure, ρ is density, R is the Gas Constant for the chosen gas, T is temperature, u is specific internal energy, c_v is the specific heat at constant volume, and the subscript r denotes the reference conditions. When the flow becomes calorically imperfect but thermally perfect, equation 2.1 can still be used, but now equation 2.3 must be solved.

$$\mathrm{du} = c_v \mathrm{dT} \tag{2.3}$$

If the thermally imperfect effects are not neglected, equations 2.4 and 2.5 must be used to close the Navier-Stokes equations. This thermal equation of state is known as Berthelot's equation, but there are other possible choices for the thermal equation of state.

$$p = \frac{RT}{v - b} - \frac{c}{v^2 T} \tag{2.4}$$

$$\mathrm{du} = c_v \mathrm{dT} + [T(\frac{\partial p}{\partial T})_v - p]\mathrm{dv} \tag{2.5}$$

where v is specific volume, b is the molecular-size constant, c is the intermolecular-force constant, and the subscript v denotes a process at constant volume.

To simplify the solution for these interim flows but still account for the vibrational heat capacity contribution to the specific heats, a simple harmonic vibrator can be assumed[35]. With these equations the ratio of specific heats, γ, can be calculated for temperatures ranging from 500° R to 5000° R[35]. Figure 2-10 graphs these approximate values of gamma for air and includes a polynomial curve fit for rapid calculation between data points. The VTHST test condition for this study is represented by the red triangle.

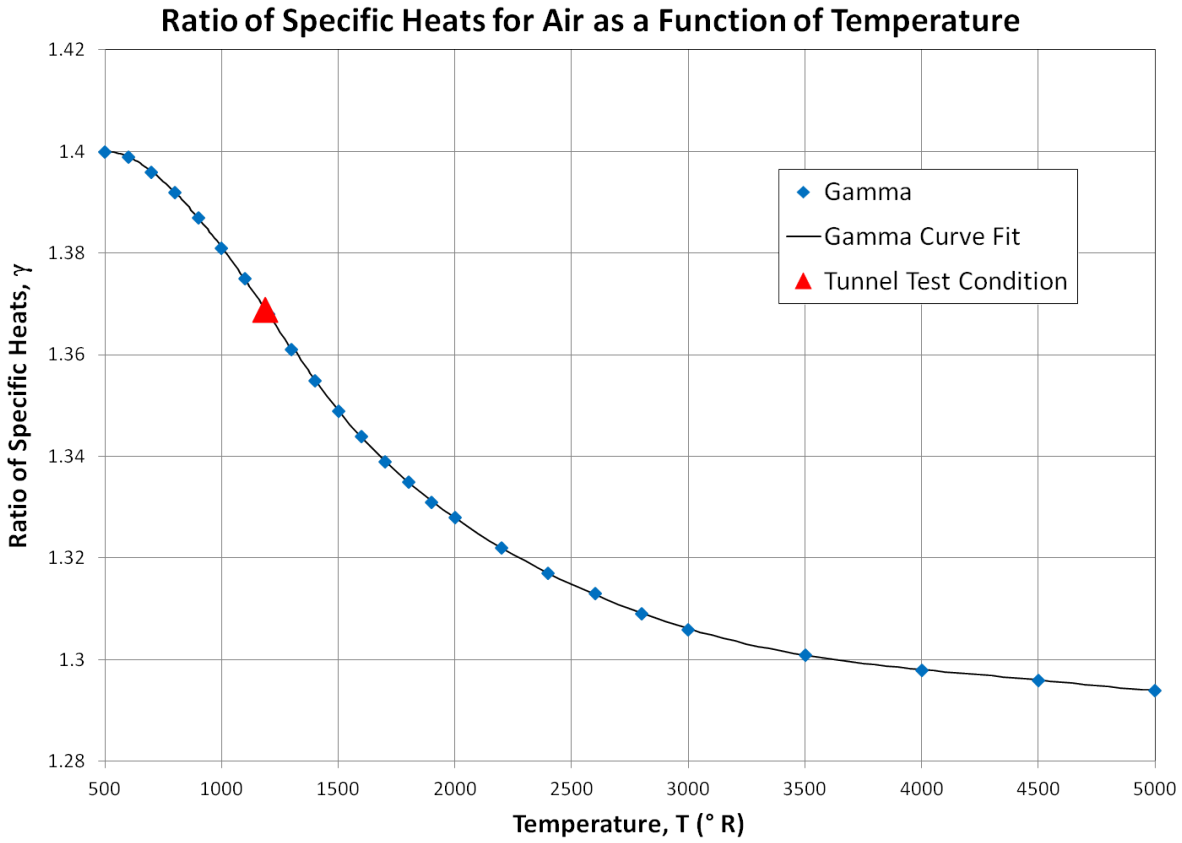

Figure 2-10. Gamma changes with Temperature[35].

Using the equations above and the derivation in the NACA 1135[35], the changes in the properties within a thermally perfect, calorically imperfect flow were calculated.

2.4.2 Imperfect Gas Results

Assuming a thermally and calorically perfect flow with a ratio of specific heats of 1.4, Table 2-3 documents the flow properties upstream and downstream of a normal shock.

γ = 1.4	Upstream (1)	Downstream (2)	Units
M	6.0000	0.4042	
p_0	1200.00	35.58	psi
T_0	1188.00	1188.00	° R
ρ_0	8.4764E-02	2.5133E-03	slugs/ft^3
p	0.76	31.79	psi
T	144.88	1150.42	° R
ρ	4.4023E-04	2.3192E-03	slugs/ft^3
a	589.96	1662.46	ft/s
V	3539.77	671.90	ft/s

Table 2-3. Flow properties upstream and downstream of a normal shock at test conditions assuming a thermally and calorically perfect gas with γ=1.4.

The simple use of a variable ratio of specific heats that accounts for vibrational energy changes the conditions behind the shock. Table 2-4 shows these changes.

γ = 1.3689	Upstream (1)	Downstream (2)	Units
M	6.0000	0.3945	
p_0	1200.00	29.20	psi
T_0	1188.00	1188.00	° R
ρ_0	8.4764E-02	2.0623E-03	slugs/ft^3
p	0.63	26.29	psi
T	155.49	1154.85	° R
ρ	3.4223E-04	1.9100E-03	slugs/ft^3
a	604.37	1647.05	ft/s
V	3626.20	649.74	ft/s

Table 2-4. Flow properties upstream and downstream of a normal shock at test conditions assuming a thermally and calorically perfect gas with γ=1.3689.

Table 2-5 tabulates the new properties behind the shock when air is assumed to be calorically imperfect and thermally perfect. The changes were interpolated from the charts the NACA 1135 Report[35].

γ = 1.3689	Upstream (1)	Downstream (2)	Units
M	6.0000	0.3944	
p_0	1200.00	28.79	psi
T_0	1188.00	1188.00	° R
ρ_0	8.4764E-02	2.0339E-03	slugs/ft^3
p	0.63	26.37	psi
T	155.49	1140.39	° R
ρ	3.4223E-04	1.9436E-03	slugs/ft^3
a	604.37	1636.71	ft/s
V	3626.20	645.49	ft/s

Table 2-5. Flow properties upstream and downstream of a normal shock at test conditions assuming a thermally perfect and calorically imperfect gas with γ=1.3689.

Table 2-6 lists the percentage change on the downstream side of the shock due to adjusting γ and accounting for the caloric imperfections. While the largest changes come from using a more accurate ratio of specific heats, it is interesting to note that the static temperature behind the shock increases with the accurate γ, but decreases by over double that percentage when the gas is treated as calorically imperfect.

	γ Changes	Calorically Imperfect
M	-2.39%	-2.42%
p_0	-17.94%	-19.08%
T_0	0.00%	0.00%
ρ_0	-17.94%	-19.08%
p	-17.33%	-17.06%
T	0.39%	-0.87%
ρ	-17.64%	-16.20%
a	-0.93%	-1.55%
V	-3.30%	-3.93%

Table 2-6. Percentage change in flow properties between perfect gas and imperfect gas assumptions.

This data shows an interesting interpretation of the changes on the flow properties themselves, but the real question is how these assumptions and changes influence the

desired property, surface heat flux in this case. Figure 2-11 shows how these changes impact the analytically predicted heat flux using the Fay-Riddell equation[33]. Throughout the on-condition time in the VTHST, the imperfect gas effects lower the predicted heat flux by almost 11%, slightly increasing the difference through the run.

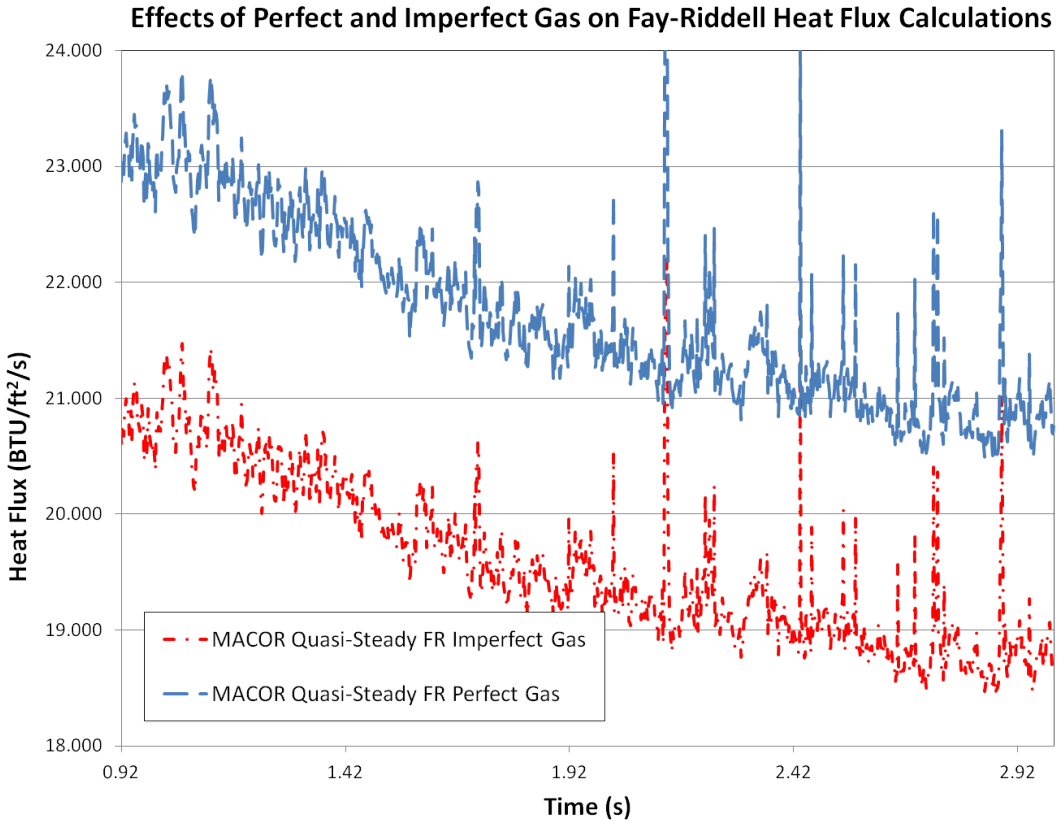

Figure 2-11. Fay Riddell Quasi-Steady Heat Flux Changes with Imperfect Gas Effects, $M_\infty = 6$ p_0=1200 psi, T_0=1188° R.

2.4.3 Imperfect Gas Conclusions

Hypersonic flow brings many challenging conditions that differ from standard compressible flow. The leap to real gas calculations is complicated and computationally intensive. For most predictions in low to medium range hypersonic flows, the properties can be calculated using imperfect gas assumptions without going to full real gas effects. In the VTHST at the chosen heat flux conditions, imperfect gas effects do have an effect on the calculated property, but this effect is within the uncertainty of the analytic calculation as shown in Appendix A.

2.2 AEDC ATM LAB Calibration Set-up

The heat flux sensors mounted in the models were calibrated in a radiative heat transfer facility because it is difficult to produce a known, high heat flux in a convective facility. The calibrations at the AEDC ATM Lab were radiative in nature and had heat flux values from 1-20 Btu/ft^2/s. The runs can be transient, where the sensor takes data as a shutter opens, or steady state, where the sensor takes data after being exposed to the heated lamps for a second. Figure 2-12 is a simplified drawing of the facility. In general direct heat flux sensors are calibrated with the steady method and indirect sensors are calibrated with the transient method. Along with the sensor that is being calibrated, there are three 3/16 in. Schmidt-Boelter Gages whose calibrations can be traced to NIST and a 1/8 in. MedTherm Type E Coaxial Thermocouple in order to verify the calibration. In all tests, all surfaces were painted with Krylon 1602 Ultra-flat black paint which has an emissivity of 0.97 in the wavelengths of the AEDC ATM Lab's heat lamp. Figure 2-13 illustrates the mounting of the various sensors including a cross section to highlight the hole in which the hemisphere sits. This facility is capable of calibrating a heat flux sensor to a 3% uncertainty as documented by Kidd in reference [19].

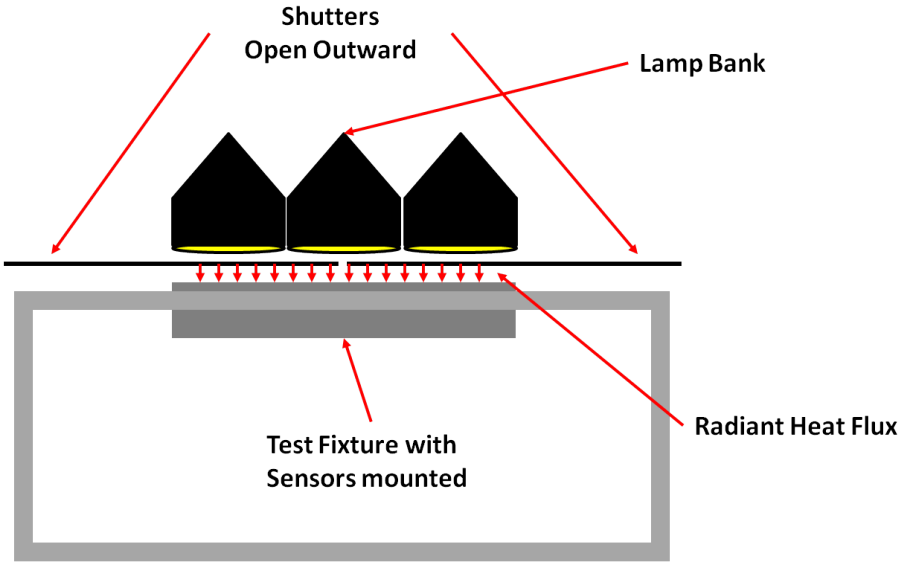

Figure 2-12. Schematic of the Radiant Heat Flux Calibration Facility at the ATM Lab.

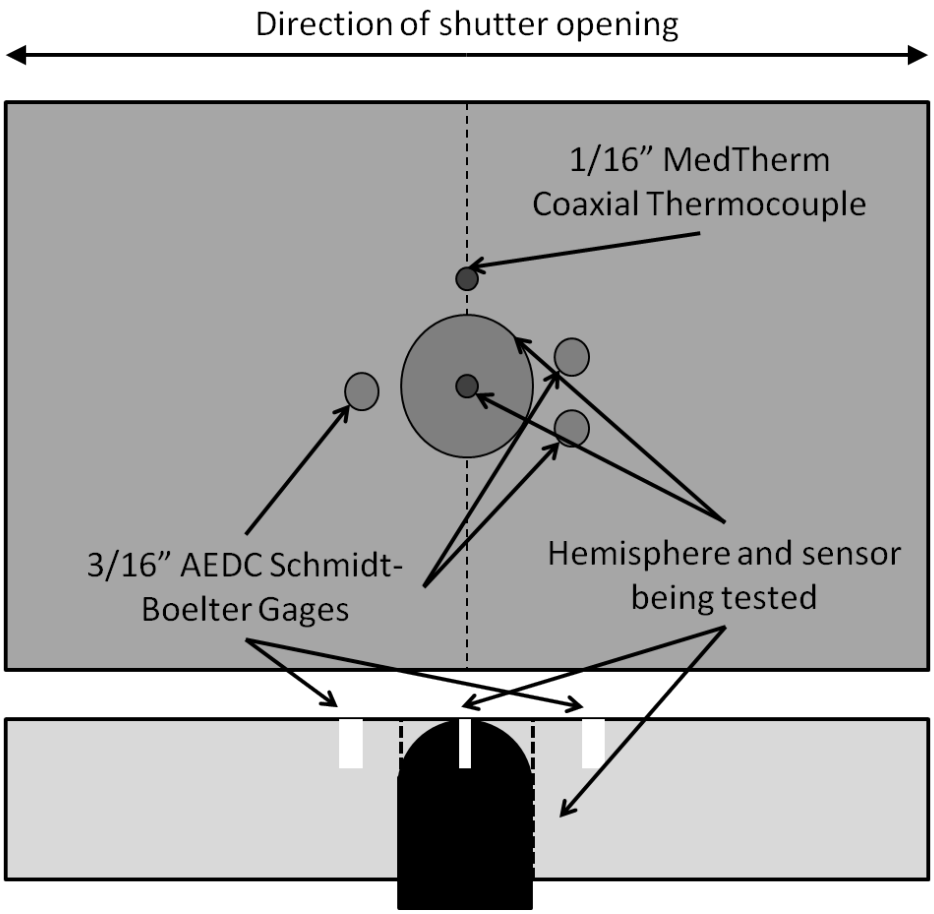

Figure 2-13. Calibration test fixture at the ATM Lab.

3. Computational and Analytic Methods

3.1 Computational Method

Modern computational fluid dynamics (CFD) methods with a conjugate heat transfer treatment of heat conduction in a solid provide a powerful capability to complement an experimental study such as undertaken here. These computations were performed in collaboration with Dr. Reece Neel of Aerosoft, Inc. GASP Version 5 was used to simulate Mach 6 flow over a hemisphere cylinder. In this simulation, both the external flow and internal heat transfer are computed via conjugate heat transfer (CHT). The hemisphere/cylinder model is composed of stainless steel, graphite, and MACOR, but has either a modeled chromel coaxial thermocouple running along the length of the model, with an exposed tip flush at the stagnation point, a modeled fast response Schmidt-Boelter gage with an exposed tip flush at the stagnation point, a silica fiber to simulate a possible future fiber-optic temperature sensor, or a "perfect" sensor composed of the hemisphere model's material.

GASP is a time-dependent, three dimensional, Reynolds-averaged Navier-Stokes (RANS) solver. It treats the integral form of the governing equations using upwind-based, finite-volume formulations. GASP supports multi-block, structured grid topologies with automated domain decomposition for parallel computing. In this study, second-order temporal accuracy is achieved through the implementation of a dual-time-stepping algorithm[36]. Spatial accuracy for the convective fluxes used the third order MUSCL scheme with second order accuracy for the diffusive fluxes[36].

The CFD model used the following parameters

- ¾ inch outside diameter hollow cylinder
- cylinder walls are 1/8 in. thick
- length of cylinder portion is ¾ inch
- base region is flat

- material is 304 stainless steel, graphite, or MACOR®
- a modeled chromel thermocouple, modeled Schmidt-Boelter gage, silica fiber or a perfect sensor of the hemisphere material runs along length of each model
- modeled sensor has exposed tip flush at surface
- thermocouple diameter is 0.0625 in., Schmidt-Boelter gage diameter is 0.125 in., fiber diameter is 125 microns.
- Mach 6 flow
- air composition
- stagnation pressure = 1200 psia
- stagnation temperature = 1188° R

The model is assumed to be at an initial temperature of 300 K. GASP simulates both the heating within the solid and the external flow field for two seconds. The physics involved here correspond to two distinct time scales. For a Mach 6 flow, the fluid flow will react and set up very quickly (a fraction of a second), while the heating within the solid will evolve more slowly (on the order of seconds). In order to deal with this, the fluid flow is solved to steady state first assuming a constant wall temperature of 300 K. Once this is achieved, the solution represents time t = 0 for the transient simulation. GASP is then used to solve both the fluid and solid (coupled together via heat transfer at the surface) out to t = 2 seconds.

The CFD simulations involve three major assumptions. First, the violent transients during the VTHST start-up are ignored, and the time accurate portion starts on-condition. This means that the solid is unaffected by "start-up". This assumption has to be made as a time accurate wind tunnel simulation including start-up is very complex and would involve a full tunnel, 3-D, time-accurate simulation. Second, the complex internal geometry of the hemisphere is neglected, along with the more intricate geometry of the coaxial thermocouple, Schmidt-Boelter gage, and fiber. Again, the main purpose of this assumption is to reduce grid size and complexity and because the contact thermal resistance difference between simulation and test is already a larger concern. Lastly, the

thermal contact between the various materials is assumed perfect. The normal contact resistance that occurs between two materials is neglected as if the various materials were bonded at a molecular level.

The geometry and flow are both symmetric in this case. Because of this, the simulation can be performed using an axi-symmetric mesh. This greatly reduces the CPU time requirement and/or allows a much finer mesh to be used.

Grid generation was performed using GridGen. An initial axi-symmetric grid was generated for the flow field. This initial grid was then used in GASP to obtain a preliminary flow field solution. For this initial test simulation, the no-slip, constant wall temperature boundary condition was used since the solid was not meshed at this point. This initial mesh for the flow field allowed the following to be studied:

1. Grid spacing at the walls. Getting the initial wall spacing on the fluid side was important since this same spacing would later be used on the solid mesh. Having the same wall spacing for both the fluid and solid is not a requirement, but it is desirable for CHT calculations to increase accuracy in the heat transfer predictions. The initial wall and fluid spacing was $2x10^{-7}$ m.

2. Farfield boundary location. Since the external free-stream flow is Mach 6, the outer boundary of the hemisphere cylinder mesh can be close to the body. Thus once the shock profile is calculated, the mesh can be regenerated using the shock as a measure of where to place the outer "inflow" boundary.

The initial mesh was then refined for the fluid and the solid grids were created. The resulting axi-symmetric fluid mesh consisted of 25,537 cells. Once the wall spacing and the outer boundary were determined, the solid portion of the model was meshed. The grid for the solid had the same wall spacing along the fluid surface, while all other surfaces (non-conjugate boundaries) had a wall spacing of $5x10^{-5}$ m. The axi-symmetric fluid-

solid grids consisted of 38,995 cells for the modeled thermocouple and perfect sensor cases, 46,495 cells for the modeled Schmidt-Boelter gage cases, and 37,208 cells for the modeled fiber cases. A view of both the fluid and solid grid is shown in Figure 3-1, including a close-up. In this figure, the fluid grid is shown in blue, while the material grid is in black.

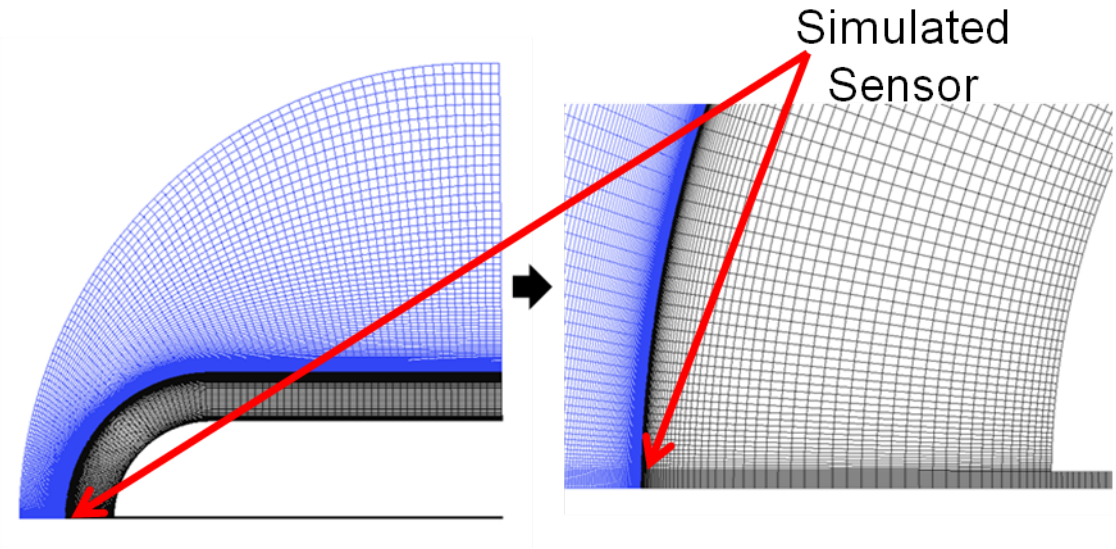

Figure 3-1. Refined grid for CFD Study.

For the solid, 12 physical models were used. There were three hemisphere models, graphite, MACOR®, and stainless steel, and four sensor models, a modeled coaxial thermocouple of chromel, a modeled Schmidt-Boelter gage composed of 6 layers, a silica fiber, and a "perfect" sensor composed of the model's material. Table 3-1 shows the various material properties for the simulations. The thermocouple was modeled as a homogeneous, solid cylinder with material properties representing a lumped equivalent of the actual multi-material thermocouple following suggestions from MedTherm. Similarly, the Schmidt-Boelter gage was modeled as a stack of materials with varying thicknesses and properties following the suggestions of the ATM Lab and Dr. John Adams.

	ρ	c_p	k	α
	kg/m^3	J/kg/K	W/m/K	$W/m^2/J$
Graphite	1822	915.1	125.68	7.54E-05
304SS	7800	460	17.9	4.99E-06
MACOR	2520	795.5	1.47	7.33E-07
Modeled TC	8670	426.4	17.3	4.68E-06
Modeled SB 1 (Stycast 2782 Epoxy)	2187	837.4	1.38	7.55E-07
Modeled SB 2 (Aluminum Nitirde Wafer)	3211	711.8	186.919	8.18E-05
Modeled SB 3 (Stycast 2782 Epoxy)	2187	837.4	1.3832	7.55E-07
Modeled SB 4 (Air)	GASP models Air			
Modeled SB 5 (Aluminum)	2707	870.9	204.116	8.66E-05
Modeled SB 6 (304 SS)	7800	460	17.9	4.99E-06
Silica	2200	740	1.38	8.48E-07

Table 3-1. Properties of the materials used in the CFD Simulations.

The material properties (other than air) were held constant (no variation with temperature). For the boundary conditions, the interior and rear walls were set to adiabatic. For the zonal boundary that separated the two materials, a special solid/solid condition was applied. This allowed for the jump in material properties to be handled properly.

Specifically when modeling the Schmidt-Boelter gage, efforts were made to try and simulate what this computational sensor would "measure" in the simulated hypersonic flow. To do that, the "measured" heat flux was calculated using equations 1.6 and 1.12 from Chapter 1. The τ* was assumed to be 0.015s which is on the order of the τ*s for the actual Schmidt-Boelter gages used in this study. To calculate the heat flux using equation 1.6, the front temperature is an average of the temperature across the modeled wire and adhesive layer on the front of the sensor, taken from a line halfway between the stagnation point and the next material. The rear temperature is similarly the average temperature across the rear wire and adhesive layer, halfway deep into the layer. The thickness is the distance between these two lines, and the thermal conductivity is the thermal conductivity of the wafer used in GASP. By reducing the data from GASP with these parameters, the modeled Schmidt-Boelter gage was able to make "measurements" similar to those described in reference [5].

3.2 Analytic Method

The quasi-steady analytic model, the Fay-Riddell equation[33], is shown below. The *w* subscript denotes values at the wall and the *e* subscript denotes values at the edge of the boundary layer.

$$q" = 0.763\mathrm{Pr}_w{}^{-0.6}(\rho_e\mu_e\kappa)^{1/2}(\frac{\rho_w\mu_w}{\rho_e\mu_e})^{0.1}(h_e - h_w) \quad (6)$$

- where κ is the local velocity gradient[33]

$$K = \frac{V_\infty}{D}(\frac{8\rho_\infty}{P_e})^{1/2} \quad (7)$$

- Conditions behind the shock were calculated assuming a perfect gas normal shock due to the uncertainty in all other properties
- As much as possible, all properties were calculated based on the correct temperature/pressure at each point in time using the "Thermodynamics of Air" calculator which outputs the equilibrium properties of air at non-standard temperatures and pressures and Sutherland's Law for the viscosities
- The wall temperature was taken from a measured temperature at the stagnation point using the sensor that best matches a given material if possible.

For each of the materials a new quasi-steady heat flux was calculated at each instant during the on-condition test time using equation 6. This allows the analytic model to accurately capture the changes in heat flux that occur due to the higher or lower thermal diffusivity of air and changes in wall temperatures due to material changes.

4. Experimental Results

The following chapter documents the results of the calibration at AEDC and the wind tunnel runs in the VTHST. The setup and details of the experiments are covered in Chapter 2, Experimental Facilities and Methods.

The graphs in this chapter will be described at the beginning of each section in order to reduce the complexity of the plots, and to keep the possible combinations of dots, dashes, and colors below the 20 combinations required for this section.

4.1 Calibration Results

This study required two separate sets of tests in the AEDC ATM Lab's radiative heat flux calibration set-up. In the first set of tests, the Schmidt-Boelter Gages were subjected to a steady-state radiative heat flux of 1, 3, 5, 8, and 12 Btu/ft^2/s. In order to create a steady environment, the heat lamp was turned on at the required setting , allowed to come to temperature for 15-20 seconds, and then the lamp shutters were opened for another 30 seconds before data was taken. The Schmidt-Boelter gages in all 3 materials were tested at these conditions and compared to the calibrated verification sensors. This allowed all initial transients and response times to be neglected in order to determine the response to a steady heat flux environment. The MedTherm coaxial thermocouples were tested dynamically at 1, 3, 6, 9, 12, and 20 Btu/ft^2/s. The Schmidt-Boelter gages were also tested dynamically to determine their τ^*. In the dynamic tests, the heat lamp was again allowed to come up to temperature for 15-20 seconds. At that point, the data acquisition was started and run for roughly a second before the shutters were opened exposing the sensors to the applied heat flux. In doing this, the sensors are tested in a step-response scenario which illustrates the time-response of the sensor as well as the accuracy of the measurement. In all cases, the hemispheres with sensors installed were painted with Krylon® 1602 Ultra-flat black paint which has an emissivity of 0.97. In the second set of tests, temperature measurements were taken in a MACOR hemisphere during a dynamic

test in both the calibration test fixture shown in Figure 2-13 made of stainless steel, and an equivalent MACOR® test fixture without the extra sensors. This test was to document what, if any, energy loss in the MACOR® hemisphere calibrations was due to the higher thermal conductivity of the stainless steel test fixture.

4.1.1 Steady-State Calibration Results

Table 4-1 illustrates the response of the three Schmidt-Boelter gages mounted in their hemispheres at two heat flux settings, 3 and 12 BTU/ft^2/s. It also shows the percentage difference in the actual lamp power for each run compared to the average for each power setting. The sensors in the hemispheres are compared to the average of the three calibration Schmidt-Boelter gages mounted in the calibration test rig as shown in Figure 2-13. In this calibration environment, the material effect on the Schmidt-Boelter gages is within the quoted uncertainty of the gages themselves, and simply varies in the direction of the lamp power variation. At 12 BTU/ft^2/s the variation between the lowest measured q_w'' in MACOR® and the highest in stainless steel is only 3.3% even with the 1.2% variation in the heat flux setting. This variation falls within the uncertainty of the 3% Schmidt-Boelter gage[19]. In this heat flux environment that is steady in time and uniform in space, the variation between the three sensors mounted in the three different materials is only 0.5% larger than the variation between the three calibration sensors.

Hemisphere Material	Measured Value	Difference from Calibration Gauges	Lamp Variation from Setting	Manufacturer's Uncertainty
	BTU/ft^2/s	%	%	%
Stainless Steel 3 BTU	2.9533	1.07%	2.09%	0.03
MACOR 3 BTU	2.88822	-1.16%	-1.16%	0.03
Graphite 3 BTU	2.90177	-0.70%	-0.92%	0.03
Stainless Steel 12 BTU	12.0993	1.73%	0.73%	0.03
MACOR 12 BTU	11.7068	-1.57%	-0.50%	0.03
Graphite 12 BTU	11.9776	0.71%	-0.22%	0.03

Table 4-1. Results for Schmidt-Boelter gages in all materials during static calibration at 3 and 12 BTU/ft^2/s.

4.1.2 Dynamic Calibration Results

The calibration at the ATM Lab involved running each of the MedTherm coaxial thermocouples through a dynamic test at various radiative heat flux settings, and the Schmidt-Boelter gages through a static test. The surface of the hemispheres and sensors were painted with a black paint of known thermal emissivity. Figure 4-1 compares the temperature results of the coaxial thermocouples during each of the tests at 12 BTU/ft^2/s. In this figure, red is the coaxial thermocouple mounted in the MACOR® hemisphere, blue is in the stainless steel hemisphere, black is in the Graphite hemisphere, and green is the calibration coaxial thermocouple mounted in the stainless steel block of the calibration rig. The front temperature measurements are solid lines and the rear are dashed. The thermocouple mounted in MACOR® has the hottest surface temperature and takes the longest for the rear surface to heat up, while the graphite thermocouple is at the other end of the spectrum as heat is conducted very quickly away from the surface. As a reference, the calibration thermocouple mounted in the surrounding test fixture as shown in Figure 4-1 is shown in green to show the temperature of a block of stainless steel. Note that the thermocouple in the stainless hemisphere is in fact hotter than the calibration thermocouple. This shows that there is some other physics contributing to the rate of the temperature rise besides a material match between the sensor and the test article.

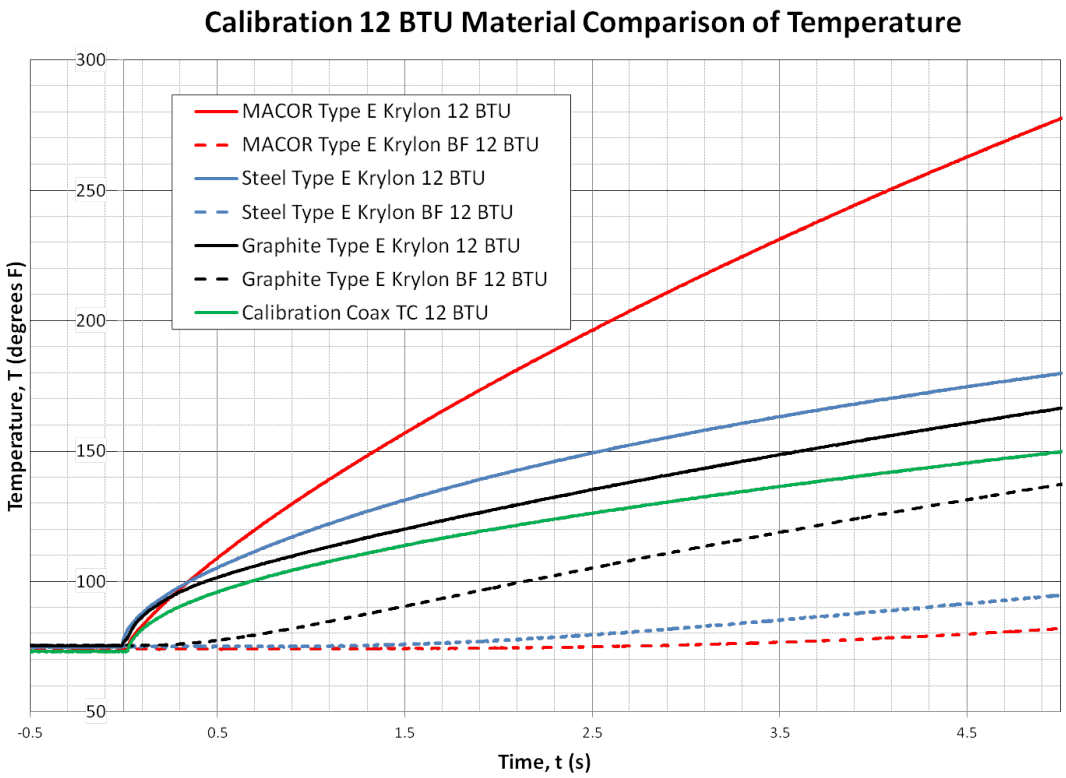

Figure 4-1. Temperature results for all materials during calibration at 12 BTU/ft^2/s.

Each of the temperature profiles were then used in an inverse[9] calculation to provide the corresponding heat flux for that sensor. Figure 4-2 shows these heat flux calculations including the output from one of the calibration Schmidt-Boelter sensors and the coaxial thermocouple mounted in the stainless steel test fixture. Due to material mismatch and shape effects none of the sensors mounted in the hemispheres are able to accurately predict the input surface heat flux.

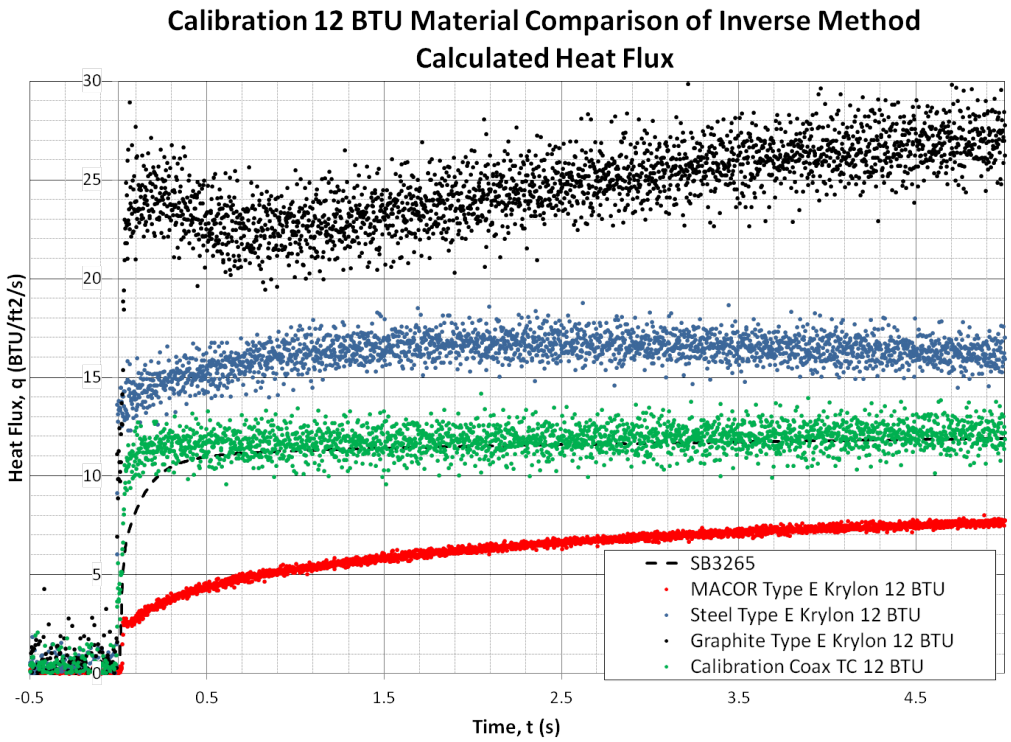

Figure 4-2. Inverse heat flux results for all materials during calibration at 12 BTU/ft^2/s.

Looking at the results of the thermocouple in the stainless steel hemisphere in more detail shows that this trend is duplicated at all heat flux levels. Figure 4-3 shows the large temperature differences between a coaxial thermocouple mounted in a stainless steel hemisphere and a coaxial thermocouple mounted in the stainless steel calibration test fixture. At every heat flux setting, the hemisphere thermocouple, shown with a black line, is at least 10% hotter by the end of the calibration run. The rear temperature in the hemisphere, shown in blue, responds at the same time at every heat flux setting.

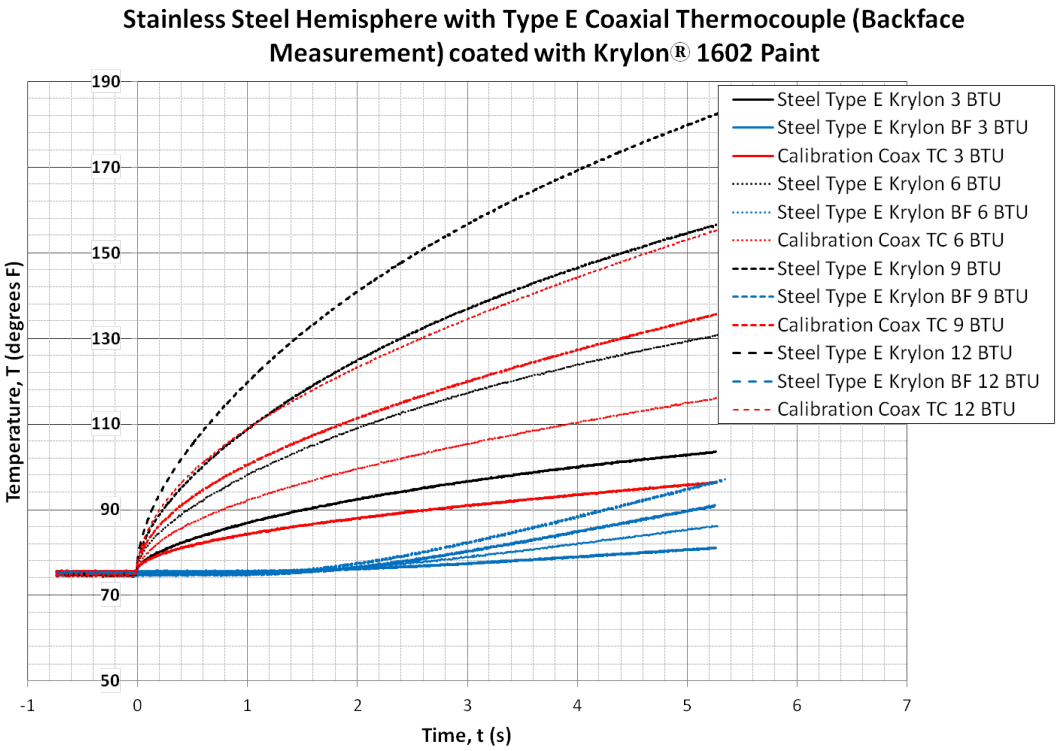

Figure 4-3. Temperature results for all the coaxial type E thermocouple in stainless steel at various heat flux settings.

To try and document the reason for the discrepancy between the coaxial thermocouple mounted in the stainless steel hemisphere versus the calibration thermocouple in the stainless steel calibration test fixture, a simple study of the planar assumption for inverse calculation was undertaken. Figure 4-4 compares the inverse method[9] used throughout this study to an inverse method that uses a tri-diagonal solver to solve for a transient 1-D heat conduction solution with either a planar or spherical assumption on the single dimension[32]. A heat flux output from one of the calibration Schmidt-Boelter sensors is also shown in black and the uncertainty on each inverse calculation is shown as the dotted line of the same color plotted with the heat flux.. The spherical solution with the blue line, as opposed to the planar solution in red, does in fact better match the actual heat flux, but does not accurately capture the slope of the heat flux when the lamp is on. During the course of a run, the lamp gets hotter as shown by the Schmidt-Boelter sensor. The uncertainties of the two inverse heat flux calculations are shown as well as dashed

lines of the same color of the data they pair with. Figure 4-4 illustrates that a spherical assumption is one piece of the discrepancy, but not the only one. Clearly, the geometry of the test article holding a heat flux sensor affects the results in a radiant heat flux calibration rig.

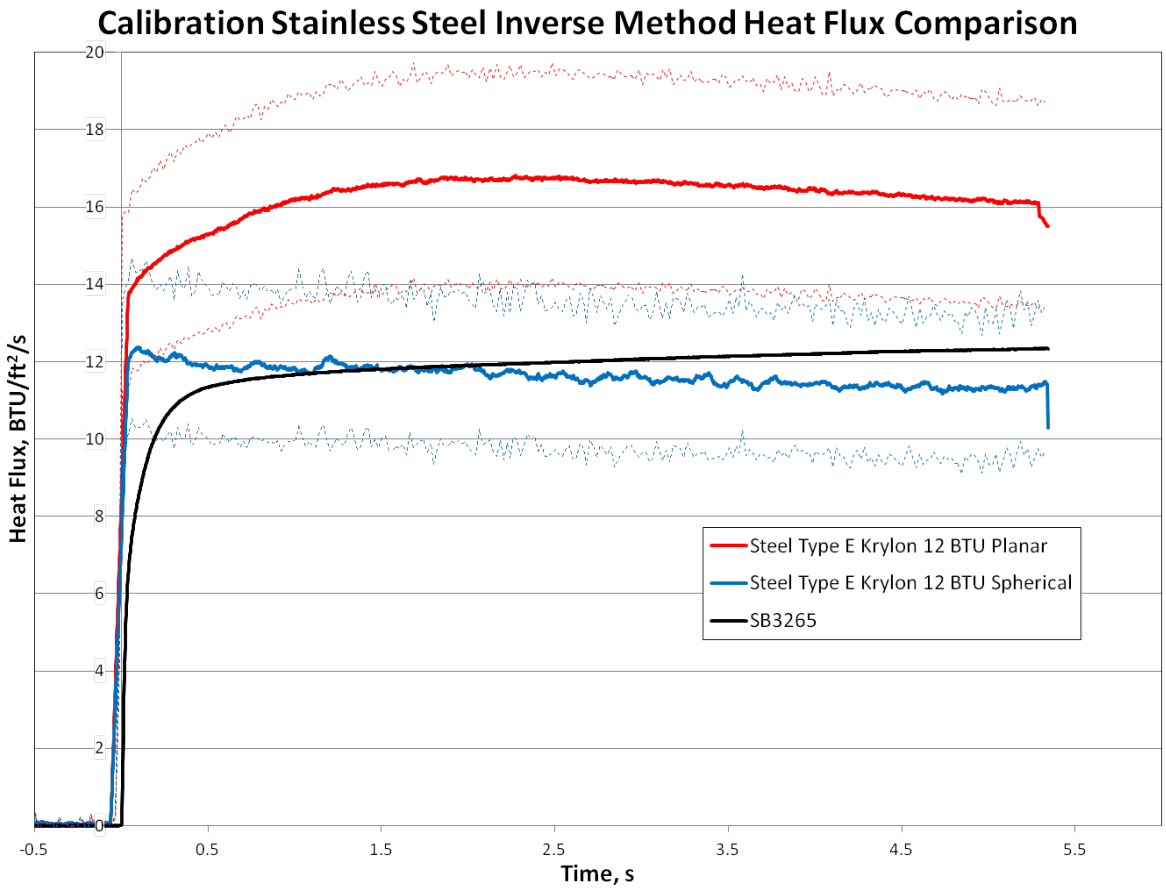

Figure 4-4. Comparison of Inverse Heat Flux methods for the coaxial thermocouple in the stainless hemisphere at 12 BTU/ft^2/s.

The choice of planar inverse or spherical inverse heat flux calculation is a discussion of the thermal environment the thermocouple will be measuring. Figure 4-5 is an illustration of the variations between a planar inverse heat flux, a spherical inverse heat flux, and the heat flux conditions in a VTHST run. In both the planar and spherical 1-D inverse methods, the wall temperature is assumed to be constant along the surface. The difference lies in the fact that the single dimension is radial and not planar.

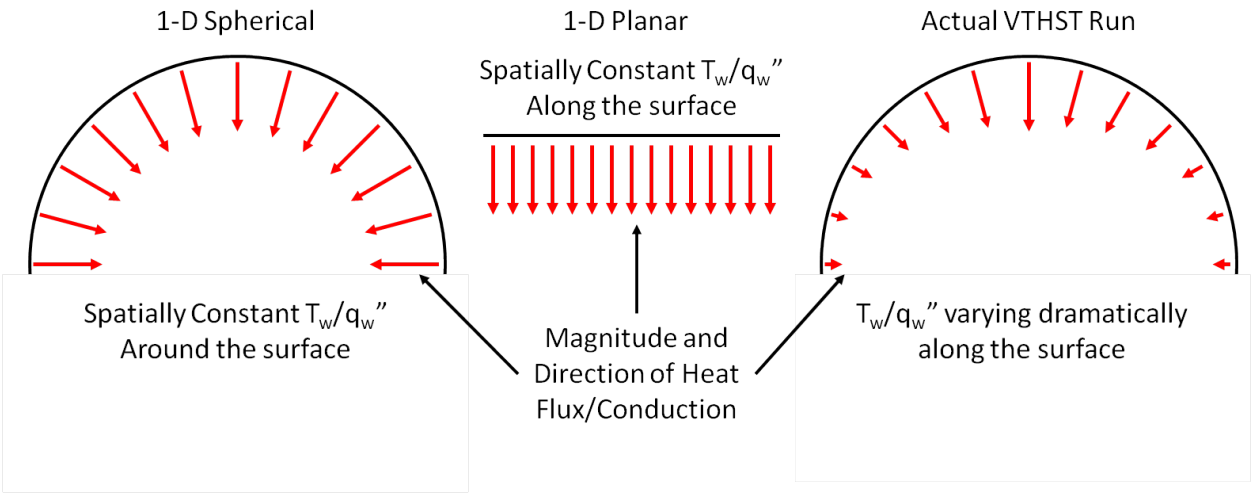

Figure 4-5. Changes in the geometry and assumptions between inverse heat flux methods and the VTHST.

The last part of the dynamic calibration involved the testing of the Schmidt-Boelter gages to determine their time constants. Table 4-2 documents the τ and τ^* measured during the dynamic testing of the three Schmidt-Boelter gages in their individual hemispheres.

	τ	τ^*
Stainless Steel	0.0157 s	0.0159 s
Graphite	0.0142 s	0.0151 s
MACOR	0.0100 s	0.0104 s

Table 4-2. The time constants for the three Schmidt-Boelter gages in their hemispheres.

The second calibration trip to the ATM lab was an effort to determine if the material that makes up the mounting block for the calibration test fixture has an effect on the measurements. When the MACOR® hemispheres are exposed to a heat flux, they increase in temperature at the surface much faster than a stainless steel hemisphere with the same applied heat flux. This means it is possible for the hot hemisphere to radiate into the cool test fixture block next to it. Figure 4-6 is a sketch of the possible radiation environment that could be created.

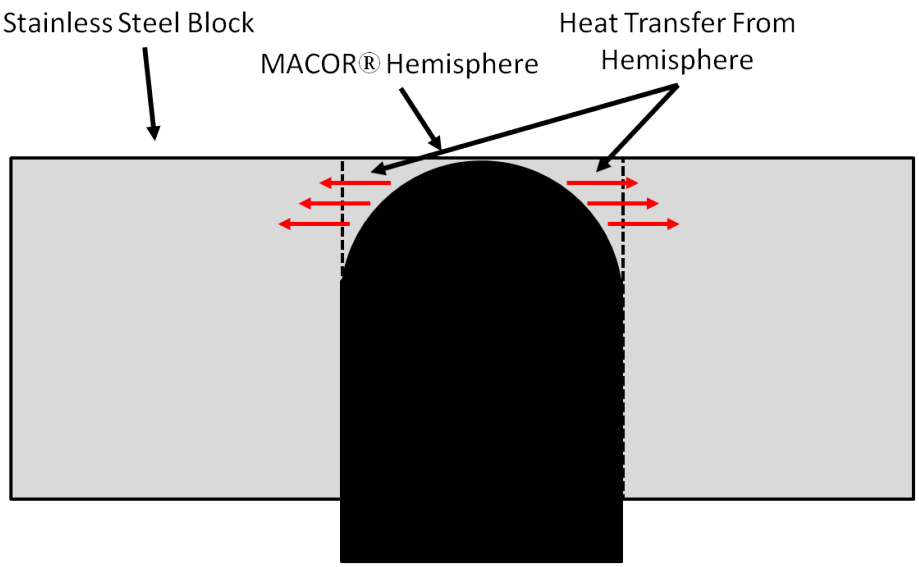

Figure 4-6. Possible external movement of thermal energy from the hemisphere.

Table 4-3 compares the differences in the temperature results of a temperature sensor in a MACOR® hemisphere mounted in the stainless steel calibration test fixture to the same sensor/hemisphere combination mounted in a MACOR® calibration test fixture at 12 BTU/ft^2/s. The MACOR® calibration test fixture does in fact keep energy from transferring away from the hemisphere, so the surface temperature of the hemisphere is higher by an average of 14%. The two temperature profiles were then used in an inverse[9] calculation to provide the corresponding heat flux for that sensor. Again, the results are documented in Table 4-3 shows these results with a 20% higher heat flux on average for the MACOR® test fixture.

	Mean % Change	σ % change
Temperature	14%	5.27%
Calculated Inverse Heat Flux	20%	15.34%

Table 4-3. Temperature and calculated inverse heat flux comparison between dynamic calibrations of a temperature sensor mounted in MACOR® sitting in a stainless steel block and a MACOR® block.

4.2 Wind Tunnel Results

In order to accurately compare results, each sensor/material combination was run in the VTHST at the same test conditions shown in Table 4-4.

Property	Value
M_∞	6
$p_{0\infty}$ (psi)	1200
$T_{0\infty}$ (R)	1188

Table 4-4. VTHST flow conditions for this study.

As documented in the set-up section, the average total pressure varies 8% throughout the on-condition time, but the run-to-run variance for all average flow properties is 1%. Initially the tunnel was only run for just over a second of on-condition time due to the possibility of un-start. After proving that it would not be a problem, later runs had just over two seconds on condition.

Note that all graphs have a zero start time that coincides with the opening of the quick release valve. The first 0.9 seconds is tunnel start-up with the plenum pressure, $p_{0\infty}$, the first to be on-condition since the transducer is well upstream of the test section. The dotted blue line indicates "on-condition" and the tunnel is back off-condition after three seconds.

Before presenting the VTHST results, an effort was made after collecting all the results to investigate various inverse heat flux calculation techniques to try and discover the reason for various discrepancies. This study is presented here in order to explain the choice of inverse method for the remainder of the results. First, to try and ascertain the reason for the discrepancy between the inverse heat flux calculated from the coaxial thermocouple mounted in stainless steel and the heat flux measured by the Schmidt-Boelter mounted in stainless steel, the Walker and Scott inverse method[9] was compared to a spherical 1-D inverse method[32]. In the calibrations, the switch from planar 1-D to spherical netted a positive result. In this case, as shown in Figure 4-7, the net decrease increased from 15% to almost 50% by the end of the run. The planar inverse calculation is red, the spherical inverse calculation is orange, the quasi-steady Fay-Riddell calculation is green, the Schmidt-Boelter gage mounted in stainless steel is black, and the percentage difference between the planar and spherical inverse methods is blue.

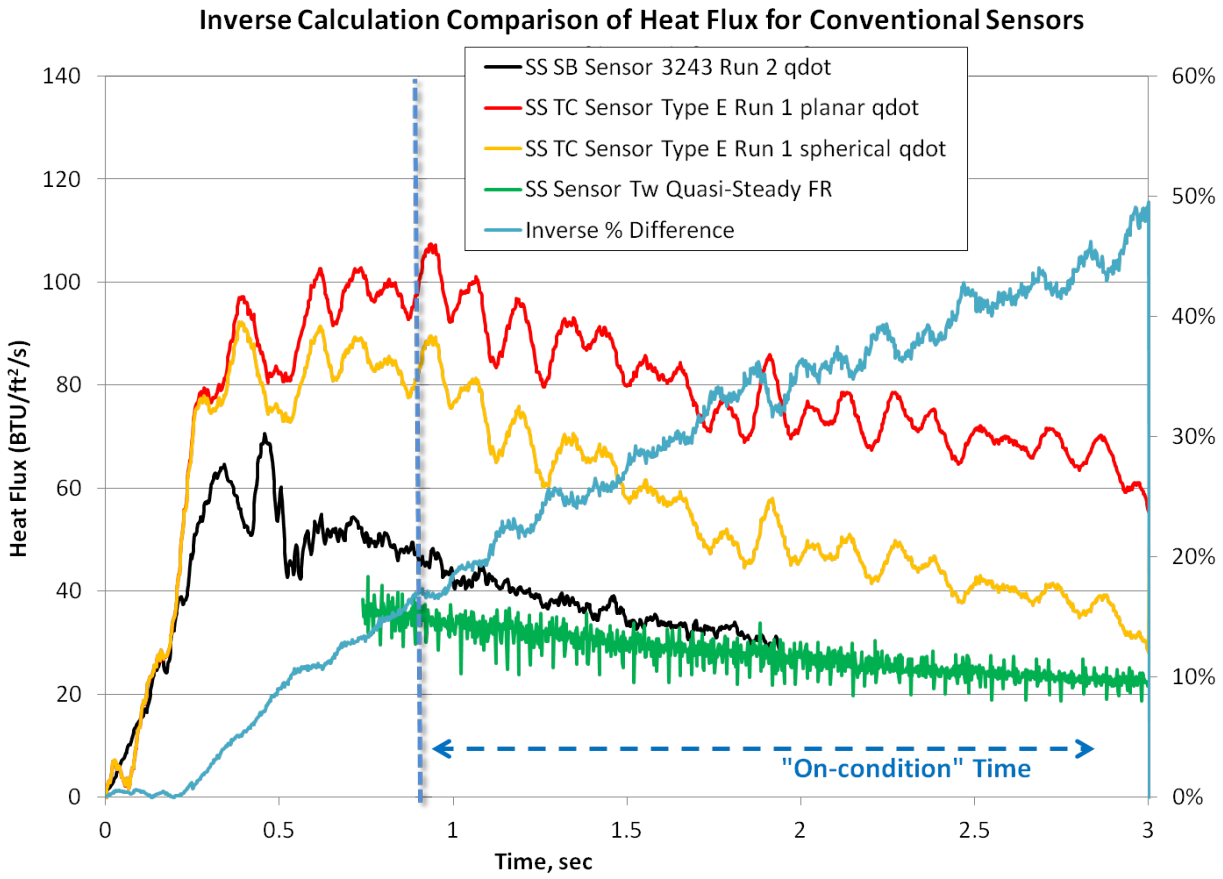

Figure 4-7. Spherical and Planar inverse heat flux method comparison for the MedTherm coaxial thermocouple in a stainless steel hemisphere.

The calculated spherical inverse does approach the quasi-steady Fay-Riddell solution by the end of the run, especially when the uncertainty for each of these calculations is taken into account, 13.14% for the Fay-Riddell and 16.41% for the inverse heat flux. But, when the actual heat flux environment is examined as shown in Figure 4-5, it is obvious that the physics of the spherical assumption are very different from the stagnation point heat flux on a small hemisphere. A spherical assumption assumes a uniform wall temperature around the radius and thermal energy penetrating normal to the curved surface. A planar assumption assumes a constant wall temperature on the flat surface with thermal energy uniformly penetrating down into the material. In the VTHST, the actual heat transfer physics are more similar to the planar one-dimensional heat conduction with the majority of the thermal energy coming in normal to the stagnation

point. The heat flux around the radius away from the stagnation point of the hemisphere falls off extremely rapidly.

At roughly 1.5 seconds during the runs in Figure 4-7, the rear face of the hemisphere had started to rise in temperature. Both of the inverse codes used in Figure 4-7 rely upon the rear temperature staying constant, called a semi-infinite assumption. An inverse heat flux code called "qcalc96", created by Colbish et. al.[18], has the capability of solving semi-infinite, or finite inverse heat flux problems, and also includes the ability to assume a planar, cylindrical, or spherical dimension. This inverse code uses a second-order, Euler-explicit, finite-difference method to solve the one-dimensional heat conduction problem[18]. Figure 4-8 presents heat flux results in the stainless steel hemisphere for the Schmidt-Boelter gage compared to various inverse heat flux calculations for the coaxial thermocouple. In this plot there are 5 different inverse heat flux calculations performed on the same coaxial thermocouple data.

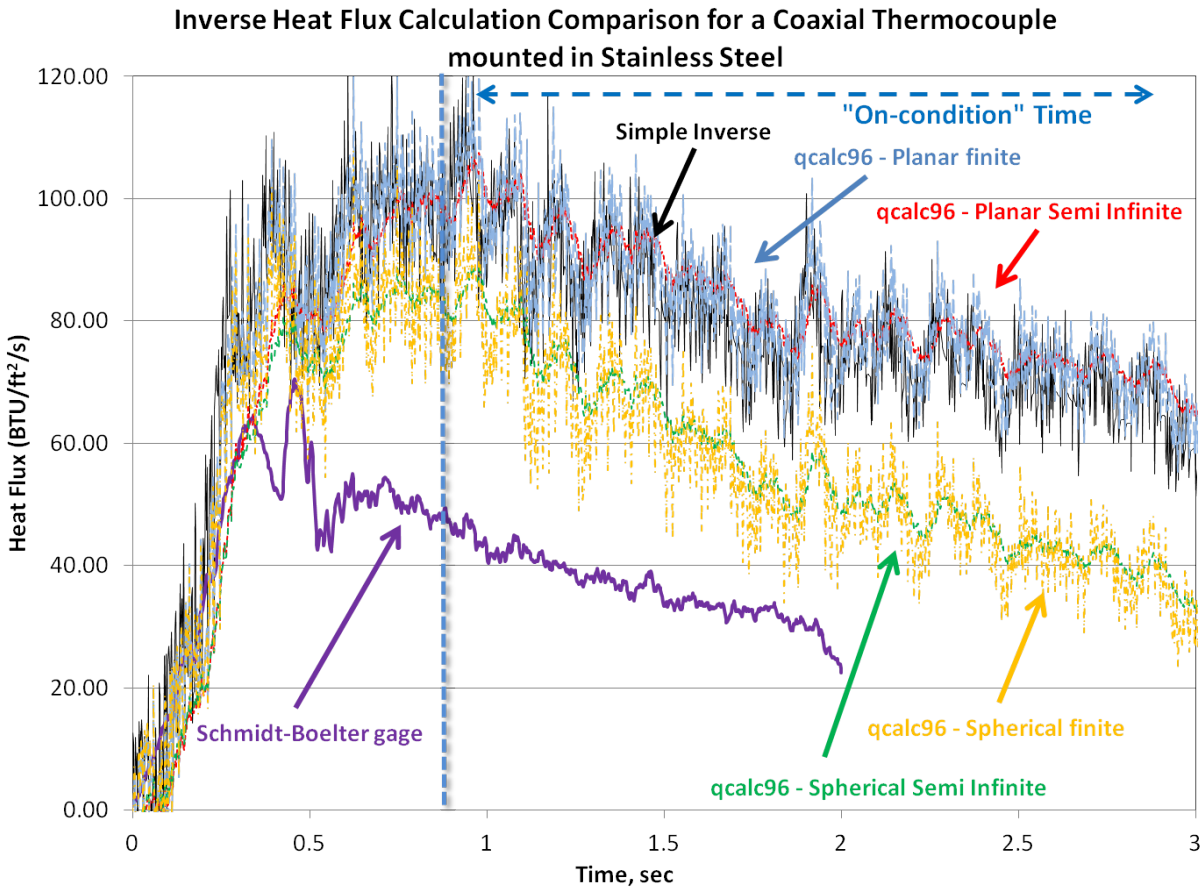

Figure 4-8. Spherical and Planar, Semi-infinite and finite inverse heat flux method comparison for the MedTherm coaxial thermocouple in a stainless steel hemisphere.

The black line is the predicted heat flux using the "Simple-Inverse Method" by Walker and Scott[9] which assumes a planar dimension and semi-infinite material. The red and green dashed lines are the "qcalc96" results assuming semi-infinite material, with the planar calculation in red and the spherical in green. The blue and orange dashed lines are the "qcalc96" results assuming 0.3 in. thick finite material, with the planar calculation in blue and the spherical in orange. Lastly, the purple line is the Schmidt-Boelter gage mounted in the stainless steel hemisphere.

The most interesting discovery in Figure 4-8 is that the move from a semi-infinite material to a finite material makes no apparent change to the calculated inverse heat flux. Much like in Figure 4-7, the spherical assumption does reduce the magnitude of the

calculated inverse heat flux, and the slope of the line. The fact that assuming the material was only 0.3 in. thick did not make a difference proves that there are other physics at play resulting in the over-prediction of heat flux using an one-dimensional inverse technique. The MACOR® and Graphite hemisphere coaxial thermocouples showed duplicate results with the various inverse techniques so the rest of the inverse heat flux calculations are using the "Simple-Inverse Method"[9] with planar and semi-infinite assumptions.

The temperature and heat flux plots of the VTHST in the following sections on coaxial thermocouples and Schmidt-Boelter gages follow the following patterns. The datum from sensors mounted in stainless steel hemispheres is black, from MACOR® hemispheres is blue, and from Graphite hemispheres is red. On the temperature graphs, the front temperature measurement is a line of the appropriate color and the rear temperature measurement is denoted by dots of the appropriate color. The heat flux plots include lines for all measurements and a fuchsia or purple line of constant heat flux which is a steady Fay-Riddell calculation for a wall temperature of 540° R[33].

4.2.1 Coaxial Thermocouple Results

Figure 4-9 is a plot of the temperature profiles for the $^{1}/_{16}$ in. MedTherm coaxial thermocouples in all three materials, with solid lines for the front temperature reading and dots for the rear.

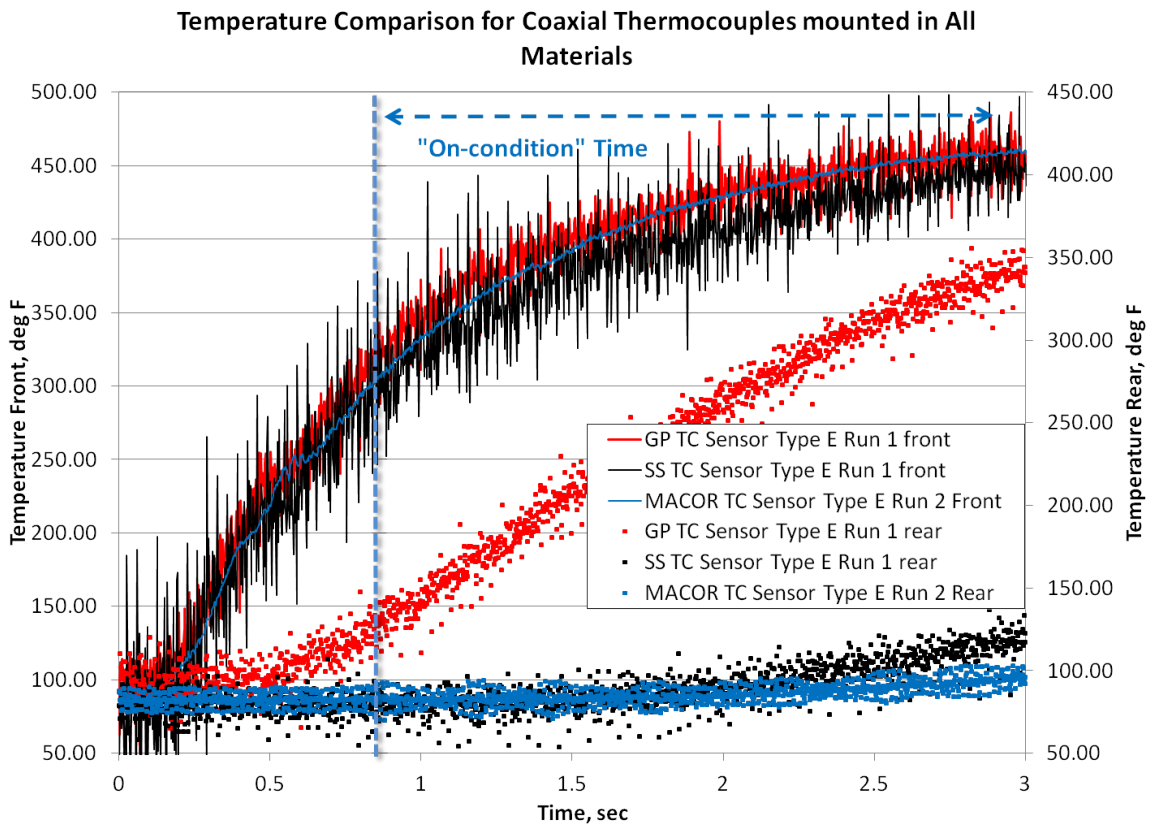

Figure 4-9. Coaxial thermocouple temperature comparison across different model materials.

It is quite noticeable that the front temperatures of the thermocouples are within 5% across all materials where as the rear temperatures follow the trends we would expect based on the thermal conductivity of the three materials. The variation in the level of noise between the three materials is also interesting and will be discussed in section 4.2.1.1.

Figure 4-10 plots the calculated heat flux for all temperature profiles in Figure 4-9 using the inverse method by developed by Walker and Scott[9]. The fuchsia line is the steady Fay-Riddell prediction calculated with a T_w of 540° R[33]. Because the temperature profiles overlaid as shown in Figure 4-9, any difference between the three materials is purely the change in thermal properties used in the inverse heat flux calculation.

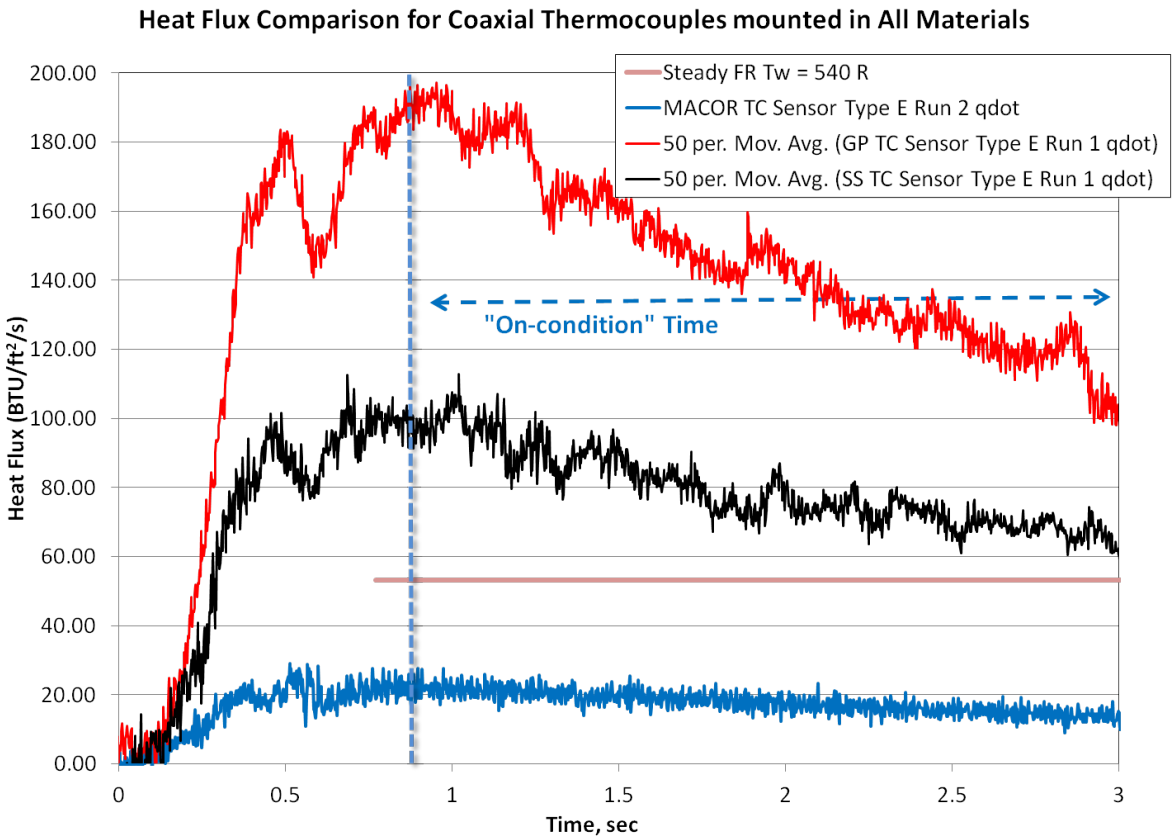

Figure 4-10. Coaxial thermocouple heat flux comparison across different model materials.

While it is expected that the MACOR® hemisphere would have the lowest q_w'' and the graphite hemisphere the highest due to the inverse relationship between thermal conductivity and wall temperature, the extremely high heat flux for the graphite hemisphere is not physical. Due to the higher noise present in the stainless steel and graphite thermocouple data, the inverse heat flux was averaged every 50 points to present a better comparison.

4.2.1.1 Coaxial Thermocouple Noise

To better understand the high noise present in the temperature from the coaxial thermocouple in the stainless steel and graphite hemispheres, a study of the noise was undertaken. A Fast Fourier Transform (FFT)[31] was performed on the data of all sensors in this test in order to ascertain whether the noise was flow related and random, or

structured and due to external interference. Figure 4-11 shows the results of the FFT for the coaxial thermocouple in the stainless steel hemisphere.

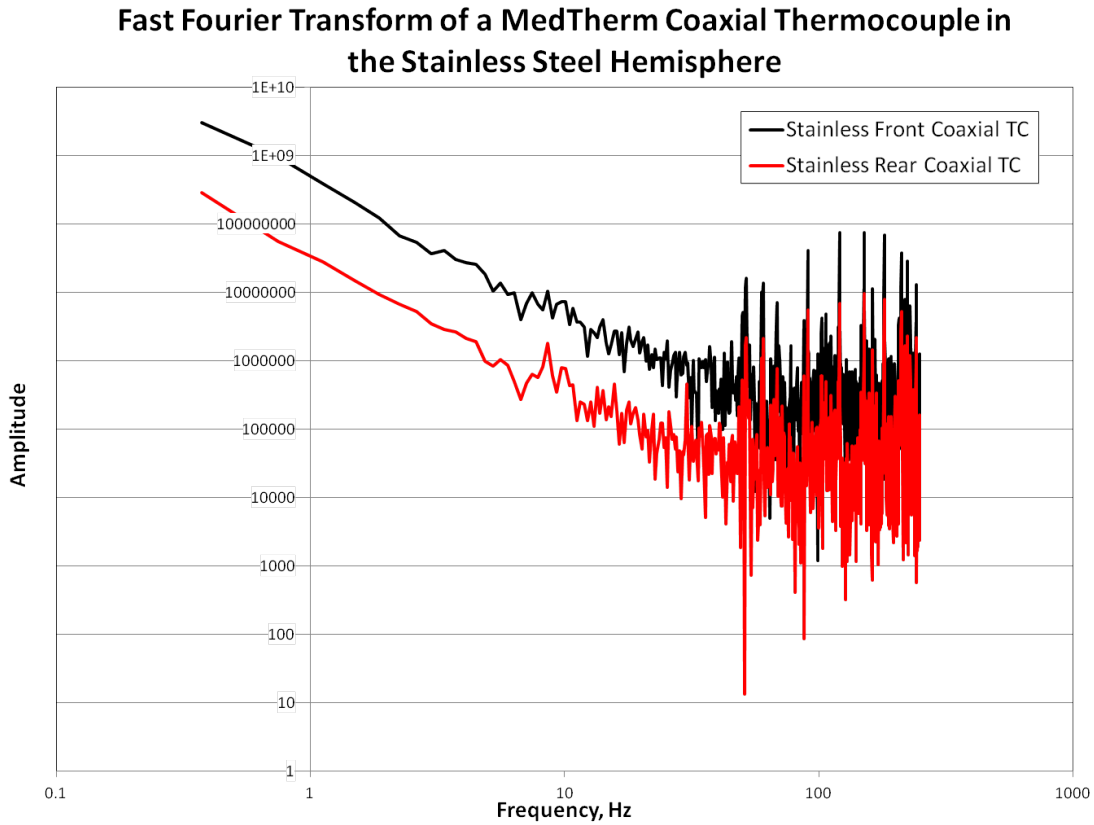

Figure 4-11. FFT of the front and rear temperature for the MedTherm coaxial thermocouple in the stainless steel hemisphere.

This result does show that there is noise present in the thermocouple signal that has a pattern. This noise is most likely a vibration in the test fixture itself that is magnified by the moment arm of the mount for the hemisphere models. The increase in noise from the rear to front temperature signal supports this conclusion.

The MACOR® hemisphere did not appear to have the same level of noise, so an FFT of the front and rear temperature data from the MACOR® hemisphere coaxial thermocouple was calculated. Figure 4-12 shows this FFT.

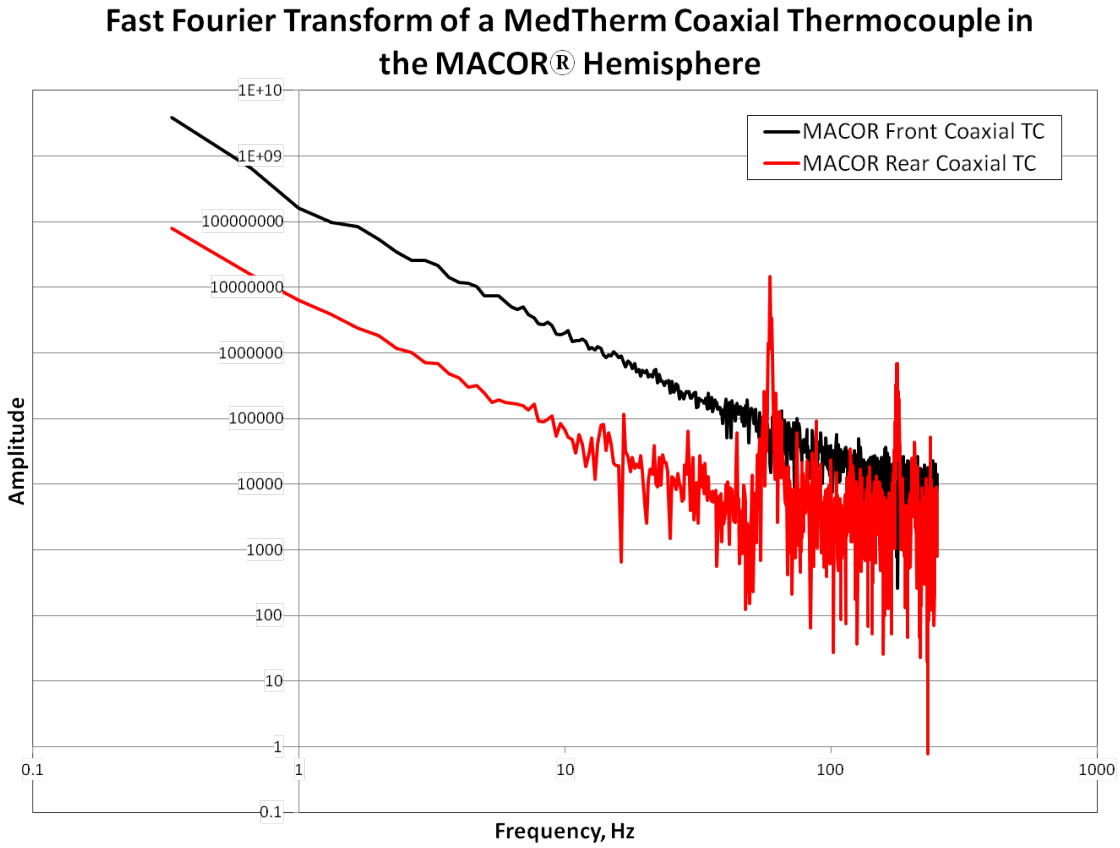

Figure 4-12. FFT of the front and rear temperature for the MedTherm coaxial thermocouple in the MACOR® hemisphere.

The front signal has none of the spikes in amplitude that were present in the stainless steel data. The rear temperature signal does have some noise in the 60 Hz and 175 Hz range, but the amplitudes are much lower than those present in the rear temperature signal from the stainless steel hemisphere.

Because the MACOR® hemisphere did not have the same level of noise as the stainless hemisphere, FFTs of the front temperature signals from the MACOR® hemisphere coaxial thermocouple, the stainless steel hemisphere thermocouple, and the graphite hemisphere thermocouple were plotted in Figure 4-13.

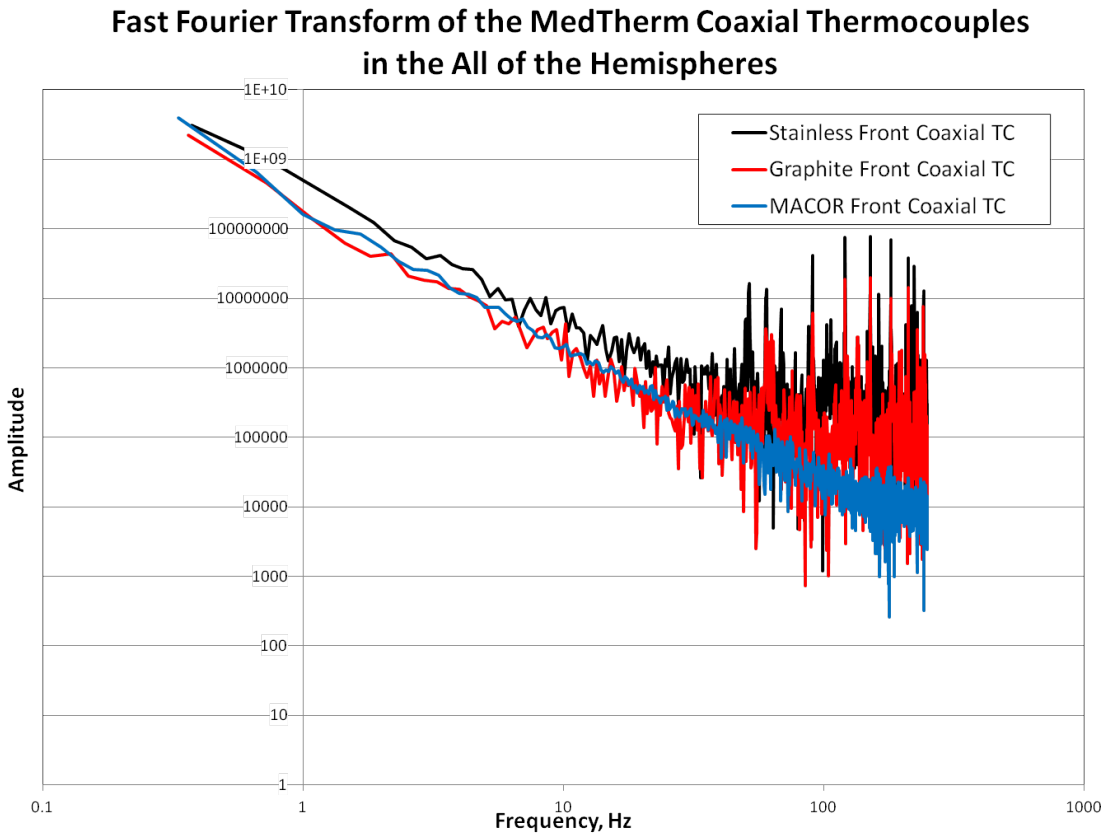

Figure 4-13. FFTs of the front temperature data for the MedTherm coaxial thermocouples in the MACOR®, Stainless, and Graphite hemispheres.

The thermocouple in stainless steel shows the largest amplitude of noise, the MACOR® mounted thermocouple does not appear to have any of the same noise, and the graphite mounted thermocouple signal contained most of the same noise as the stainless data, but at lower amplitudes. This eliminates alternating current noise or the noise of any switching power supplies on the signals, as well as vibration affecting the data acquisition system. These large differences can only point to acoustic vibrations of the actual sensor as the cause. The reason that the identical external geometry sensors show different levels of noise is due to the construction of the models themselves as shown in Figure 2-4. The stainless steel model is a one-piece design so that any vibration can be transmitted without dampening all the way to the front of the hemisphere. The graphite and MACOR® models are actually composed of two pieces with a high-temperature gasket material in between the hemisphere and the stainless steel cylinder that is attached

to the test fixture, as shown in Figure 2-4 and Figure 2-5. In the case of the graphite, the hemisphere itself had such a tight friction fit that removal of the hemisphere without damaging it, could never take place. This strong connection allowed the dampening of the gasket material to be reduced such that the coaxial thermocouple for the graphite model still shows the noise present in the stainless data.

If the noise was only acoustic vibrations affecting the thermocouple data in the hemispheres, the Pitot pressure transducer measuring p_{02} should demonstrate little to no noise, or different noise, as the transducer is mounted on the outside of the test section. Moreover, the total temperature probe measuring T_{02}/ T_{01}/ $T_{0\infty}$ should pick up on some of the vibrations as it is mounted on the test fixture near the end of a tube. Figure 4-14 plots a comparison between the FFTs of the front temperature data from the coaxial thermocouple in the stainless steel hemisphere, the pressure data from the Pitot tube, and the temperature data from the total temperature probe. The pressure transducer does not show the same structure of noise as the coaxial thermocouple in the stainless steel hemisphere. The total temperature measured by the total temperature probe does in fact pick up on the same noise at the higher frequencies at much reduced amplitude. This does confirm the hypothesis that the added noise is simply acoustic vibration from the running tunnel. Steps were taken early on to reduce the vibration of the test fixture with beams added to the top of the mount for stiffness and mass.

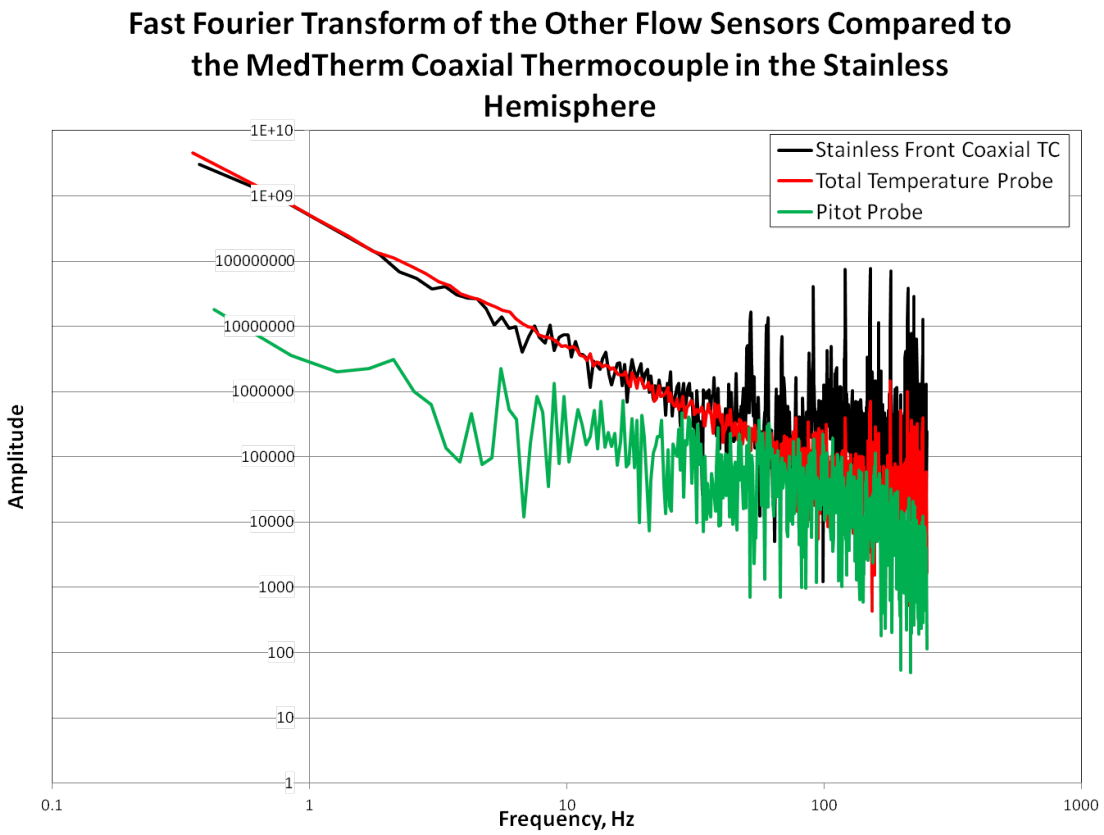

Figure 4-14. FFTs of the coaxial thermocouple in the stainless steel hemisphere, the pitot tube transducer, and the total temperature probe thermocouple.

In order to determine to the true impact of the noise present in the various signals, the fast Fourier transforms were integrated and compared to fast Fourier transforms of the signals without the noise. Table 4-5 shows the percentage of the energy due to the noise. Interestingly, while the pitot pressure signal appeared to have very little noise, the percentage of noise present was the highest at 2.13%.

Sensor	Noise % of the Energy
Stainless Steel Hemisphere Front Thermocouple	0.0451%
Stainless Steel Hemisphere Rear Thermocouple	0.6000%
MACOR® Hemisphere Front Thermocouple	0.0023%
MACOR® Hemisphere Rear Thermocouple	0.2100%
Graphite Hemisphere Front Thermocouple	0.0655%
Graphite Hemisphere Rear Thermocouple	0.0376%
Pitot Pressure Transducer	2.1300%
Total Temperature Prope	0.0028%

Table 4-5. Percentage of the energy that is the apparent noise.

Given the low percentages of noise actually present within the signals, signal conditioning such as averaging was used throughout this study as the majority of the energy occurs in frequencies below 10 Hz.

4.2.2 Fast Response Schmidt-Boelter Gage Results

Figure 4-15 plots the measured heat flux for the Schmidt-Boelter gages in all three materials. As referenced above, the stainless steel hemisphere is represented in black, the MACOR® hemisphere is represented in blue, and the Graphite hemisphere is represented in red. The purple line is the steady Fay-Riddell calculated with a T_w of 540° R[33].

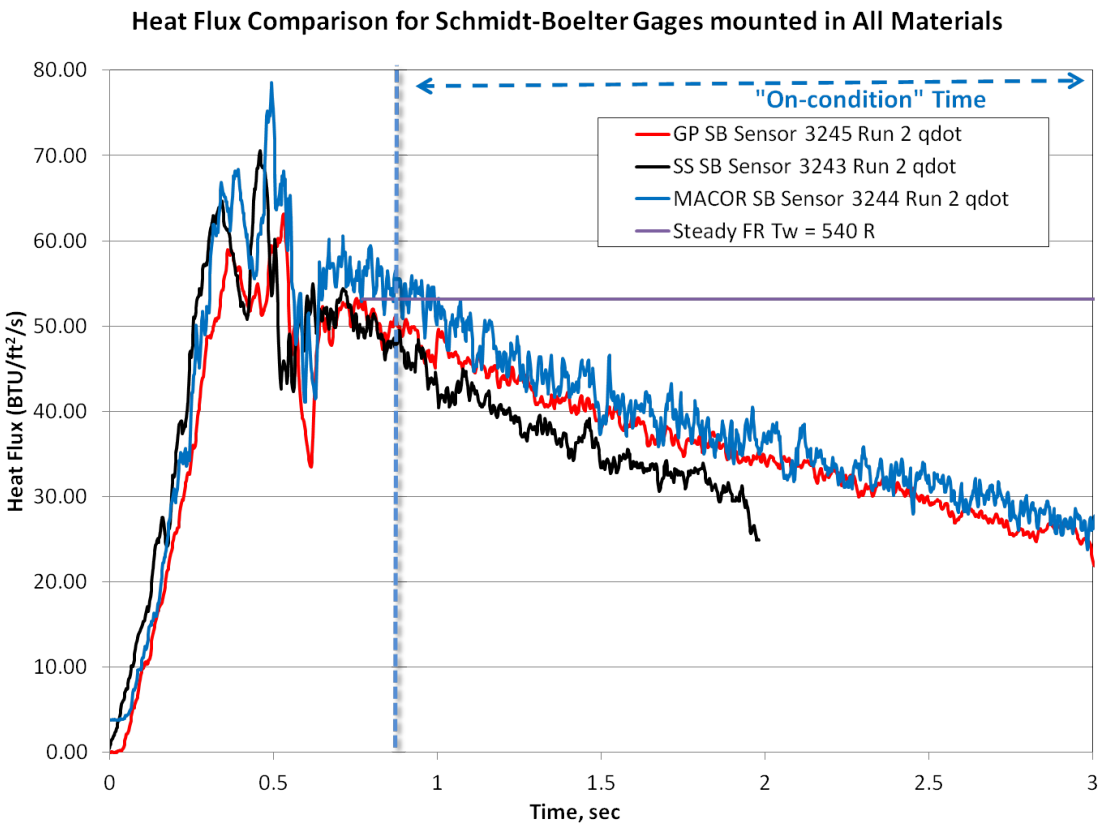

Figure 4-15. Schmidt-Boelter gage heat flux comparison across different model materials.

Theory predicts that stagnation heat flux on the MACOR® hemisphere should be the lowest due to the highest wall temperatures, and the Graphite hemisphere should have the lowest wall temperatures and correspondingly have the highest stagnation heat flux. The fast response Schmidt-Bolter gages in this study were designed to be installed in stainless steel models. Figure 4-15 illustrates that these sensors are being used outside of that intended application. The extremely close responses out of the three materials is well within the 13.18% uncertainty for the Schmidt-Boelter gage heat flux measurements. This response is similar to that of the coaxial thermocouples where it I possible that there is poor thermal contact between the sensors and the hemispheres.

Figure 4-16 plots the temperature profiles for the Schmidt-Boelter gages in all three materials, with solid lines for the front temperature reading and dots for the rear. The fast

response Schmidt-Boelter gages from AEDC include a rear thermocouple, but the front temperature is calculated by a combination of the measured heat flux and the measured rear temperature as specified by the manufacturer.

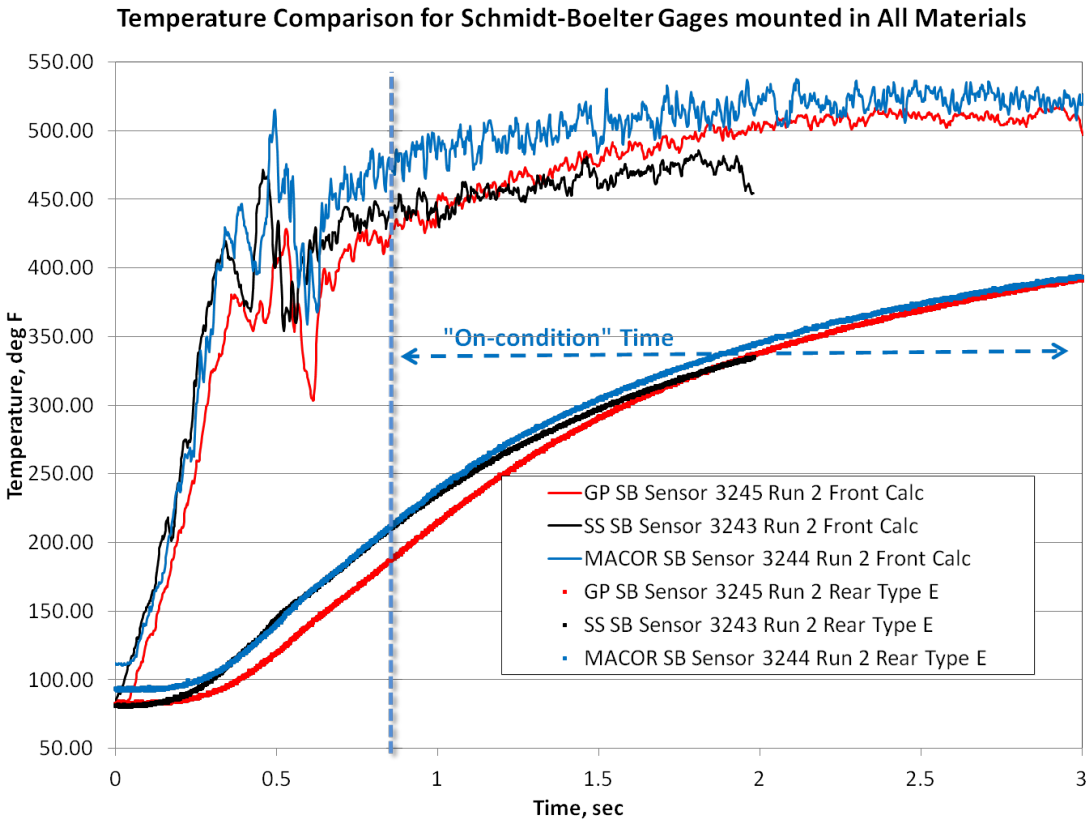

Figure 4-16. Schmidt-Boelter gage temperature comparison across different model materials.

The rear temperatures are very close to one another, illustrating either a design feature of the Schmidt-Boelter gage, isolation, or poor thermal contact. Most likely it is isolation as the depth of the back side thermocouple is much closer to the surface than the rear measurement on the coaxial thermocouples. The front temperatures vary by roughly 50 degrees R, but the front temperature of the MACOR mounted Schmidt-Boelter gage exceeded the temperature capability of the adhesive at 520° F. Also, since the temperature exceeded the thermal specification, the thickness of the adhesive layer was most likely changed so that the equation to calculate the front temperature was most

likely wrong for that sensor, and probably calculated low. Because of this, that sensor was recalibrated and all data updated off the new calibration.

4.3 Model Material Comparisons

In order to facilitate comparisons across sensor types, the data presented above is presented again organized by model material.

The temperature and heat flux plots of the VTHST in the following sections comparing sensors in a single material follow the following patterns. The data from the coaxial thermocouples is red and from the Schmidt-Boelter gages is black. On the temperature graphs, the front temperature measurement is a line of the appropriate color and the rear temperature measurement is denoted by dots of the appropriate color. Each heat flux plot will also have the prediction of stagnation heat flux from a quasi-steady Fay-Riddell[33] calculation plotted in green.

4.3.1 Stainless Steel Hemisphere Model

Figure 4-17 shows the temperature results for the Schmidt-Boelter and the coaxial thermocouple mounted in their respective stainless hemispheres. Note that the "front" temperature for the Schmidt-Boelter is a calculated front temperature based on the thickness and material properties of the insulator, and is provided by the manufacturer.

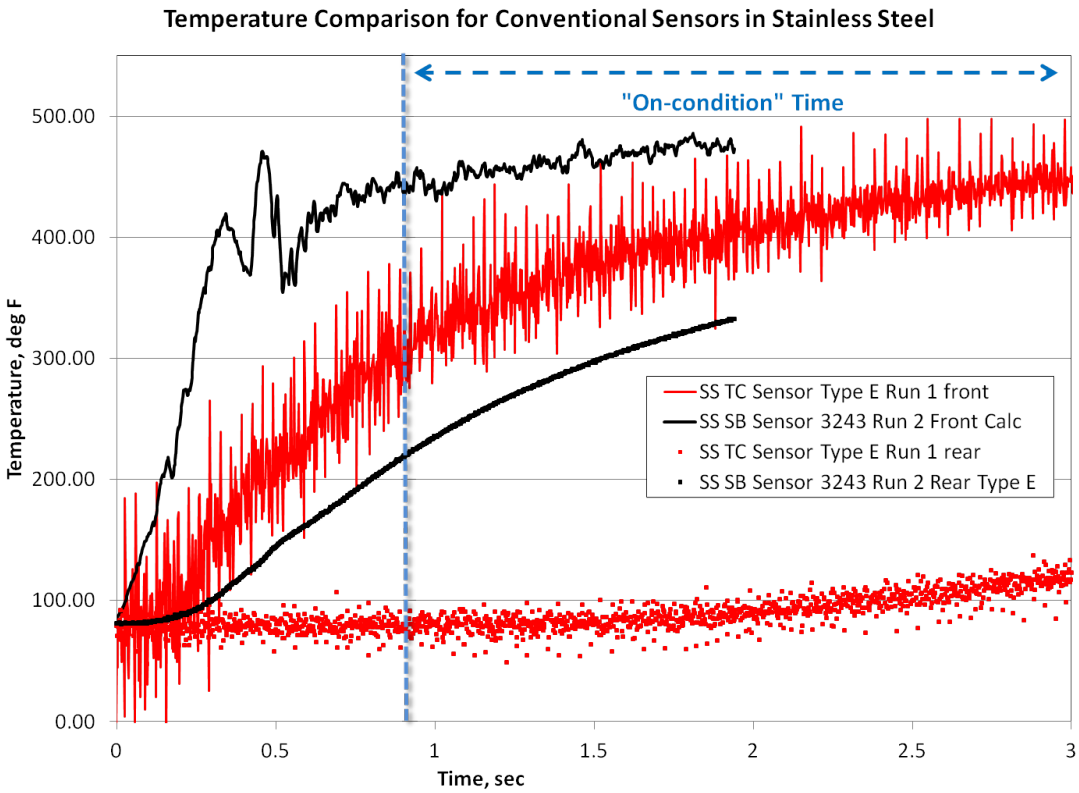

Figure 4-17. Stainless steel model temperature comparison.

Roughly a half second into the on-condition run, the temperature has started to rise on the back temperature measurement for the thermocouple. This means that the heat has penetrated to the back face of the hemisphere and that a semi-infinite assumption for the inverse calculation is no longer valid.

In Figure 4-18 the heat flux output from the Schmidt-Boelter gage is compared to an inverse[9] calculation of the thermocouple data. As a check, a quasi-steady Fay-Riddell prediction was calculated using the wall temperatures from the coaxial thermocouple. The Schmidt-Boelter gage results in black and the quasi-steady Fay-Riddell prediction in green agree, as expected. What is interesting is that the simple inverse of the thermocouple temperature result is about two times greater than either the Fay-Riddell or the Schmidt-Boelter gage heat flux. As shown in Figure 4-8, this is not the result of either the planar, or semi-infinite assumption. This discrepancy can only be caused by physics that are not captured by any one-dimensional inverse heat flux calculation.

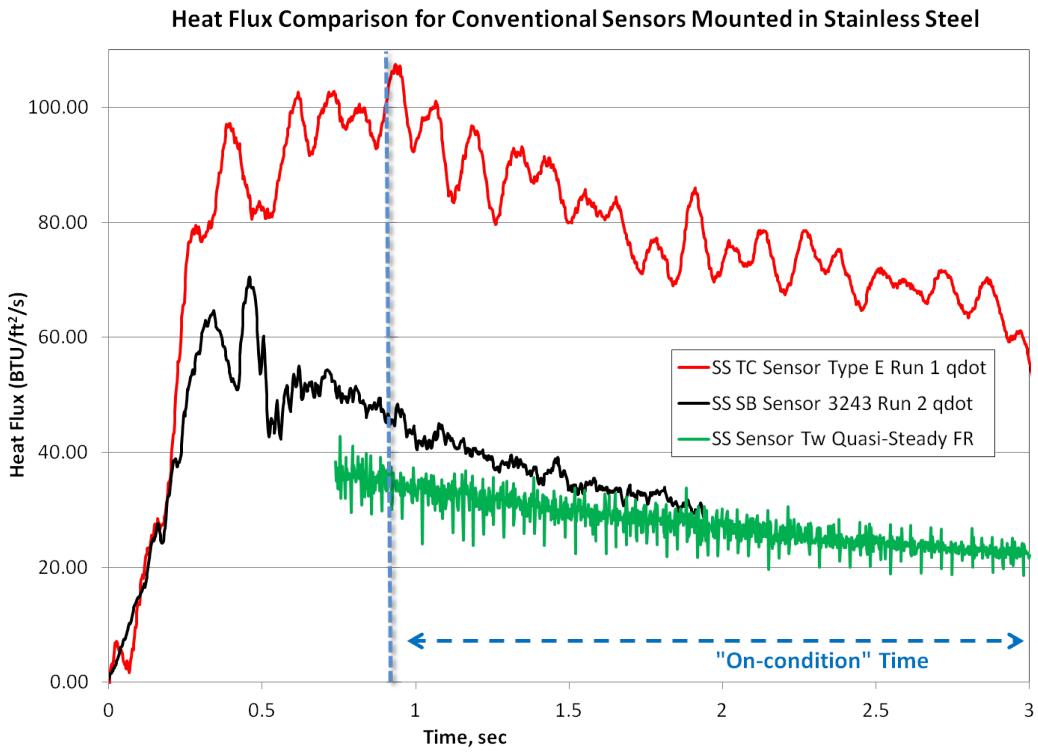

Figure 4-18. Stainless steel model heat flux comparison.

4.3.2 Graphite Hemisphere Model

Figure 4-19 shows the temperature results for the Schmidt-Boelter gage and the coaxial thermocouple mounted in their respective graphite hemispheres. Just as for the stainless steel hemispheres, the "front" temperature for the Schmidt-Boelter is a calculated front temperature based on the thickness and material properties of the insulator. Also, the conventions for dots and colors remain the same as the stainless steel model graphs.

Roughly a half second into run, before the tunnel is on-condition, the temperature has started to rise on the back temperature measurement for the thermocouple. This means that the heat has penetrated to the back face of the hemisphere during tunnel start-up and that a semi-infinite assumption for the inverse calculation is not valid for the entire "on-condition" portion of the run.

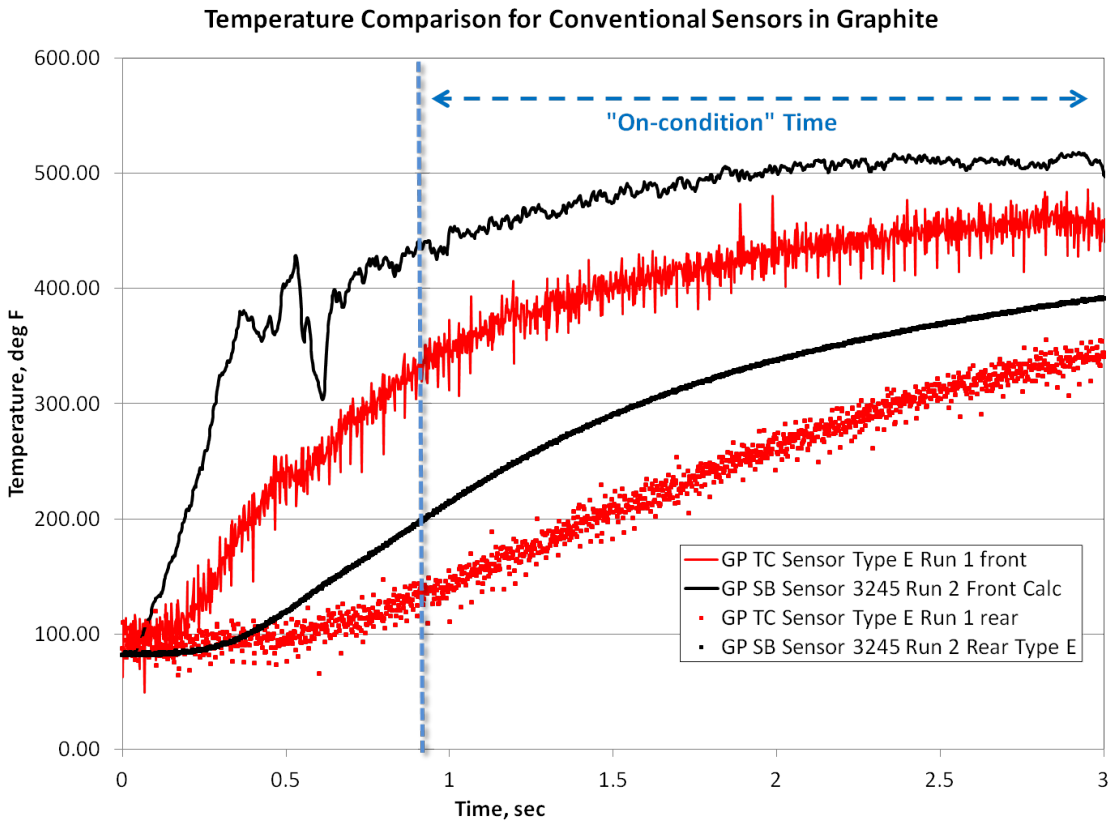

Figure 4-19. Graphite model temperature comparison.

In Figure 4-20 the heat flux output from the Schmidt-Boelter gage is compared to an inverse calculation[9] of the thermocouple data. Again a quasi-steady Fay-Riddell prediction was calculated[33], but in this case the wall temperature comes from the rear thermocouple on the Schmidt-Boelter gage due to the problematic high temperatures in the coaxial thermocouple in Graphite. Of note is the drop in heat flux that occurs at t=0.52 s. This corresponds to the time when the backface of the hemisphere has started to rise in temperature. After that initial drop, the slope turns positive again as the complex geometry of the Graphite hemisphere, stainless steel cylinder, and gasket material overwhelms the one-dimensional assumptions on the inverse heat flux calculation. The Schmidt-Boelter and the Fay-Riddell results agree, but that is due to the use of the rear Schmidt-Boelter gage thermocouple data for the Fay-Riddell calculation. In fact, the Schmidt-Boelter gage is optimized for mounting in stainless steel not Graphite, so the measured heat flux is lower than expected.

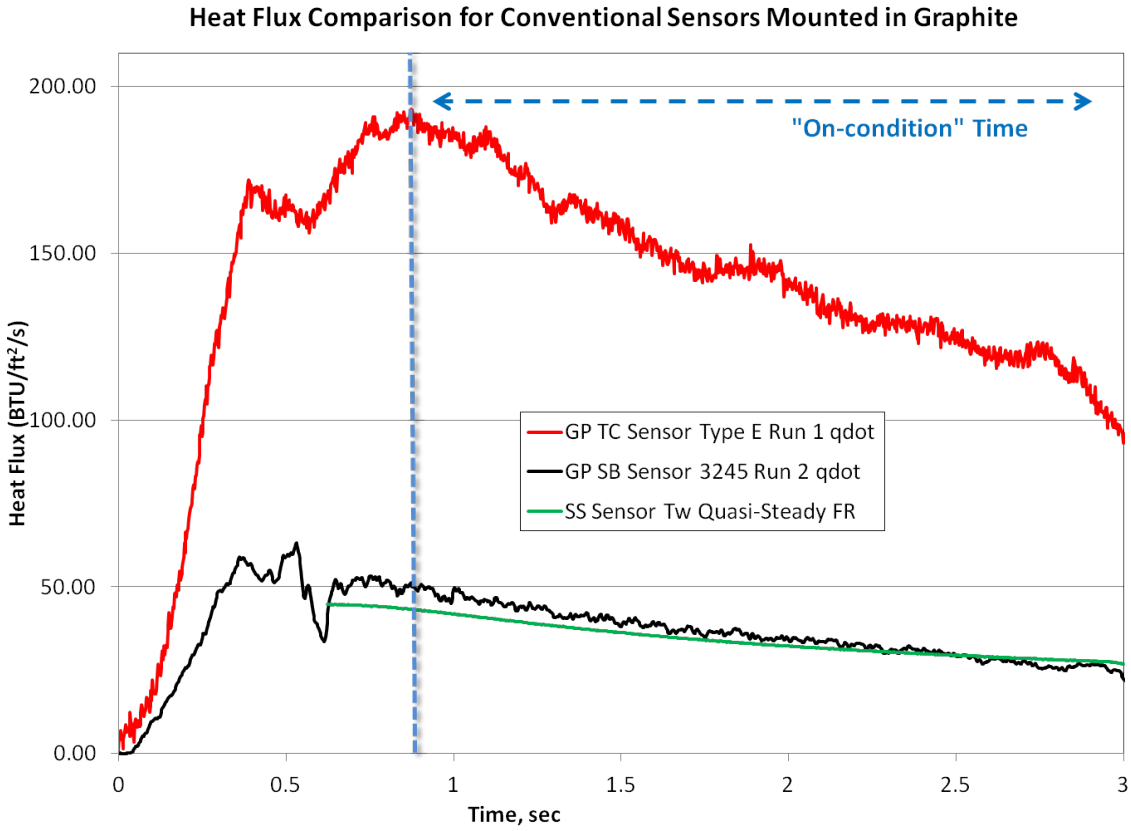

Figure 4-20. Graphite model heat flux comparison.

4.3.3 MACOR® Hemisphere Model

Figure 4-21 shows the temperature results for the Schmidt-Boelter gage and the coaxial thermocouple mounted in their respective MACOR® hemispheres. Again, the "front" temperature for the Schmidt-Boelter is a calculated front temperature based on the thickness and material properties of the insulator. Also, the conventions for dots and colors remain the same as in the stainless steel and Graphite graphs.

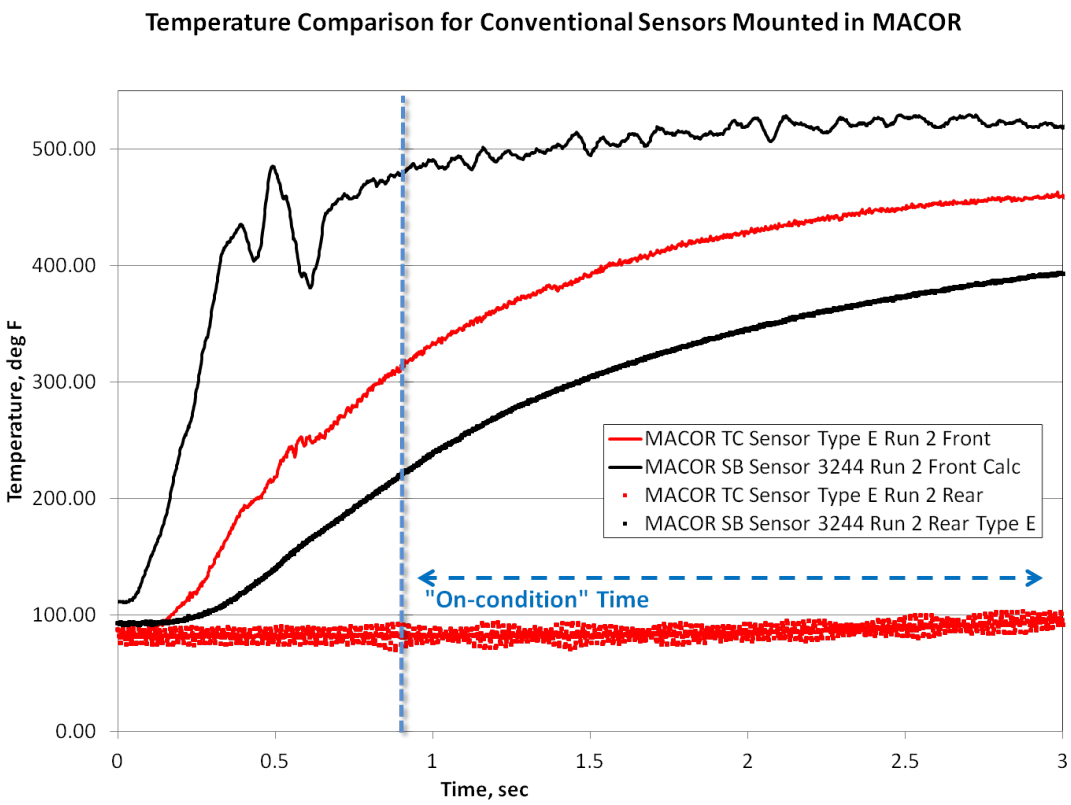

Figure 4-21. MACOR® model temperature comparison.

Due to the extremely low thermal conductivity of MACOR®, the backface of the hemisphere does not experience a change in temperature from ambient until t=2.5 s, and even then there is only a 10° F rise by the end of the run. For MACOR®, the semi-infinite assumption used in the inverse calculation is a very good assumption. Also, the calculated front temperature for the Schmidt-Boelter reaches above 520° F. The adhesive used to secure the thermopile to the insulator begins to melt at 520° F. Because of this, this Schmidt-Boelter gage was recalibrated after the wind tunnel runs and showed a 10% decrease in the slope of the q_w''/mV equation. The plotted values take this correction into account as the shift happened quite obviously in the first run.

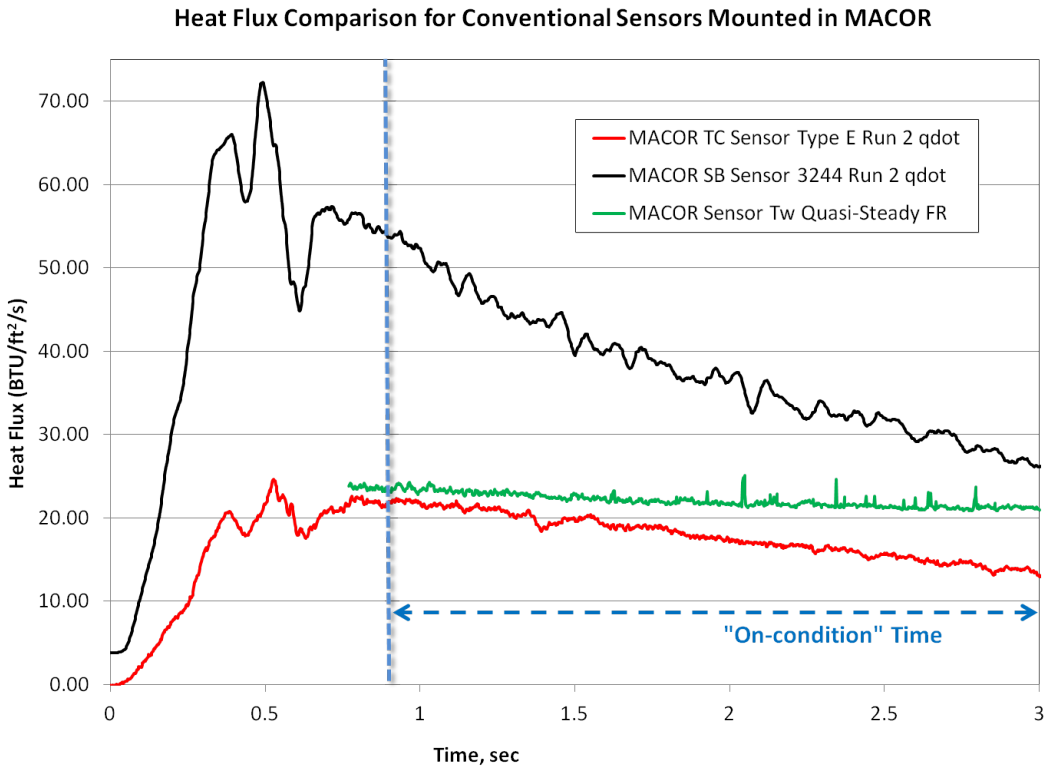

Figure 4-22. MACOR® model heat flux comparison.

In Figure 4-22 the heat flux output from the Schmidt-Boelter gage is compared to an inverse calculation[9] of the thermocouple data. Again a quasi-steady Fay-Riddell prediction was calculated using the wall temperatures from the coaxial thermocouple as a check and is plotted in green. In this case it seems that the inverse method produces the best results when compared to the Fay-Riddell calculation. But, this might be a false promise as the quasi-steady nature of the Fay-Riddell calculation can not accurately account for the rapid temperature rise that happens on the surface of the MACOR® hemisphere. Also, the front temperature measured by the coaxial thermocouple in Figure 4-21 is not accurate as was shown in Figure 4-9 due to poor thermal contact. Because of this, the slope is off as well which affects the inverse heat flux calculation. The Schmidt-Boelter gage reads extremely high, since the very hot ceramic around the metal sensor changes the front reading while the isolated rear measurement remains low, artificially raising the measured heat flux.

5. Computational Results

The following chapter documents the results of the modeled wind tunnel runs using CFD with CHT. The setup and details of the simulation are covered in Chapter 3, Computational and Analytic Methods.

The graphs in this section conform to the following guidelines. For the temperature and heat flux plots, the stainless steel hemisphere data is blue, and MACOR is green, and the graphite is red. For these temperature plots, the surface temperature is solid and the backface temperature is dashed. For the heat flux plots, the heat flux output from GASP at the stagnation point is the solid line. The dashed line is either the inverse method calculated heat flux, or the calculation of a heat flux in the same was a Schmidt-Boelter gage measures heat flux. The modeled indirect sensors, thermocouple, fiber, and perfect, use the inverse technique for heat flux calculation, and the modeled direct sensor, the Schmidt-Boelter gage, uses the "measurement" calculation.

For the cross-section contour plots, the upper left time is 0.5 s, the upper right is 1.0 s, the lower left is 1.5 s, and the lower right is 2.0 s into the simulation. The top legend for these plots is the temperature scale for the fluid, the bottom is the temperature scale for the solid, and the legend to the right depicts the scaling for the fluid Mach number contours.

5.1 Coaxial Thermocouple Surrogate

A surrogate of the 1/16 in. MedTherm coaxial thermocouple was simulated at the wind tunnel conditions in each of the hemisphere materials. Figure 5-1 shows the temperature results of the various simulated sensors at the test condition. As mentioned above, the stainless steel hemisphere data is blue, and MACOR is green, and the graphite is red. The surface temperature is solid and the backface temperature is dashed. With the thinner, $^1/_8$ in., hemisphere, the back surface temperatures rise much sooner. The

temperature on the backface of the Graphite hemisphere is rising after 0.08 s, the stainless steel backface temperature rises after 0.2 s, and the MACOR® hemisphere's backface rises after 0.24 s. All of these temperatures are measured $^{1}/_{8}$ in. deep on the centerline of the modeled chromel thermocouple.

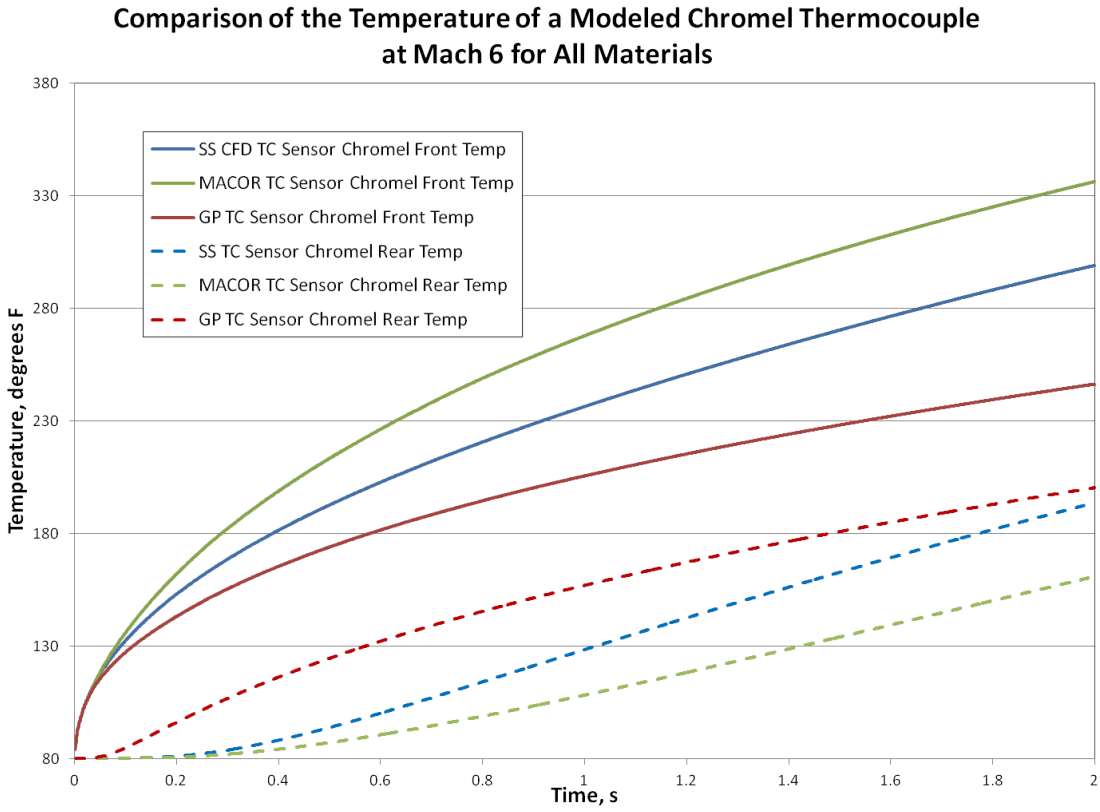

Figure 5-1. Simulated Mach 6 wind tunnel run temperature profile for a modeled chromel sensor with different model materials.

Figure 5-2 shows the heat flux output from GASP compared to the inverse method[9] calculation of each of the sensors. The heat flux output from GASP for each material is the solid line and the calculated heat flux for each material is the dashed line. None of the inverse heat flux calculations are able to recover actual heat flux due to the failure of the semi-infinite assumption, but as expected due to the close material matching, the inverse of the stainless steel hemisphere is the closest to the simulated heat flux.

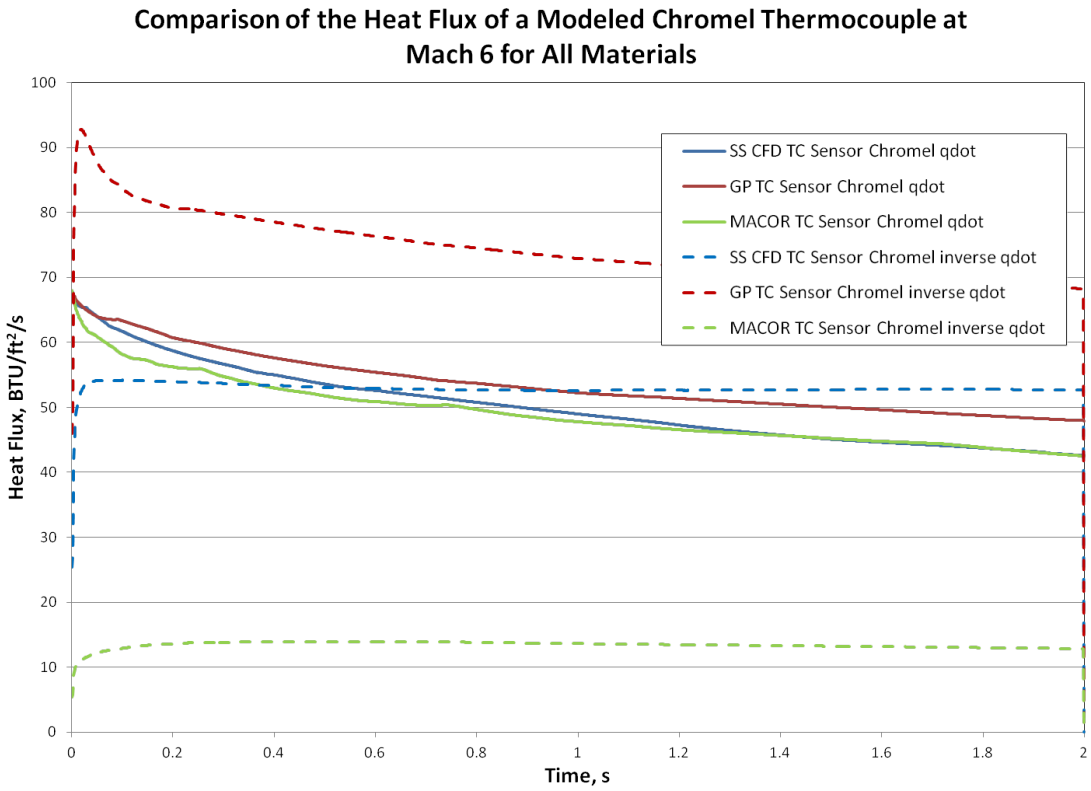

Figure 5-2. Simulated Mach 6 wind tunnel run heat flux profile for a modeled chromel sensor with different model materials.

Figure 5-3 shows the progression of the high temperatures in the stainless steel hemisphere with the modeled chromel thermocouple as time goes from 0.5 s in the upper left, to 1.0 s in the upper right, to 1.5 s in the lower left, finally to 2.0 s and the end of the run in the lower right. The shaded colors are the temperatures of the solid as defined by the scale at the bottom of each plot, the temperatures of the fluid as defined by the scale at the top of each plot, and the contour lines are contours of Mach number as defined by the scale to the right of the plot. With the assumed "perfect" thermal contact between the sensor and the hemisphere and a modeled sensor that has similar thermal properties to the hemisphere, the temperature in the modeled sensor appears to match the hemisphere well at each time.

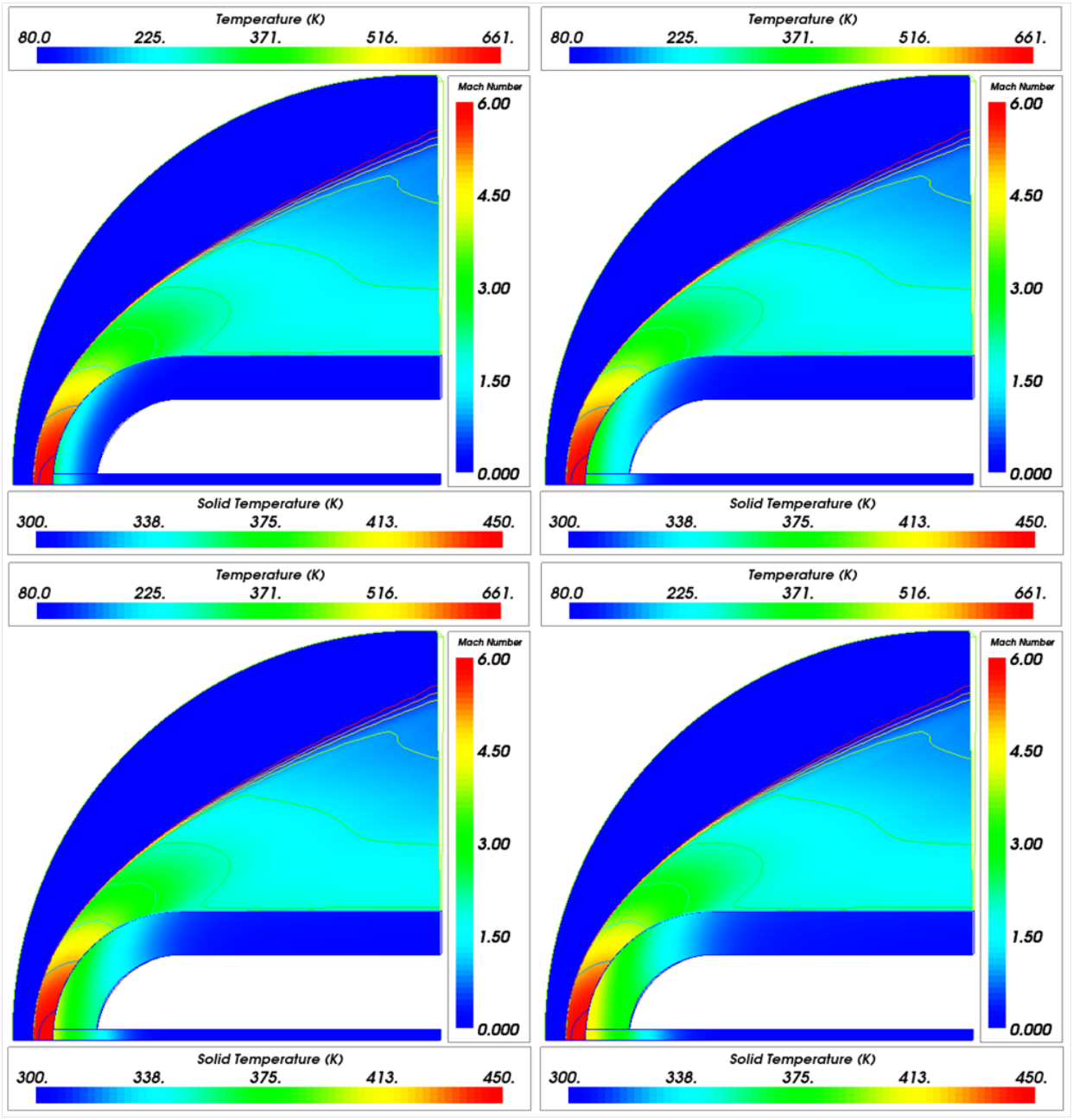

Figure 5-3. Temperature and Mach contours at t = 0.5, 1, 1.5, and 2 sec. for a Simulated Mach 6 wind tunnel run with a modeled chromel thermocouple in a stainless steel hemisphere.

Figure 5-4 shows the progression of the high temperatures in the MACOR® hemisphere with the modeled chromel thermocouple as time goes from 0.5 s to 2.0 s, as above. The temperature shading Mach contours and scales are the illustrated in Figure 5-3. While thermal contact is still assumed to be "perfect", the mismatch in the thermal properties

between the modeled chromel sensor and the MACOR® hemisphere means that the sensor is transferring the higher temperature deeper, and is cooler at the end of the run. Note that the maximum temperature of 532 K occurs away from the stagnation point on the surface of the hemisphere, and is hotter than any point in the stainless steel simulation.

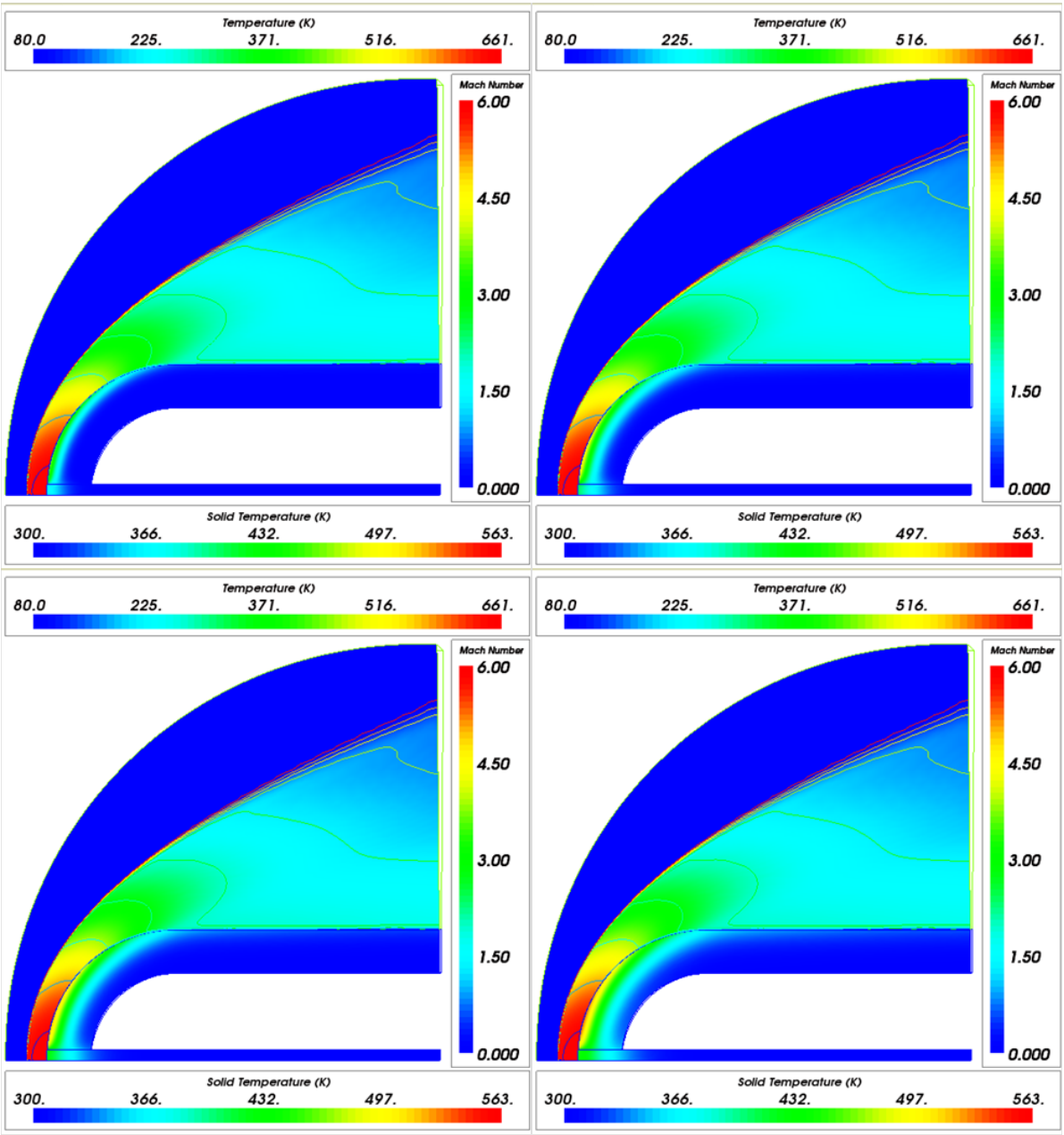

Figure 5-4. Temperature and Mach contours at t = 0.5, 1, 1.5, and 2 sec. for a Simulated Mach 6 wind tunnel run with a modeled chromel thermocouple in a MACOR® hemisphere.

Figure 5-5 shows the progression of the high temperatures in the Graphite hemisphere with the modeled chromel thermocouple as time goes from 0.5 s to 2.0 s, as above. Much like in the MACOR® model above, thermal contact is still assumed to be "perfect", but the mismatch in the thermal properties between the modeled chromel sensor and the Graphite hemisphere means that the hemisphere is transferring the higher temperature much deeper, and is cooler at the end of the run. Note that the maximum temperature of 392 K occurs at the stagnation point on the surface of the sensor, and is cooler than the hotspots in both the stainless steel MACOR® simulations.

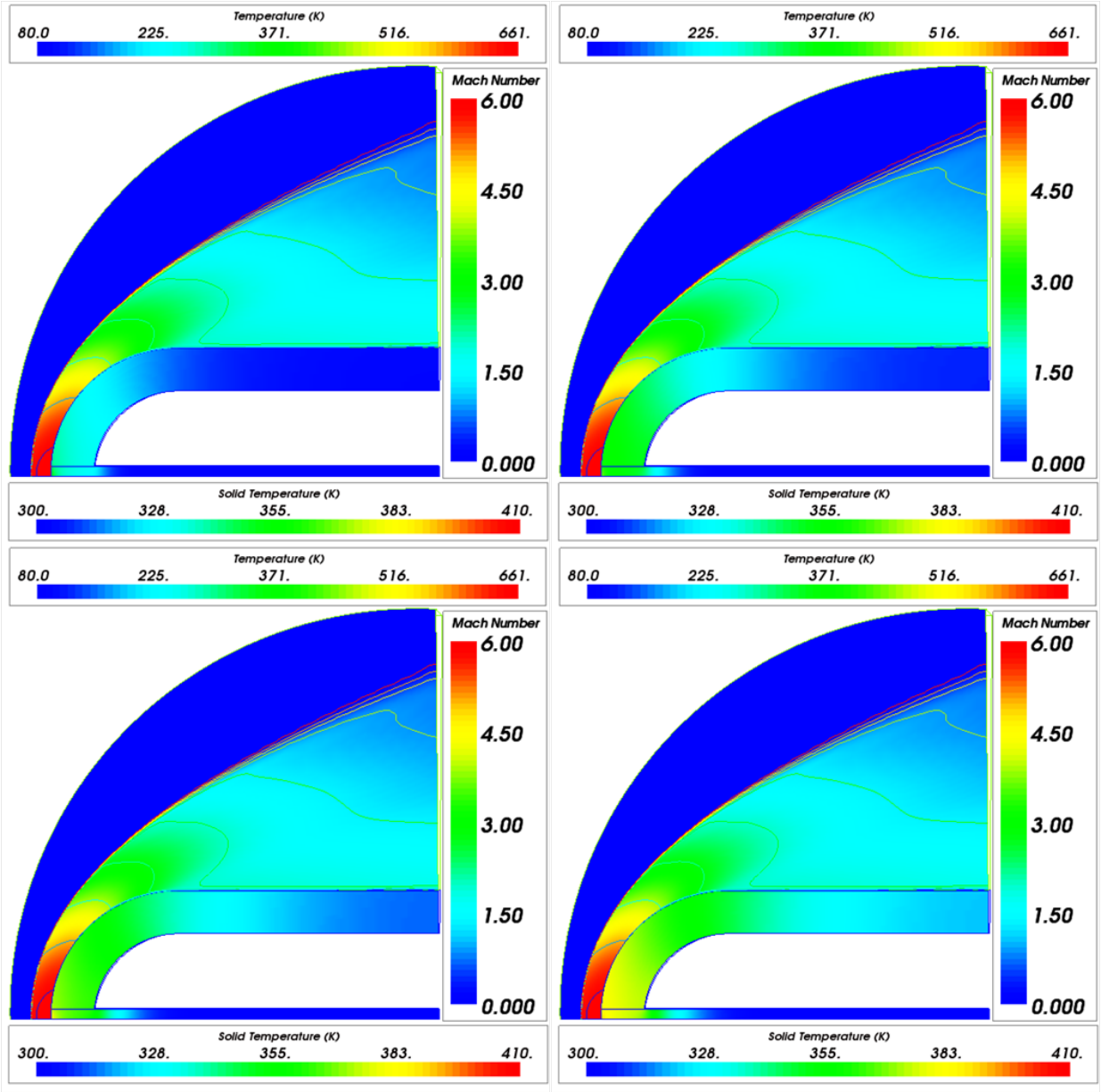

Figure 5-5. Temperature and Mach contours at t = 0.5, 1, 1.5, and 2 sec. for a Simulated Mach 6 wind tunnel run with a modeled chromel thermocouple in a Graphite hemisphere.

5.2 Fast Response Schmidt-Boelter Gage Surrogate

A surrogate of the 1/8 in. Schmidt-Boelter gage was simulated at the wind tunnel conditions in each of the hemisphere materials. Figure 5-6 shows the temperature results of the various simulated sensors at the test condition. As above, the stainless steel hemisphere data is blue, and MACOR is green, and the graphite is red. The surface

temperature is solid and the backface temperature is dashed. The temperature response at the backface is extremely fast, but it is interesting that the backface of the stainless steel hemisphere is hotter than the graphite hemisphere by 0.75 seconds. This means that the high thermal conductivity of the graphite is allowing a path for the thermal energy such that the back of the hemisphere does not get as hot. All of the backface temperatures are measured $^{1}/_{8}$ in. deep on the centerline of the modeled Schmidt-Boelter gage.

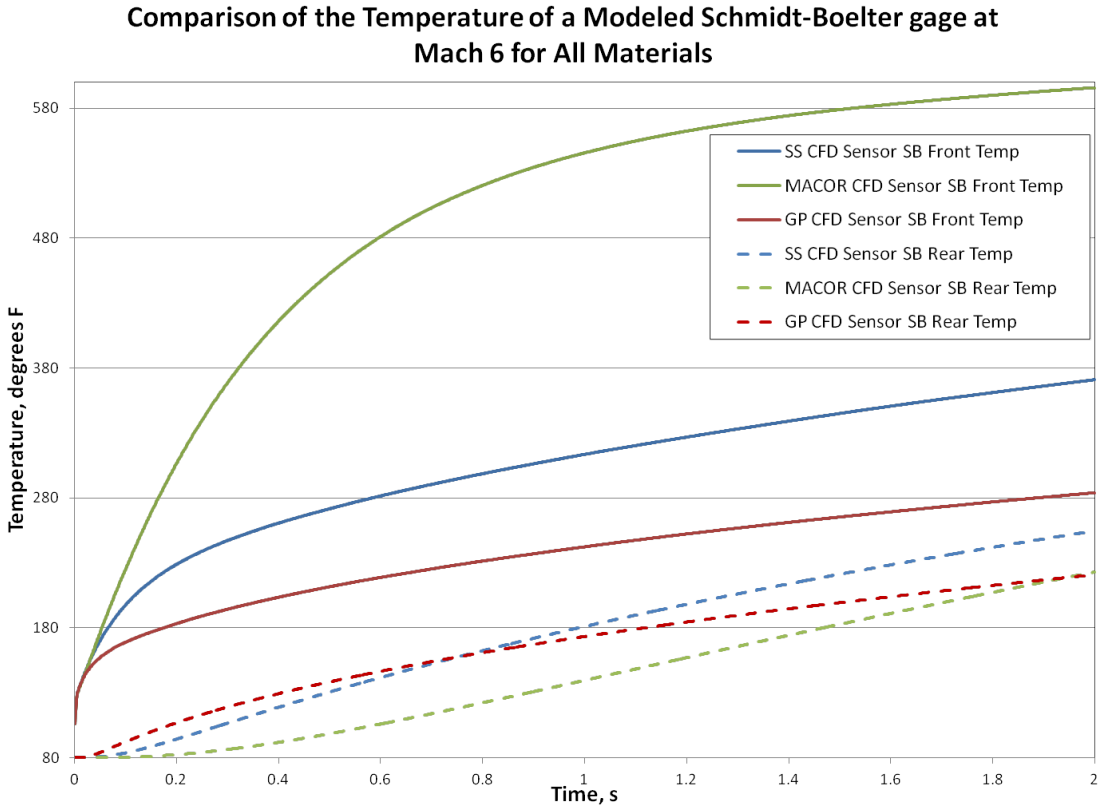

Figure 5-6. Simulated Mach 6 wind tunnel run temperature profile for a modeled Schmidt-Boelter gage with different model materials.

Figure 5-7 shows the heat flux output from GASP compared to the calculation of the heat flux "measured" by the modeled Schmidt-Boelter gages. As described in chapter 3, this measured heat flux was calculated using equations 1.6 and 1.12 from Chapter 1. The τ^* was assumed to be 0.015s which is on the order of the τ^*s for the actual Schmidt-Boelter gages used in this study. To calculate the heat flux using equation 1.6, the front temperature is an average of the temperature across the modeled wire and adhesive layer on the front of the sensor, taken from a line halfway between the stagnation point and the

next material. The rear temperature is similarly the average temperature across the rear wire and adhesive layer, halfway deep into the layer. The thickness is the distance between these two lines, and the thermal conductivity is the thermal conductivity of the wafer used in GASP. The modeled Schmidt-Boelter gages are all able to "measure" a heat flux that is within 2-4% of the heat flux that the simulation is applying, illustrating that a perfectly installed axi-symmetric Schmidt-Boelter is capable of correctly measuring heat flux in all three materials.

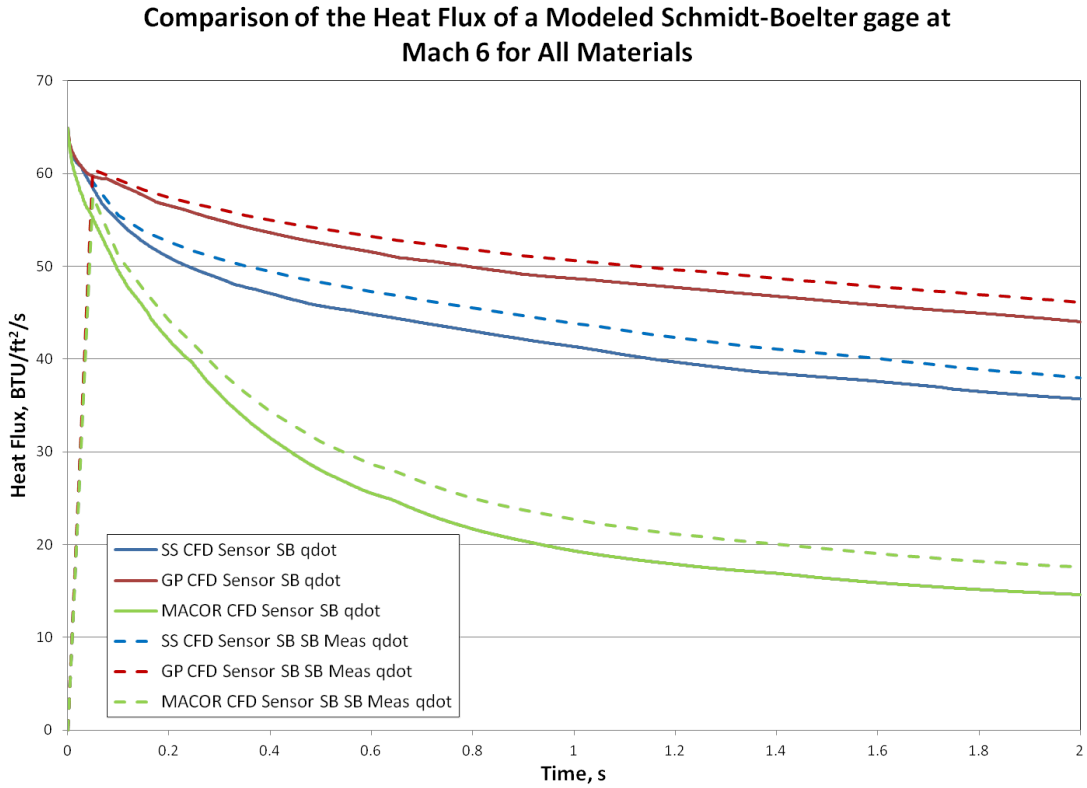

Figure 5-7. Simulated Mach 6 wind tunnel run heat flux profile for a modeled Schmidt-Boelter gage with different model materials.

Figure 5-8 shows the progression of the high temperatures in the stainless steel hemisphere with the modeled Schmidt-Boelter gage as time goes from 0.5 s in the upper left, to 1 s in the upper right, to 1.5 s in the lower left, finally to 2.0 s and the end of the run in the lower right. As discussed in the thermocouple section, the shaded colors are the temperatures of the solid as defined by the scale at the bottom of each plot, the

temperatures of the fluid as defined by the scale at the top of each plot, and the contour lines are contours of Mach number as defined by the scale to the right of the plot. The Schmidt-Boelter gage is designed to be mounted in stainless steel. But, the plots show that as time proceeds in the simulation, the surface of the sensor is much hotter than the metal around it, and the aluminum heat sink conducts faster such that the temperature gradient has penetrated deeper into the sensor at each time level.

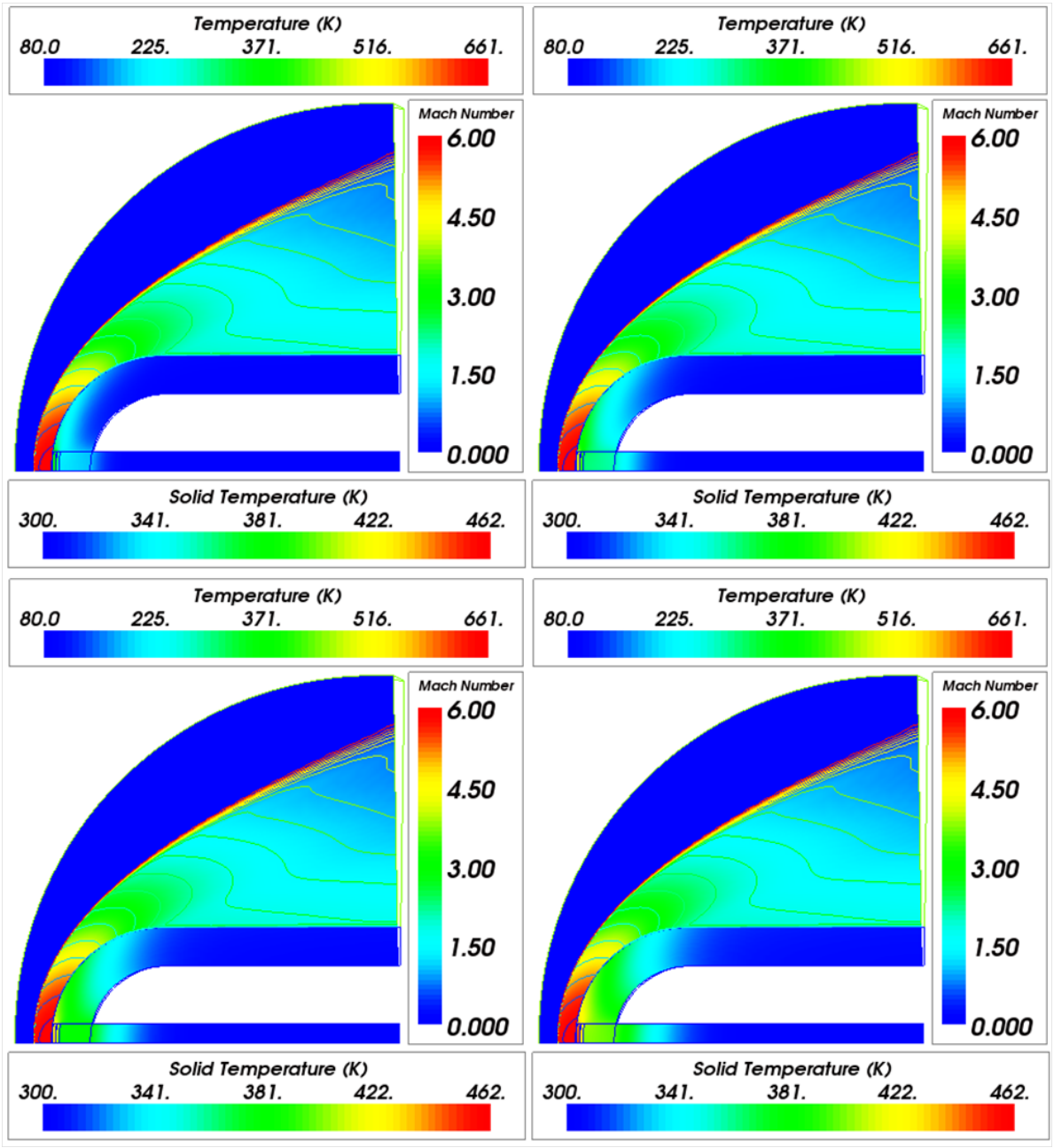

Figure 5-8. Temperature and Mach contours at t = 0.5, 1, 1.5, and 2 sec. for a Simulated Mach 6 wind tunnel run with a modeled Schmidt-Boelter gage in a stainless steel hemisphere.

Figure 5-9 shows the progression of the high temperatures in the MACOR® hemisphere with the modeled Schmidt-Boelter gage as time goes from 0.5 s to 2.0 s, as above. The temperature shading and Mach contours, and the scales are illustrated the same as in Figure 5-8. The mismatch in the thermal properties between the modeled Schmidt-

Boelter gage and the MACOR® hemisphere means that the sensor is transferring the higher gradient deeper, but interestingly the surface of the sensor is hotter than the hemisphere. This is different than the modeled thermocouple's trend in MACOR®. Note that the maximum temperature of 587 K occurs at the stagnation point on the surface of the sensor, and is well above the melting temperature of the adhesive for the Schmidt-Boelter gages of roughly 540 K. This confirms the behavior of the real Schmidt-Boelter mounted in MACOR® during a wind tunnel run.

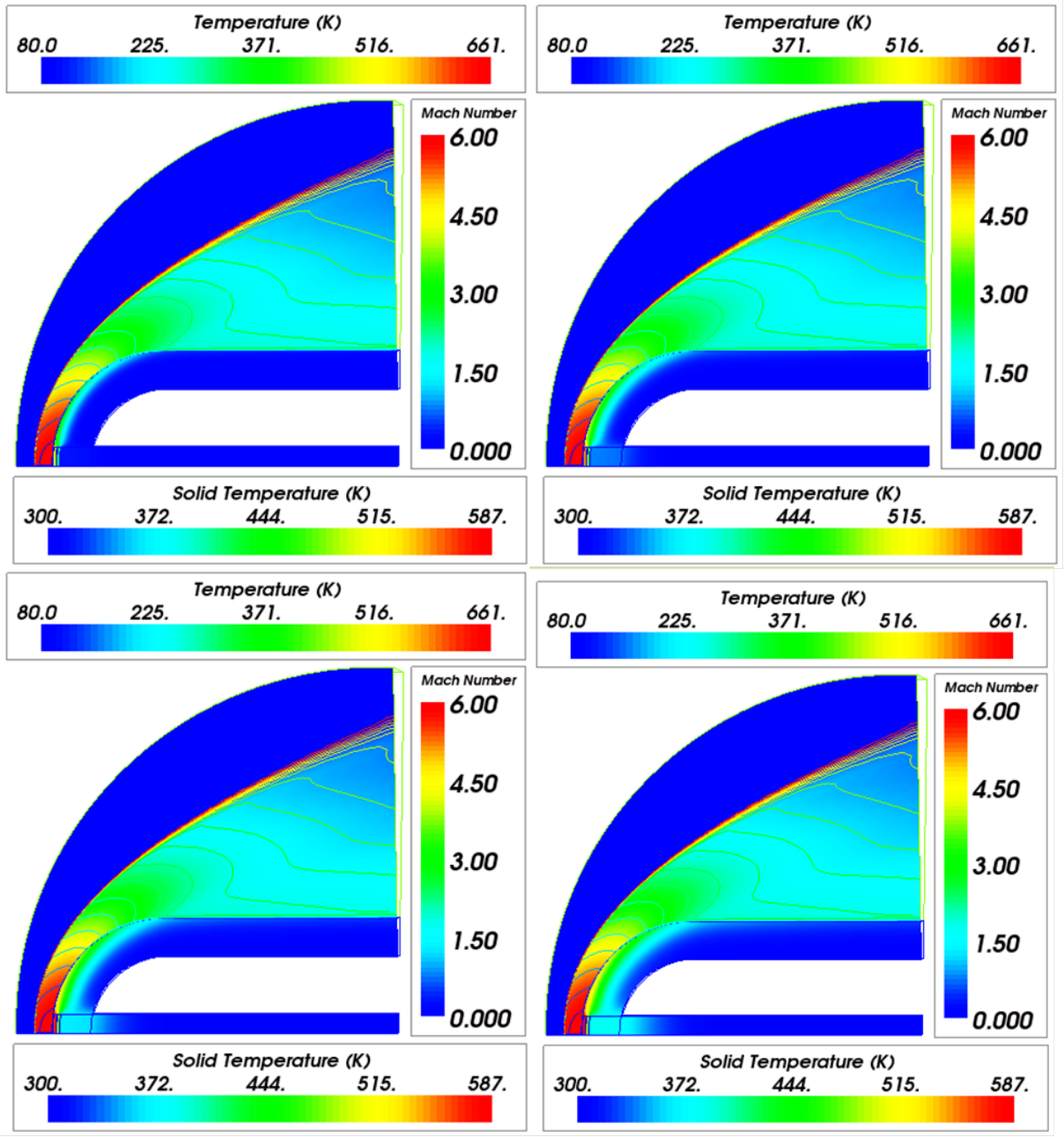

Figure 5-9. Temperature and Mach contours at t = 0.5, 1, 1.5, and 2 sec. for a Simulated Mach 6 wind tunnel run with a modeled Schmidt-Boelter gage in a MACOR® hemisphere.

Figure 5-10 shows the progression of the high temperatures in the Graphite hemisphere with the modeled Schmidt-Boelter gage as time goes from 0.5 s to 2.0 s, as above. The temperature shading and Mach contours, and the scales are illustrated the same as in Figure 5-8. Much like in the MACOR® model above, thermal contact is still assumed to

be “perfect”, but the mismatch in the thermal properties between the modeled Schmidt-Boelter gage and the Graphite hemisphere means that the hemisphere is transferring the higher temperature much deeper, and the surface of the hemisphere is cooler at the end of the run. Note that the maximum temperature of 414 K occurs at the stagnation point on the surface of the sensor, and is cooler than the hotspots in both the stainless steel MACOR® simulations.

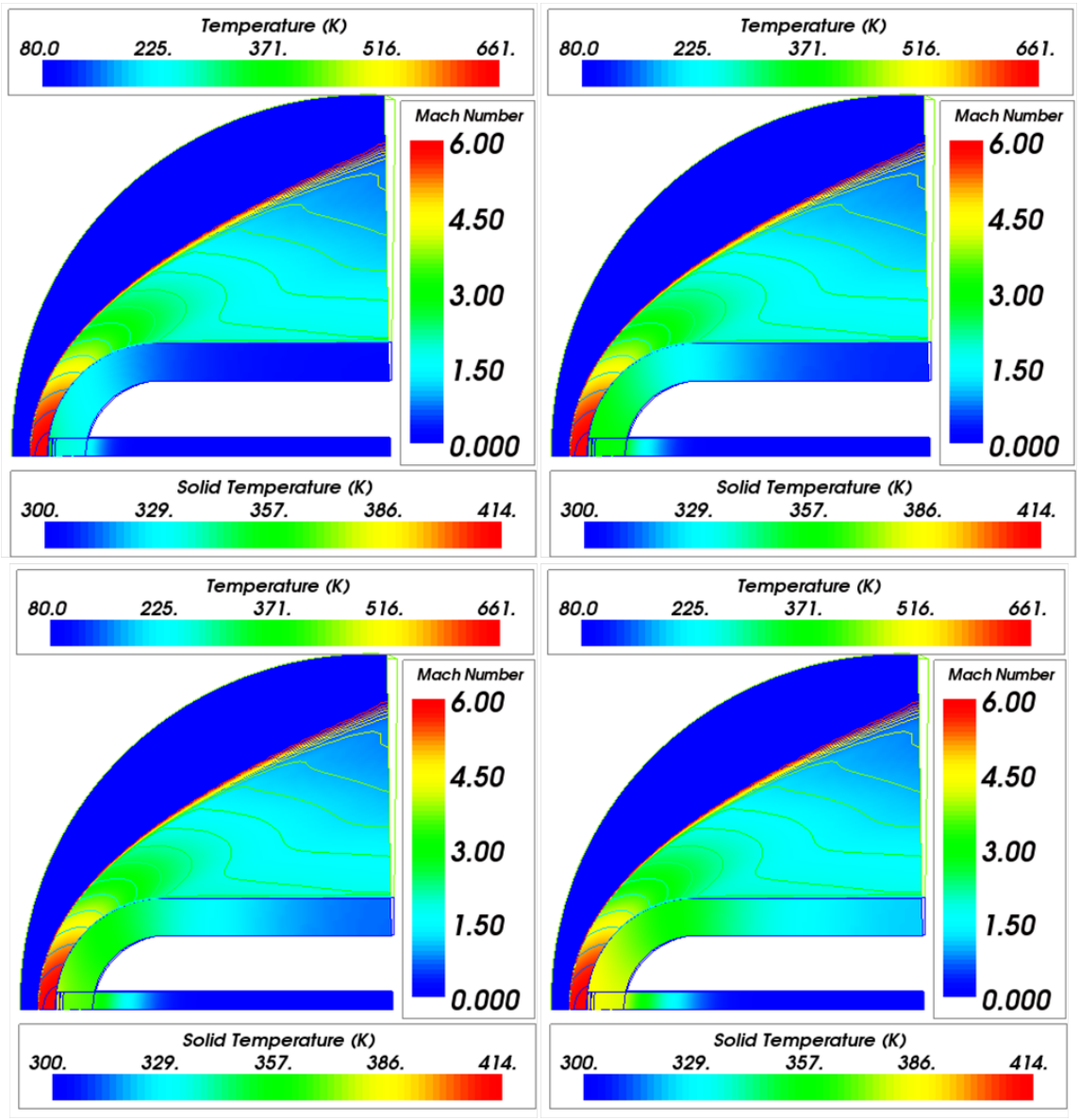

Figure 5-10. Temperature and Mach contours at t = 0.5, 1, 1.5, and 2 sec. for a Simulated Mach 6 wind tunnel run with a modeled Schmidt-Boelter gage in a Graphite hemisphere.

5.3 Fiber Optic Thermocouple Surrogate

Similar to the modeled thermocouple in the stainless steel hemisphere, a silica fiber used to simulate a fiber optic temperature sensor should mate well with the MACOR® hemisphere. Figure 5-11 and Figure 5-12 show the temperature and heat flux, respectively, of the various hemispheres with the simulated fiber. As above, the stainless steel hemisphere data is blue, and MACOR is green, and the graphite is red. In the temperature plot, the surface temperature is solid and the backface temperature is dashed. For the heat flux plot, the solid line is the GASP heat flux output and the dashed is the calculated heat flux. The heat flux calculated using a simple inverse method[9] does in fact yield good results in the MACOR® hemisphere. The low thermal conductivity of the silica fiber does extend the time that the semi-infinite assumption is valid for the inverse heat flux calculations in the MACOR® hemisphere, but the stainless steel and graphite hemispheres once again rise in temperature at the backface very early.

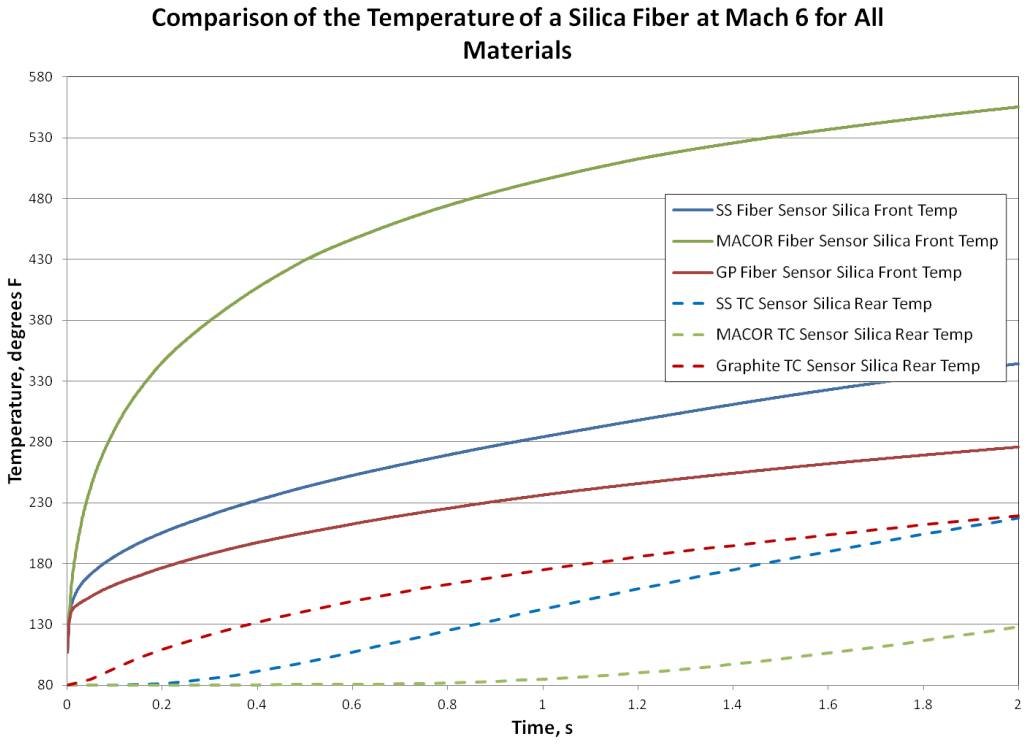

Figure 5-11. Simulated Mach 6 Wind Tunnel Run temperature profile for a silica fiber with different model materials.

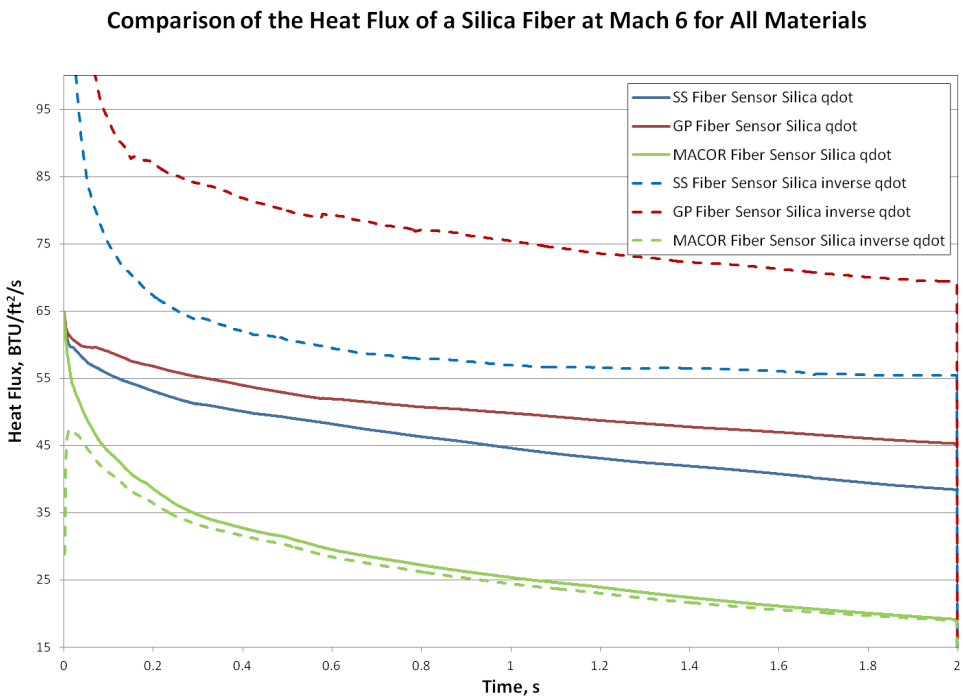

Figure 5-12. Simulated Mach 6 Wind Tunnel Run heat flux profile for a silica fiber with different model materials.

Figure 5-13 shows the progression of the high temperatures in the stainless steel hemisphere with the silica fiber as time goes from 0.5 s in the upper left, to 1.0 s in the upper right, to 1.5 s in the lower left, finally to 2.0 s and the end of the run in the lower right. The shaded colors are the temperatures of the solid as defined by the scale at the bottom of each plot, the temperatures of the fluid as defined by the scale at the top of each plot, and the contour lines are contours of Mach number as defined by the scale to the right of the plot. With the assumed "perfect" thermal contact between the sensor and the hemisphere and a modeled sensor that has very different thermal properties to the hemisphere, the temperature in the modeled sensor is hotter than the hemisphere at the surface, and the temperature gradient is deeper in the hemisphere.

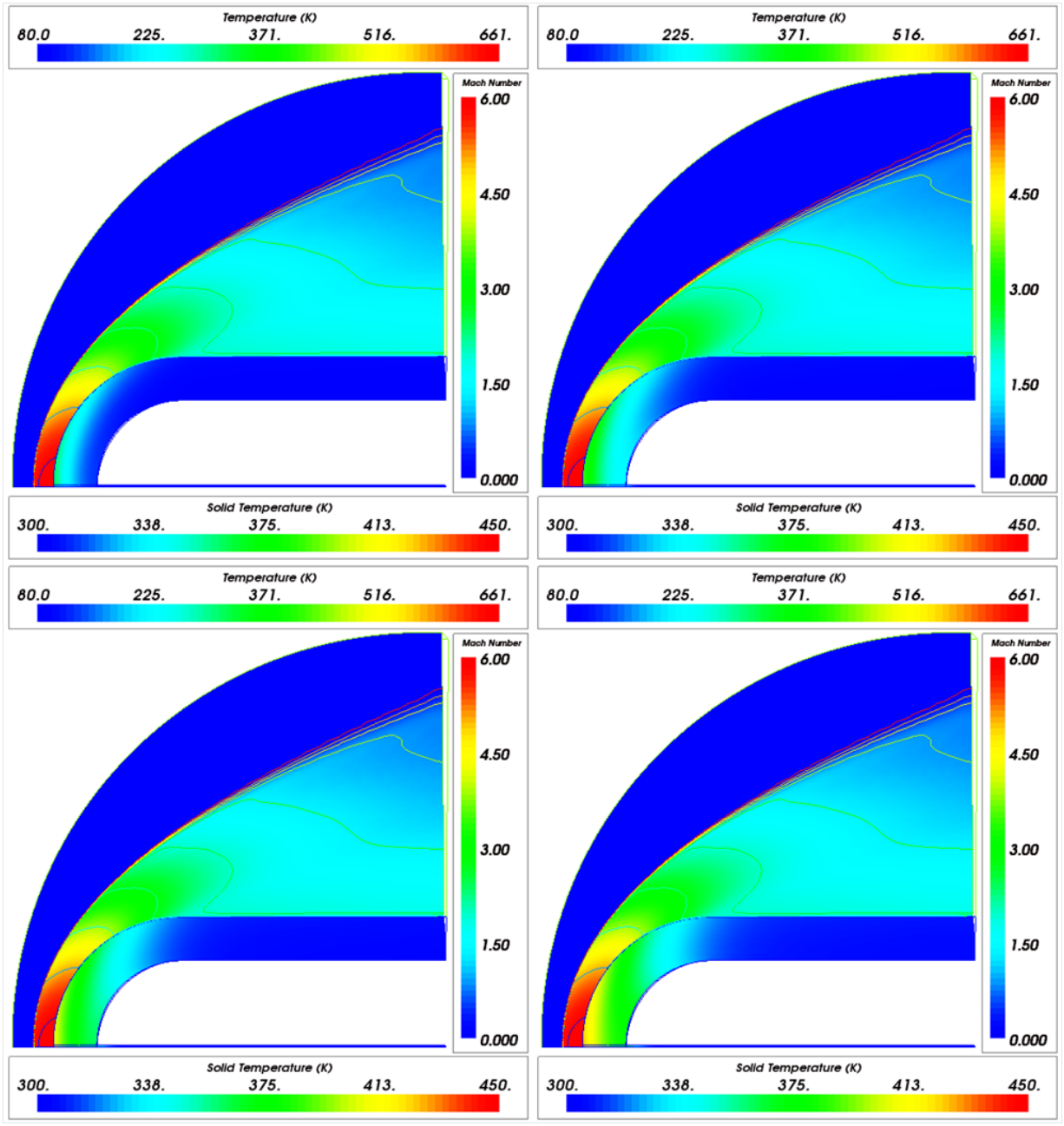

Figure 5-13. Temperature and Mach contours at t = 0.5, 1, 1.5, and 2 sec. for a Simulated Mach 6 wind tunnel run with a silica fiber in a stainless steel hemisphere.

Figure 5-14 shows the progression of the high temperatures in the MACOR® hemisphere with the silica fiber as time goes from 0.5 s to 2.0 s, as above. The temperature shading and Mach contours, and the scales are illustrated the same as in Figure 5-13. While thermal contact is still assumed to be "perfect", the matched thermal

properties between the silica fiber and the MACOR® hemisphere means that the sensor and hemisphere match in temperature very well. Note that the maximum temperature of 559 K occurs at the stagnation point on the surface of the fiber as it should for a matched model.

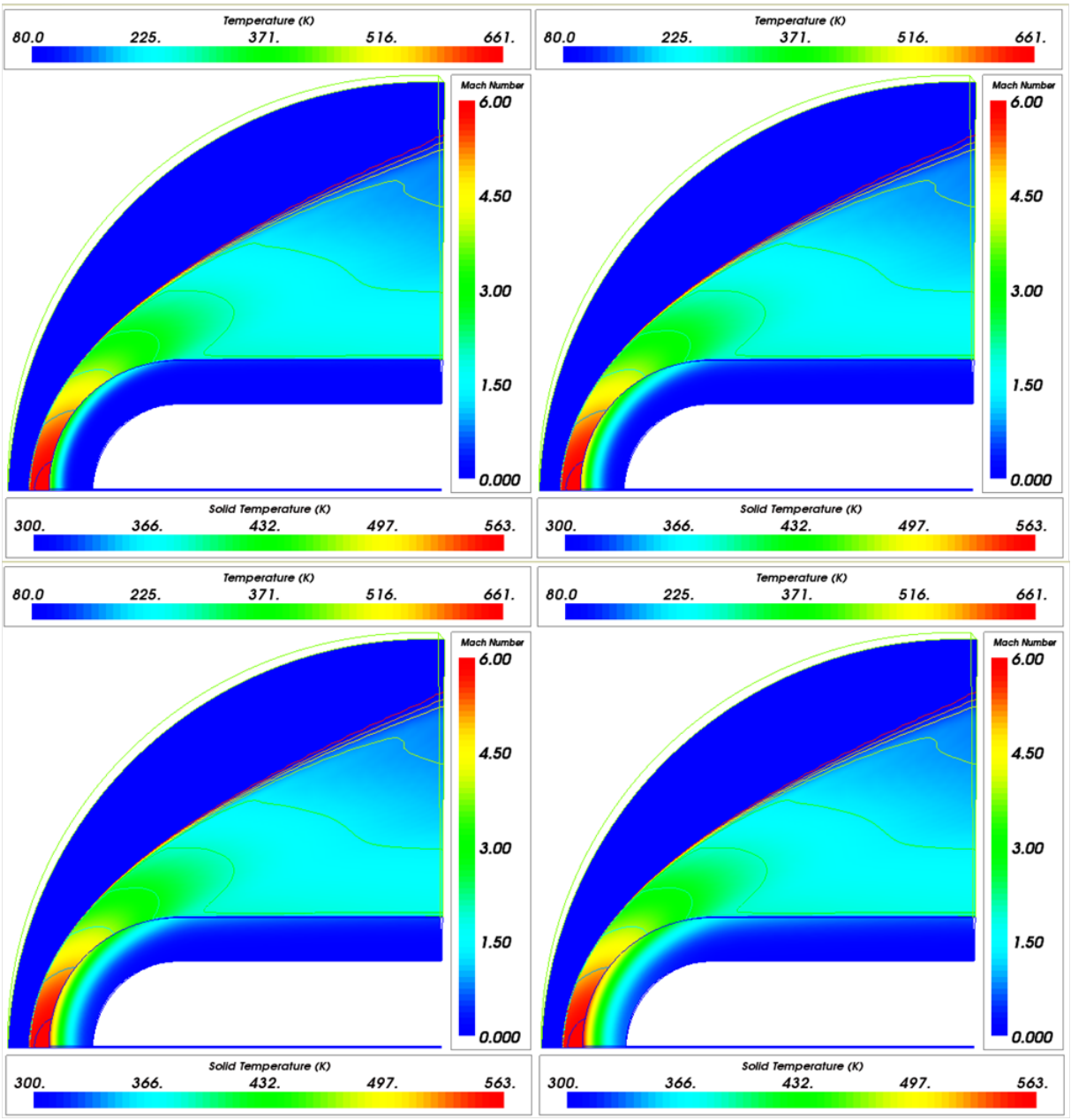

Figure 5-14. Temperature and Mach contours at t = 0.5, 1, 1.5, and 2 sec. for a Simulated Mach 6 wind tunnel run with a silica fiber in a MACOR® hemisphere.

Figure 5-15 shows the progression of the high temperatures in the Graphite hemisphere with the silica as time goes from 0.5 s to 2.0 s, as above. The temperature shading and Mach contours, and the scales are illustrated the same as in Figure 5-13. Much like in the MACOR® model above, thermal contact is still assumed to be "perfect", but the mismatch in the thermal properties between the silica fiber and the Graphite hemisphere means that the hemisphere is transferring the higher temperature much deeper, and is cooler at the end of the run. Note that the maximum temperature of 410 K occurs at the stagnation point on the surface of the sensor, and is cooler than the hotspots in both the stainless steel MACOR® simulations.

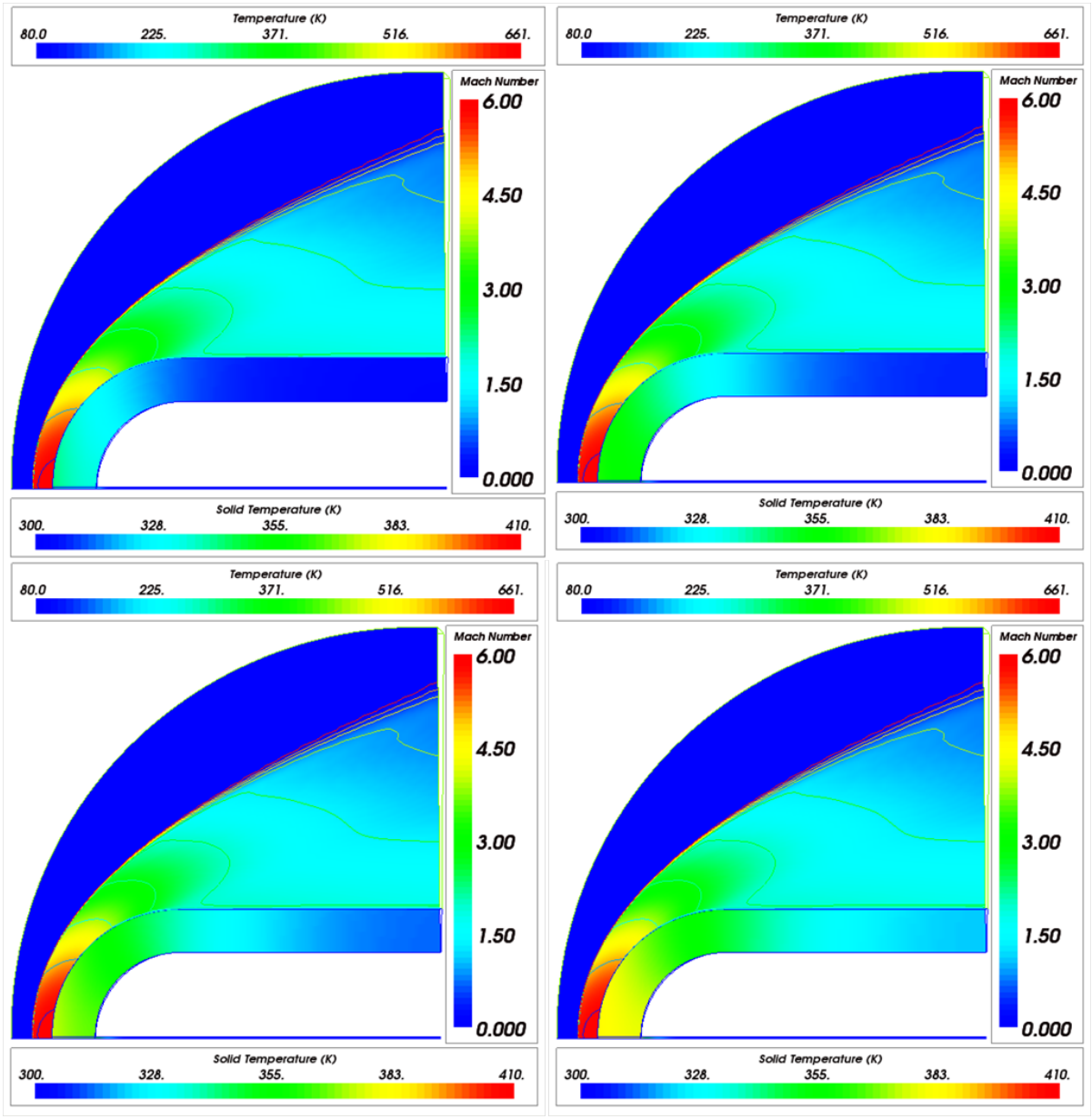

Figure 5-15. Temperature and Mach contours at t = 0.5, 1, 1.5, and 2 sec. for a Simulated Mach 6 wind tunnel run with a silica fiber in a Graphite hemisphere.

5.4 Perfect Sensor

In order to simulate the "perfect" sensor installed in each of the hemispheres, a $^{1}/_{16}$ in. diameter column of the same material as the hemisphere was simulated to try and ascertain the ideal performance of an indirect sensor. Figure 5-16 shows the temperature results of the various simulated sensors at the test condition. As above, the stainless steel

hemisphere data is blue, and MACOR is green, and the graphite is red. The surface temperature is solid and the backface temperature is dashed. As in the above sensor/hemisphere combinations, the $^1/_8$ in. thick hemisphere causes the back surface temperatures to rise very quickly. The temperature on the backface of the Graphite hemisphere is rising after 0.02 s, the stainless steel backface temperature rises after 0.2 s, and the MACOR® hemisphere's backface rises after 0.82 s. All of these temperatures are measured $^1/_8$ in. deep on the centerline of the modeled perfect sensor.

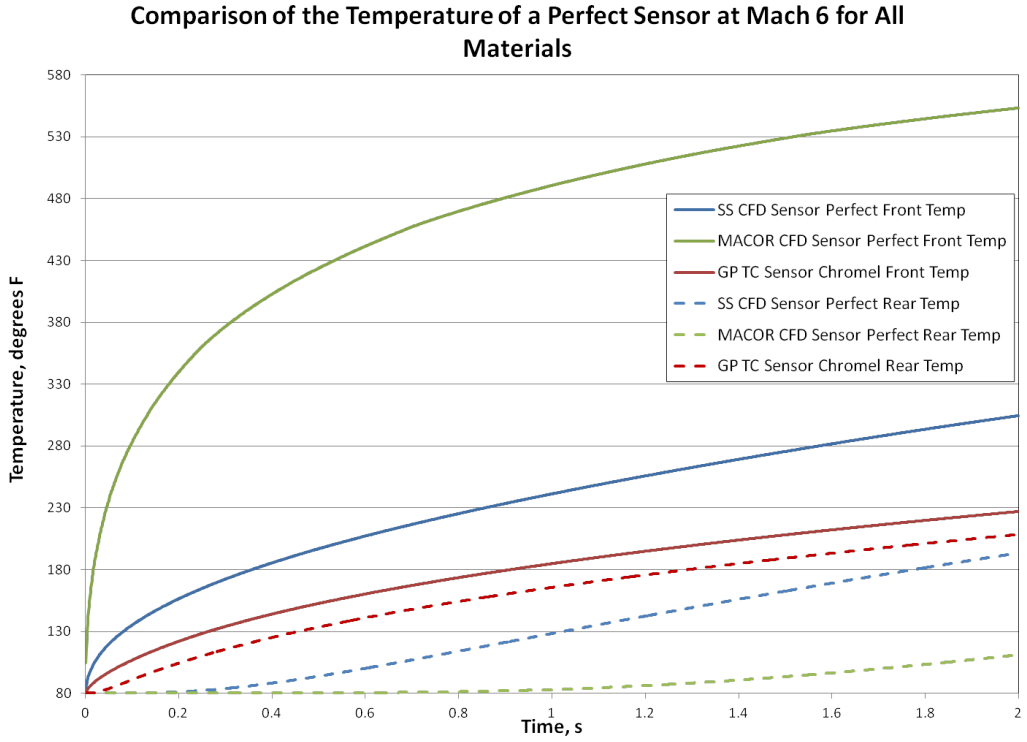

Figure 5-16. Simulated Mach 6 Wind Tunnel Run temperature profile for a perfect sensor with different model materials.

Figure 5-17 shows the heat flux output from GASP compared to the inverse method[9] calculation for each of the perfect sensors. The solid line is the GASP heat flux output and the dashed is the calculated heat flux. The MACOR® sensor inverse calculation is very close to the modeled heat flux, but the other inverse heat flux calculations are unable to recover simulated heat flux due to the failure of the semi-infinite assumption.

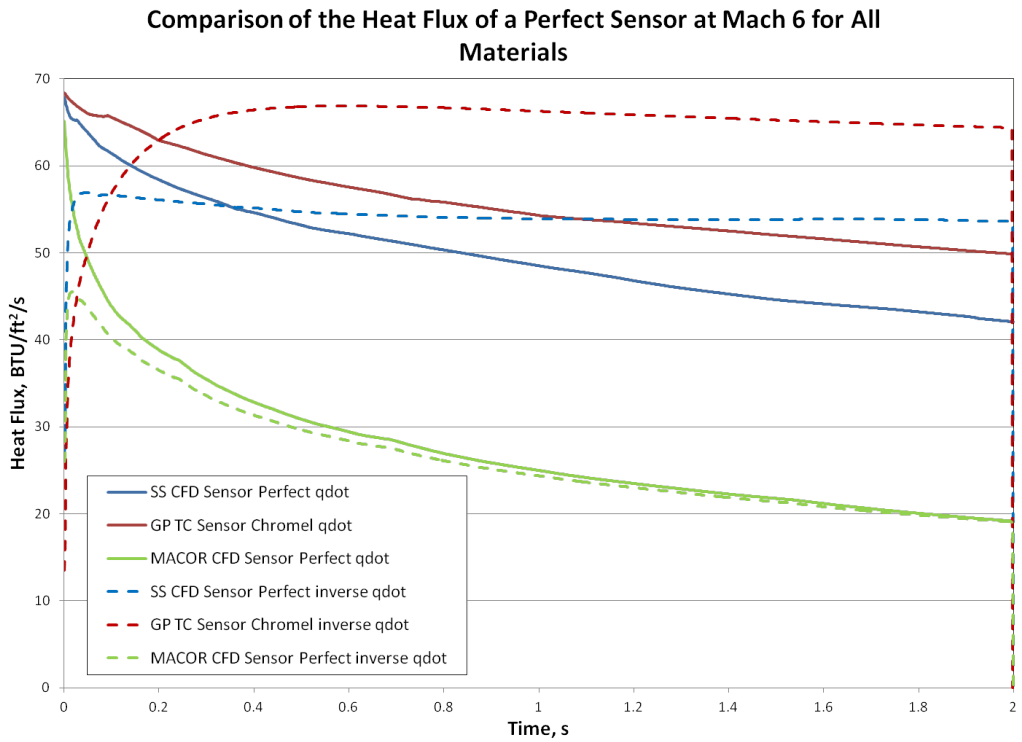

Figure 5-17. Simulated Mach 6 Wind Tunnel Run heat flux profile for a perfect sensor with different model materials.

Figure 5-18 shows the progression of the high temperatures in the stainless steel hemisphere with the perfect stainless steel sensor as time goes from 0.5 s in the upper left, to 1.0 s in the upper right, to 1.5 s in the lower left, finally to 2 s and the end of the run in the lower right. The shaded colors are the temperatures of the solid as defined by the scale at the bottom of each plot, the temperatures of the fluid as defined by the scale at the top of each plot, and the contour lines are contours of Mach number as defined by the scale to the right of the plot. With the assumed "perfect" thermal contact between the sensor and the hemisphere and a modeled sensor that has identical thermal properties to the hemisphere, the temperature in the modeled sensor is an extension of the hemisphere.

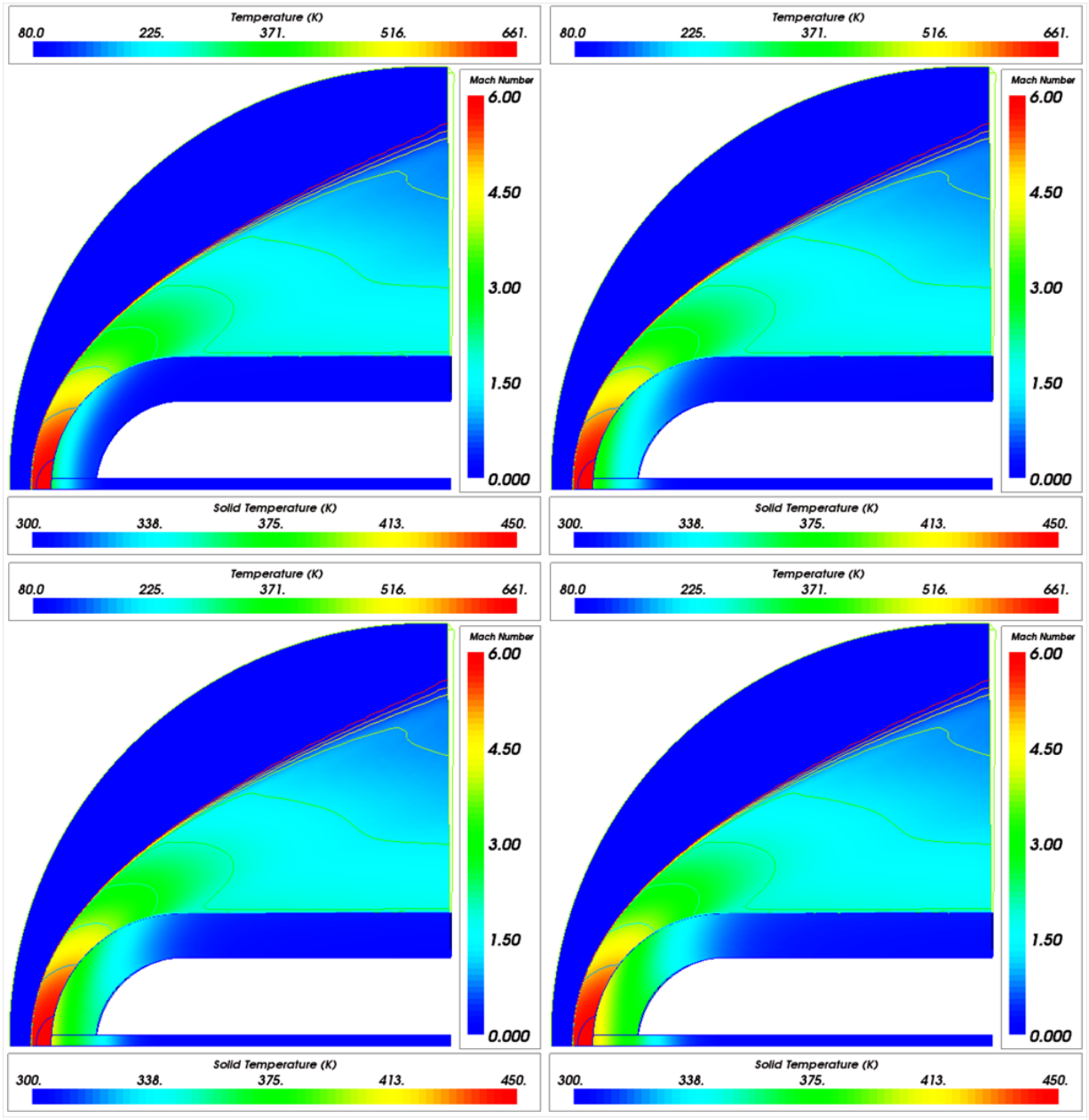

Figure 5-18. Temperature and Mach contours at t = 0.5, 1, 1.5, and 2 sec. for a Simulated Mach 6 wind tunnel run with a stainless steel sensor in a stainless steel hemisphere.

Figure 5-19 shows the progression of the high temperatures in the MACOR® hemisphere with the MACOR® perfect sensor as time goes from 0.5 s to 2 s, as above. The temperature shading and Mach contours, and the scales are illustrated the same as in Figure 5-18. Much like in Figure 5-18, the assumed "perfect" thermal contact between the sensor and the hemisphere and a modeled sensor that has identical thermal properties

to the hemisphere means that the temperature in the modeled sensor is an extension of the hemisphere. Note that the maximum temperature of 563 K occurs at the stagnation point on the surface of the fiber as it should for a matched model.

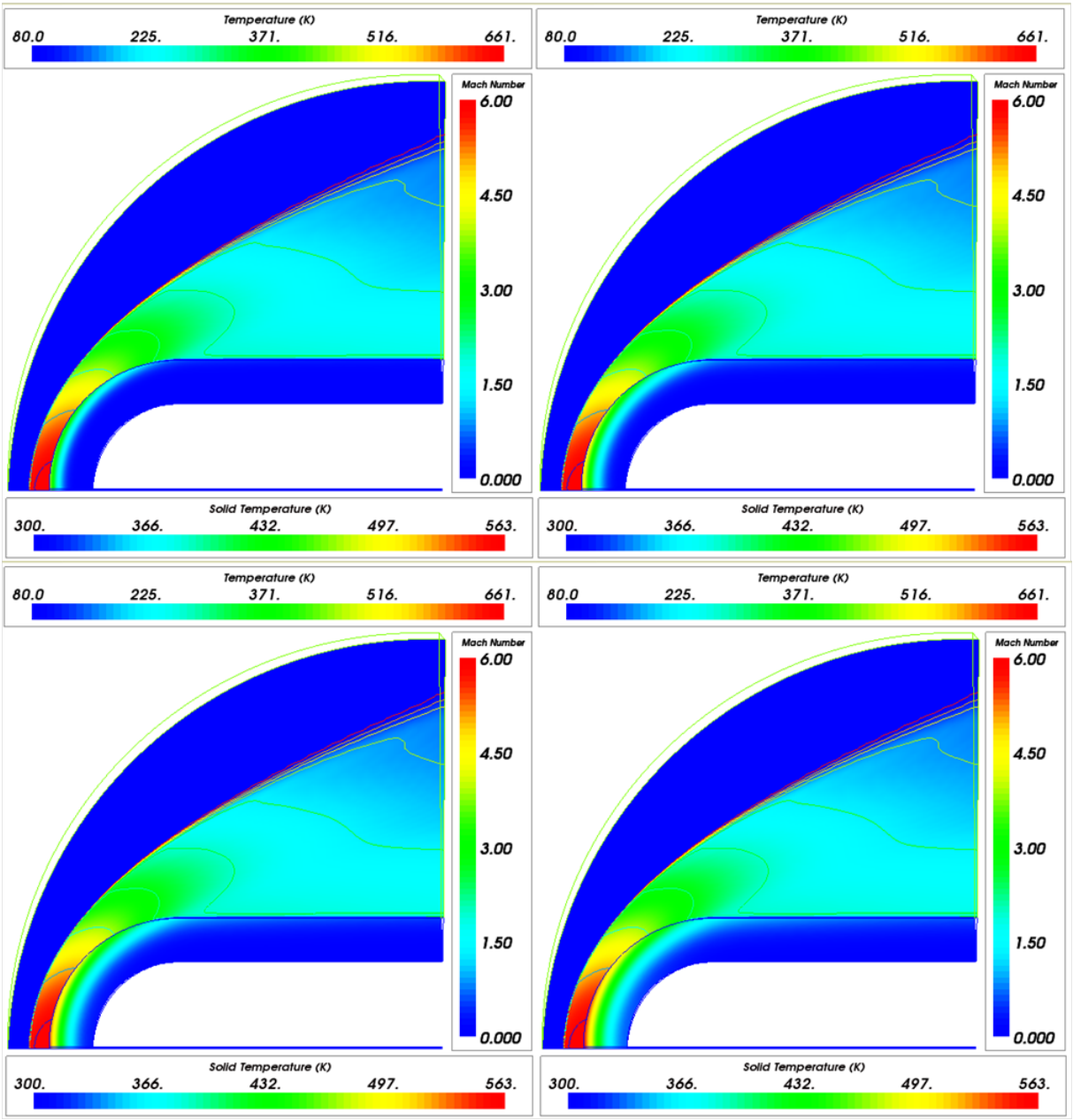

Figure 5-19. Temperature and Mach contours at t = 0.5, 1, 1.5, and 2 sec. for a Simulated Mach 6 wind tunnel run with a MACOR® sensor in a MACOR® hemisphere.

Figure 5-20 shows the progression of the high temperatures in the Graphite hemisphere with the perfect Graphite sensor as time goes from 0.5 s to 2 s, as above. The

temperature shading and Mach contours, and the scales are illustrated the same as in Figure 5-18. Again, the assumed perfect thermal contact and perfect thermal property match mean that the sensor is an extension of the hemisphere. Note that the maximum temperature of 383 K occurs at the stagnation point on the surface of the fiber as it should for a matched model, and is cooler than the other two materials.

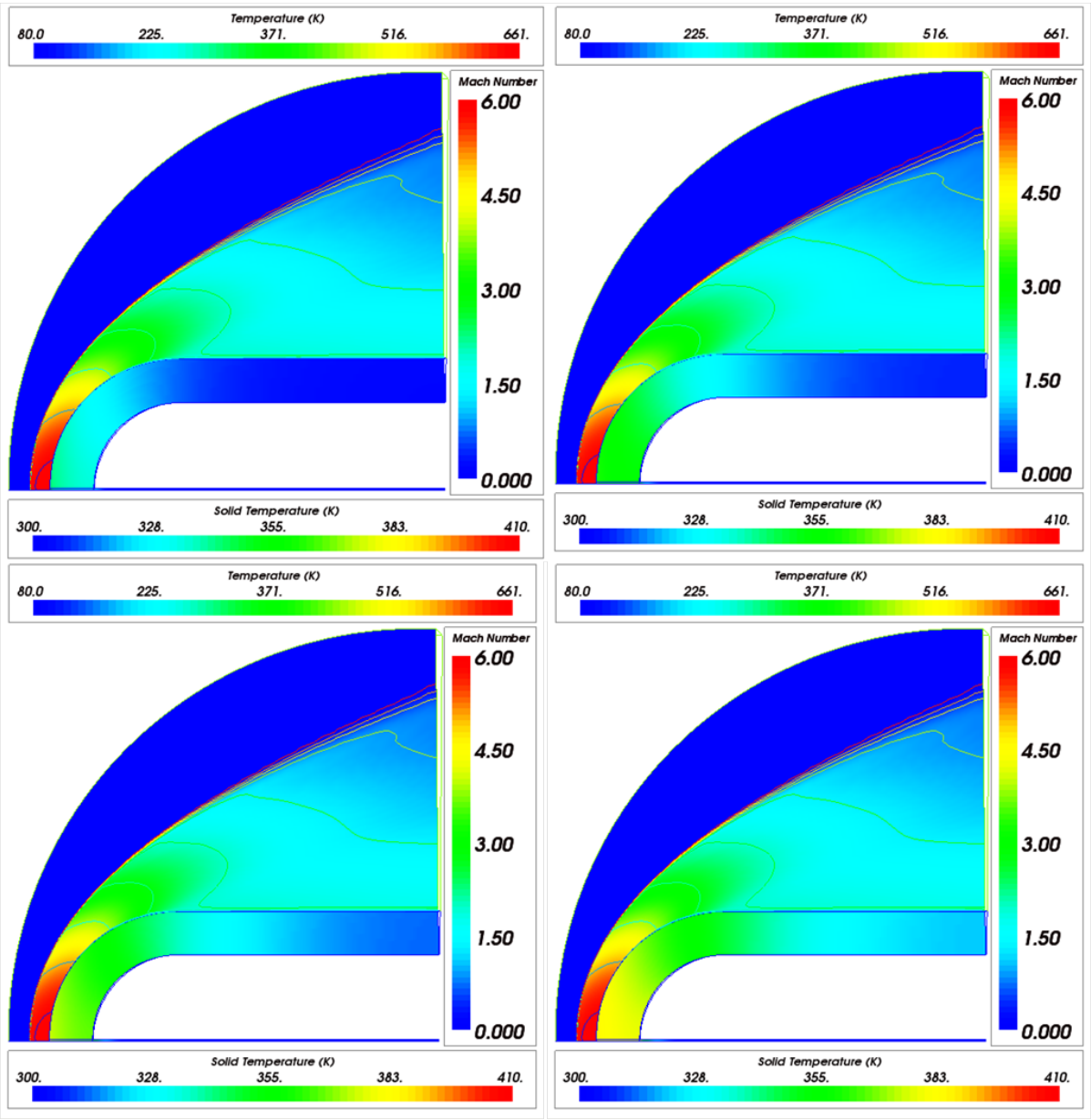

Figure 5-20. Temperature and Mach contours at t = 0.5, 1, 1.5, and 2 sec. for a Simulated Mach 6 wind tunnel run with a Graphite sensor in a Graphite hemisphere.

6. Experimental and Computational Results Comparison

The results from chapter 4, Experimental Results, and chapter 5, Computational Results, are compared in this section. The conditions for the VTHST and CFD with CHT remain the same as described in chapters 2 and 3, respectively.

As a reminder, the CFD simulations involve three major assumptions. First, the violent transients during the VTHST start-up are ignored, and the time accurate portion starts on-condition. This means that the solid is unaffected by "start-up". This assumption has to be made as a time accurate wind tunnel simulation including start-up is very complex and would involve a full tunnel, 3-D, time-accurate simulation. Second, the complex internal geometry of the hemisphere is neglected, along with the more intricate geometry of the coaxial thermocouple, Schmidt-Boelter gage, and fiber. Again, the main purpose of this assumption is to reduce grid size and complexity and because the contact thermal resistance difference between simulation and test is already a larger concern. Lastly, the thermal contact between the various materials is assumed perfect. The normal contact resistance that occurs between two materials is neglected as if the various materials were bonded at a molecular level.

For comparison, t = 0 s remains the start time for the tunnel, and the beginning of the unsteady CHT portion of the CFD simulations. Because of this, the simulations only overlay 1.1 s of the "on-condition" run. This does allow the CFD solution to somewhat "catch up" to the wind tunnel run because the simulations neglect start-up of the tunnel.

The temperature and heat flux plots of the VTHST in the following sections comparing sensors in a single material follow the following patterns. The data from the both the real and modeled coaxial thermocouples is red and from the real and modeled Schmidt-

Boelter gages is black. The modeled fiber optic thermocouple is blue, and the perfect sensor and the quasi-steady Fay-Riddell are green. All VTHST sensors or calculations are solid lines and the modeled sensors are dashed lines. On the temperature graphs, only the stagnation temperatures are compared as the modeled sensors have a rear location at 1/8 in. instead of the 0.3 in. of the real hemisphere models. In each heat flux plot, the simulation data is the GASP output of heat flux at the stagnation point, except for the modeled Schmidt-Boelter gage. In that case, the heat flux is the simulation of the "measured" heat flux as discussed in chapters 3 and 5.

6.1 Stainless Steel Hemisphere Comparison

Figure 6-1 is the temperature plot of all the real and modeled sensors in their stainless steel hemispheres. Because the simulations do not account for the wind tunnel start-up, the modeled sensors do not capture the rapid initial rise. But, the real and modeled sensors have very similar slopes once the tunnel is "on-condition." Moreover, the trend that the front of the Schmidt-Boelter gage, in black, is hotter than the coaxial thermocouple is duplicated in the simulations. This plot also shows that with perfect thermal contact, the coaxial thermocouple should follow the stagnation point temperature rise of a stainless steel hemisphere with no sensor at all within 2-3%.

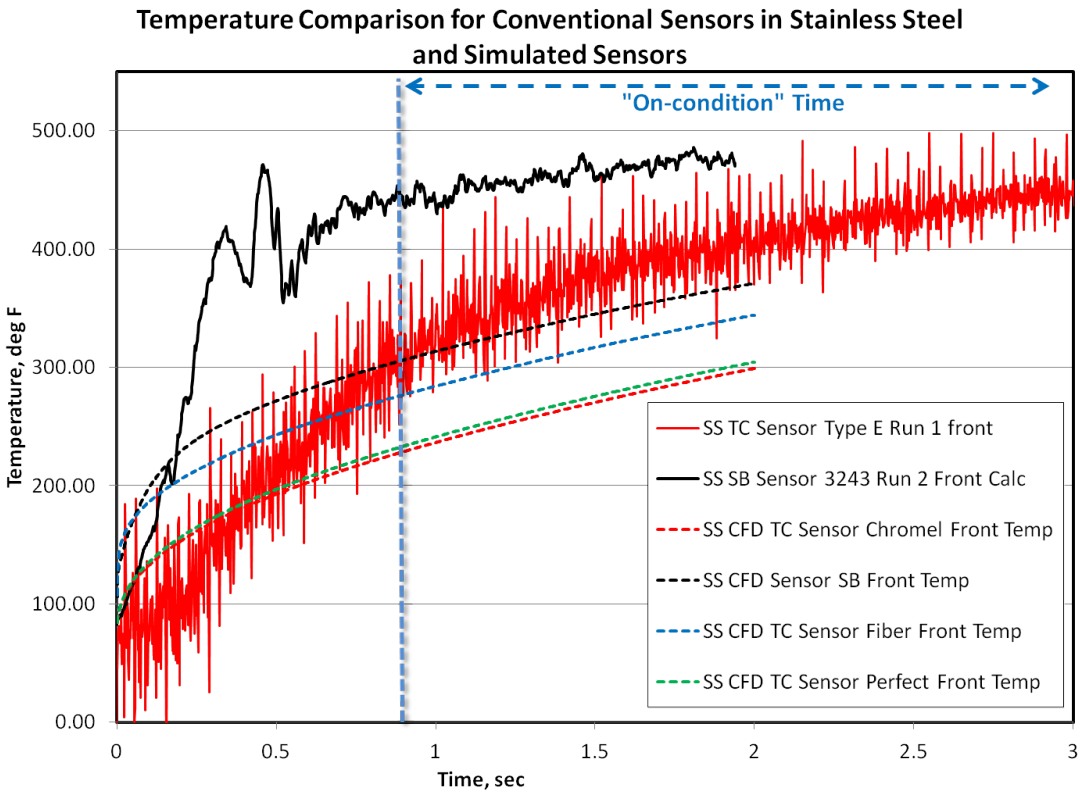

Figure 6-1. Stainless steel model temperature comparison VTHST to CFD with CHT.

Figure 6-2 is the heat flux plot of all the real and modeled sensors in their stainless steel hemispheres. Even though the simulations do not account for the wind tunnel start-up, the measured heat flux from the Schmidt-Boelter gage is well within the 13.18% uncertainty of the heat flux measurements when compared to the modeled perfect stainless steel hemisphere. Also, the modeled Schmidt-Boelter gage's "measured" heat flux is within 5-6% of the GASP output for the stainless steel hemisphere. Nothing about the simulations is able to explain the extremely high calculated inverse heat flux using the measured temperature from the coaxial thermocouple. The divergence in the slope of the real Schmidt-Boelter gage compared to the modeled gage is most likely a result of the higher temperature at the face of the real gage during the run due to start-up transients.

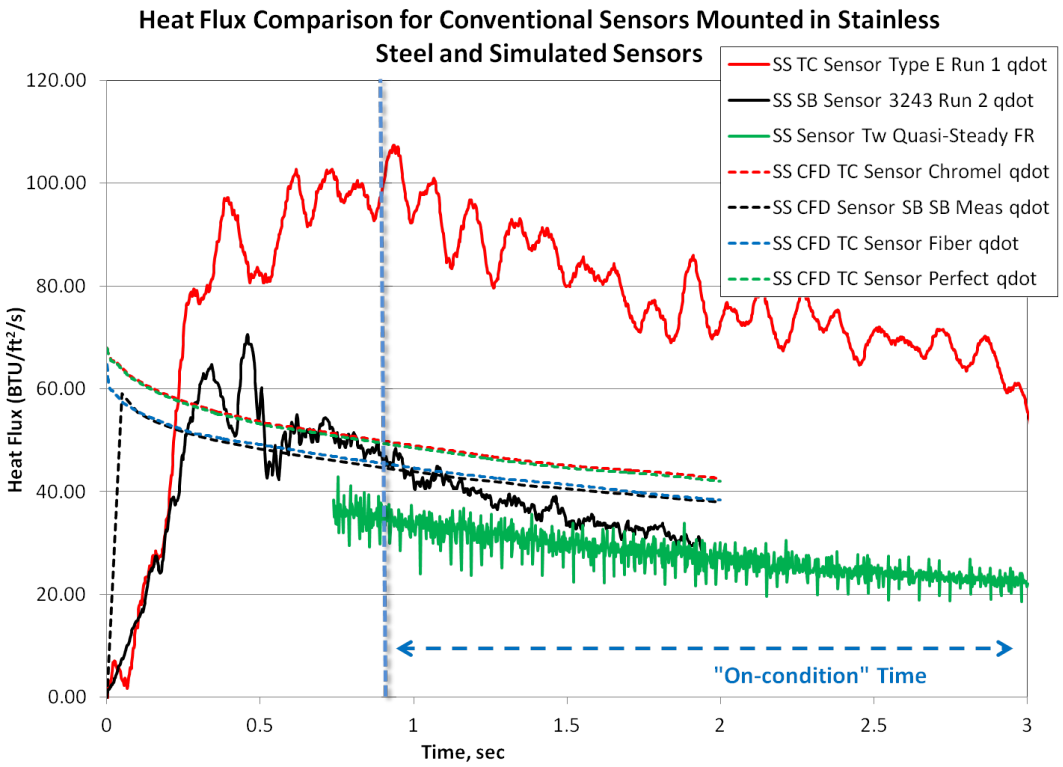

Figure 6-2. Stainless steel model heat flux comparison VTHST to CFD with CHT.

The comparison of the simulated stainless steel hemisphere to the real VTHST runs of a stainless steel hemisphere offer insight into the apparent problems that existed in the coaxial thermocouple in the stainless steel hemisphere. In the simulations, even with the assumptions and differences, the modeled thermocouple still matched the temperature and heat flux of the modeled stainless steel hemisphere, as expected. But, as shown in chapter 5, an inverse heat flux calculation using the temperature from the modeled coaxial thermocouple does not recover the actual heat flux because the one-dimensional and semi-infinite assumptions for the inverse heat flux calculations do not hold for the simulated wind tunnel runs.

6.2 MACOR® Hemisphere Comparison

Figure 6-3 is the temperature plot of all the real and modeled sensors in their MACOR® hemispheres. Interestingly, the modeled Schmidt-Boelter gage in dashed black almost

matches the real Schmidt-Boelter gage in solid black initially. Because the front temperature is calculated on the real Schmidt-Boelter gage, it is entirely possible that going over the melting temperature of the adhesive changed the thickness enough that the front temperature equation was no longer valid. In fact, the surface of the real Schmidt-Boelter gage might have reached above 600° F as the simulation predicts. This plot also illustrates why a fiber optic sensor would accurately measure temperature in MACOR® if it was properly installed as the modeled fiber optic temperature sensor matches the temperature rise of the perfect MACOR temperature sensor within 1-2% throughout the simulation. As expected, neither version of the coaxial thermocouple accurately measures the stagnation temperature, and the mismatch in magnitude and slope of the real coaxial thermocouple in solid red, compared to the modeled thermocouple in dashed red, depicts that the real sensor does not have perfect thermal contact.

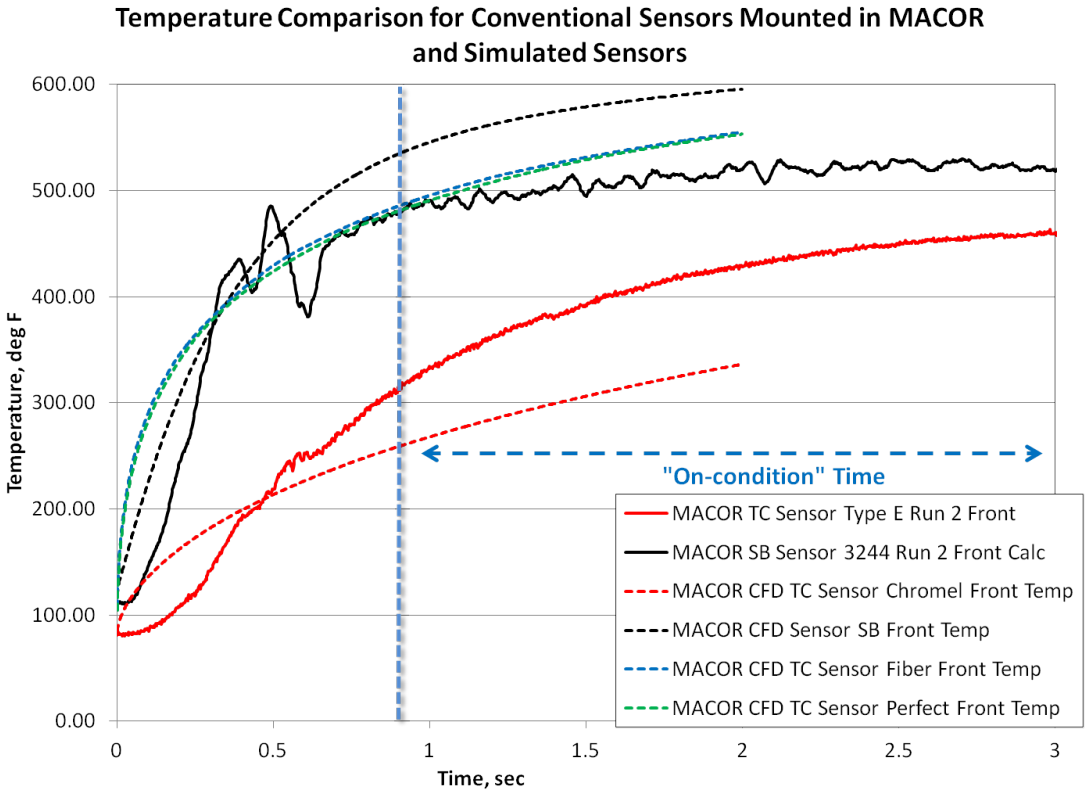

Figure 6-3. MACOR® model temperature comparison VTHST to CFD with CHT.

Figure 6-4 is the heat flux plot of all the real and modeled sensors in their MACOR® hemispheres. Of note is that again, even though the simulations do not account for the wind tunnel start-up, the "measured" heat flux from the modeled Schmidt-Boelter gage is well within the 13.18% uncertainty of the heat flux measurements when compared to the modeled perfect MACOR® hemisphere. This plot also appears to show the inverse heat flux calculation of the coaxial thermocouple as accurate when compared to the simulation output of the MACOR sensor. The problem is that this is an artifact of the inverse heat flux calculation, and not necessarily the right result. It is possible that at a different tunnel condition the inverse heat flux would be completely wrong. Note that instead of the GASP output heat flux for the modeled fiber optic sensor, the blue dashed line is the inverse heat flux calculation using the temperature data from the modeled fiber optic sensor.

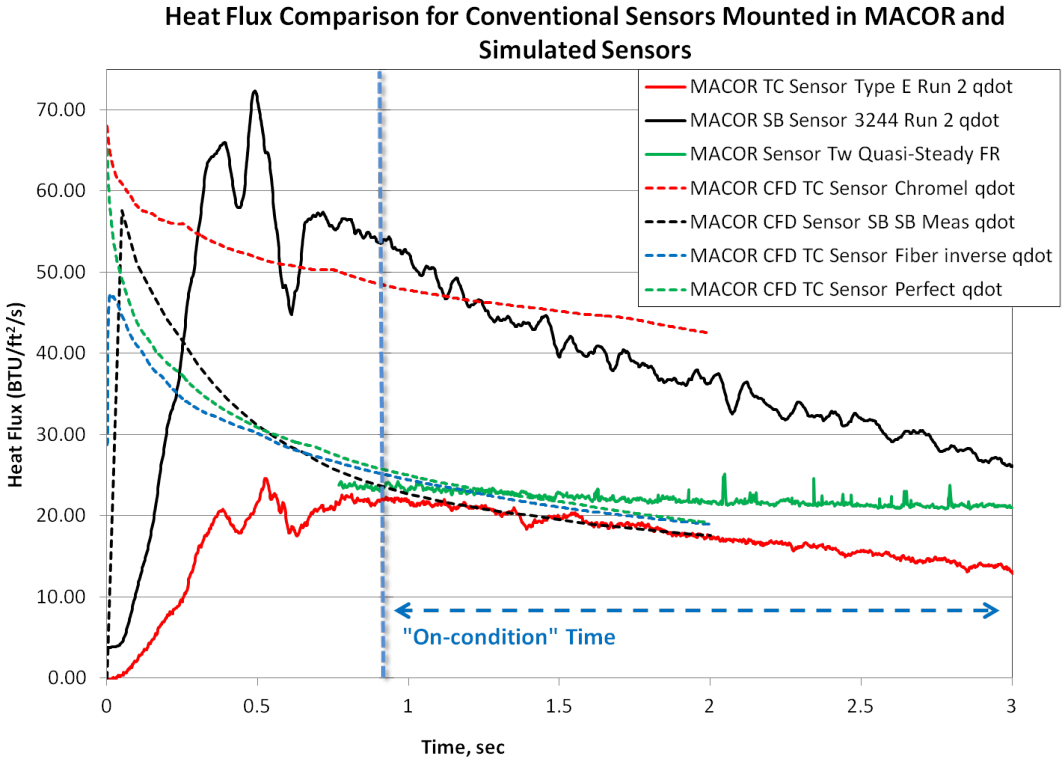

Figure 6-4. MACOR® model heat flux comparison VTHST to CFD with CHT.

Figure 6-4 presents two interesting results. The first is that the Schmidt-Boelter gage is capable of measuring accurate heat flux in MACOR® if it is installed extremely well. Secondly, as expected a fiber optic temperature sensor would accurately predict heat flux in MACOR® using an inverse heat flux calculation if the assumptions for the calculation hold.

6.3 Graphite Hemisphere Comparison

Figure 6-5 is the temperature plot of all the real and modeled sensors in their Graphite hemispheres. Both of the real sensors in the VTHST wind tunnel runs read significantly higher than the simulated sensors. Much of this discrepancy is likely due to the geometry differences between the simulated runs and the real ones. One of the biggest geometry changes is the effect of the stainless cylinder the Graphite hemisphere sits in in the wind tunnel runs. Because the simulation does not have that feature, the thermal energy is quickly conducted away from the surface. It is also of note that the modeled fiber optic sensor shown with the blue dashed line has the same stagnation temperature as the modeled perfect graphite sensor with the green dashed line.

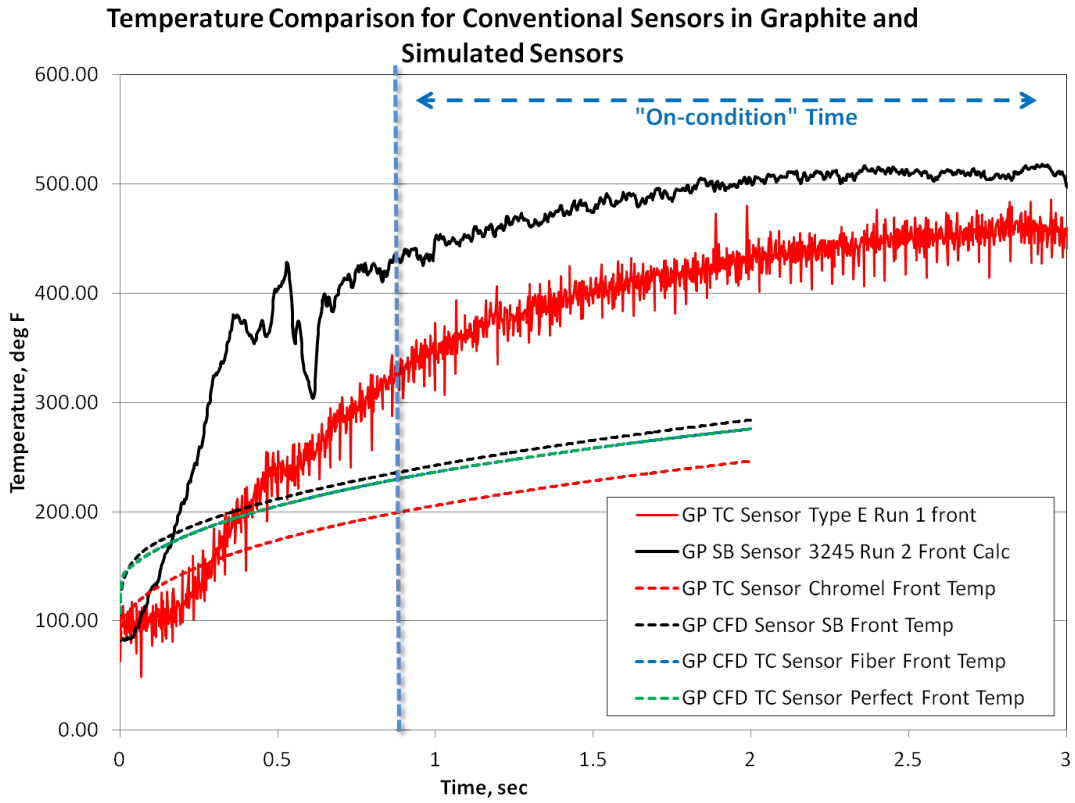

Figure 6-5. Graphite model temperature comparison VTHST to CFD with CHT.

Figure 6-6 is the heat flux plot of all the real and modeled sensors in their Graphite hemispheres. The Schmidt-Boelter gage does appear to be measuring a heat flux close to the modeled perfect graphite heat flux output within the uncertainty of 13.18%, but due to the improper slope, it is most likely a false promise. Again, it is of note that the "measured" heat flux from the modeled Schmidt-Boelter gage is well within the 13.18% uncertainty of the heat flux measurements when compared to the modeled perfect Graphite hemisphere.

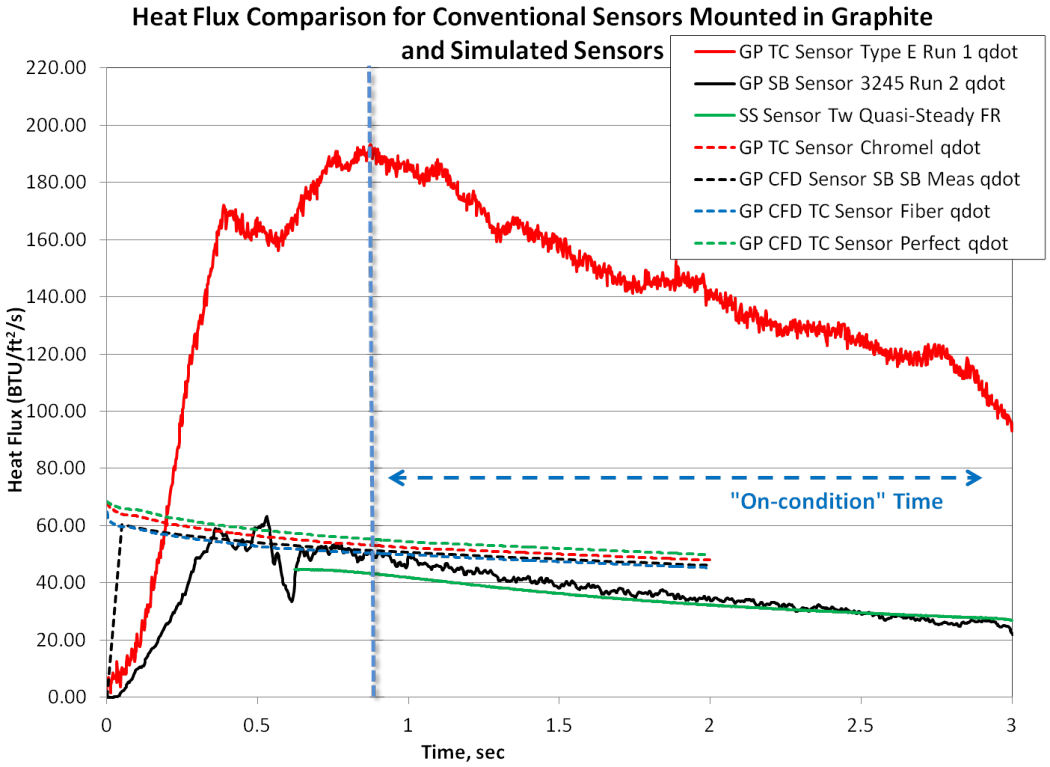

Figure 6-6. Graphite model heat flux comparison VTHST to CFD with CHT.

7. Discussion

Note that the various plots in this chapter are repeated plots from earlier chapters illustrated again for ease of reference.

7.1 Results

This study was envisioned to first illustrate the effects of test article/sensor material matching on heat flux measurement techniques. A direct and indirect heat flux sensor that are materially matched to stainless steel were tested in a similar model material and also two model materials at opposite ends of the thermal property spectrum. Due to the material mismatch, these differences were expected to have shown in a Schmidt-Boelter gage that read high in MACOR® and low in Graphite due to the correspondingly higher or lower temperature of the surroundings. This is in spite of the physics of this condition which dictate a lower stagnation heat flux for the cooler graphite hemisphere compared to the higher stagnation heat flux of the hotter MACOR® hemisphere. In fact Figure 7-1 illustrates the original hypothesis with caveats.

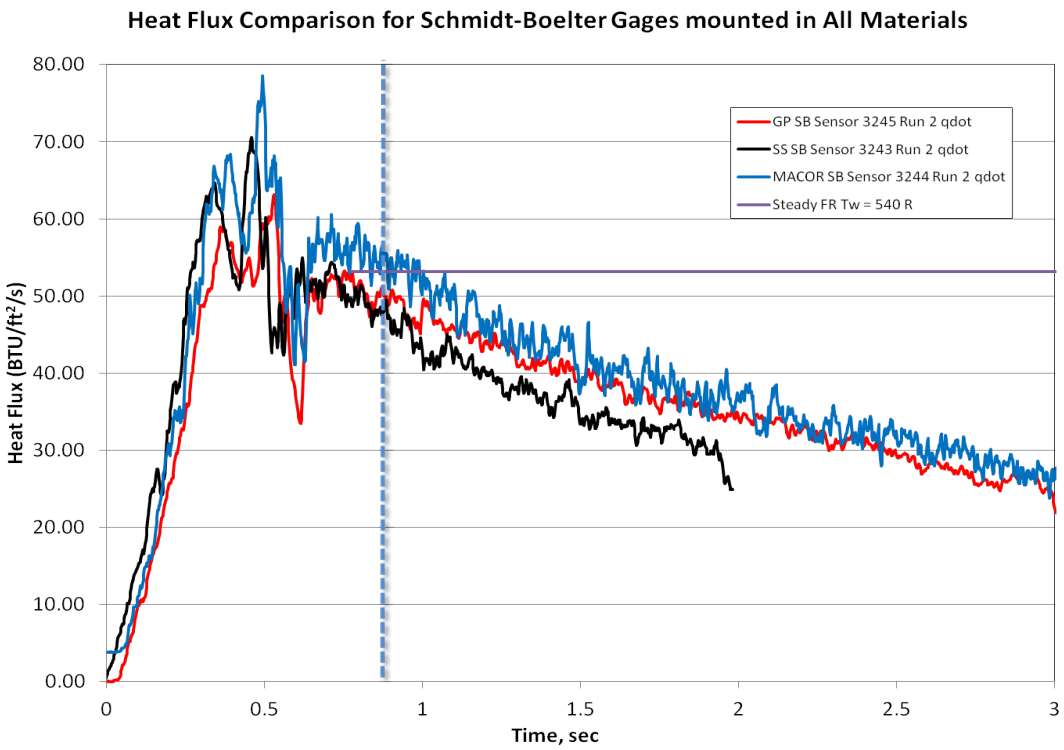

Figure 7-1. Schmidt-Boelter gage heat flux comparison across different model materials.

Figure 7-2 shows the temperatures for the three Schmidt-Boelter gages and verifies the hypothesis. But, it also shows that the model internal geometry has a very important effect. The heat flux measured by the Schmidt-Boelter gage in graphite is the same or greater than in the stainless steel version. The reason is shown by the rapid rise of the backface temperature in the graphite sensor and by the fact that the backface of the hemisphere is increasing in temperature before the beginning of the on-condition run in the graphite hemisphere, shown in Figure 7-2.

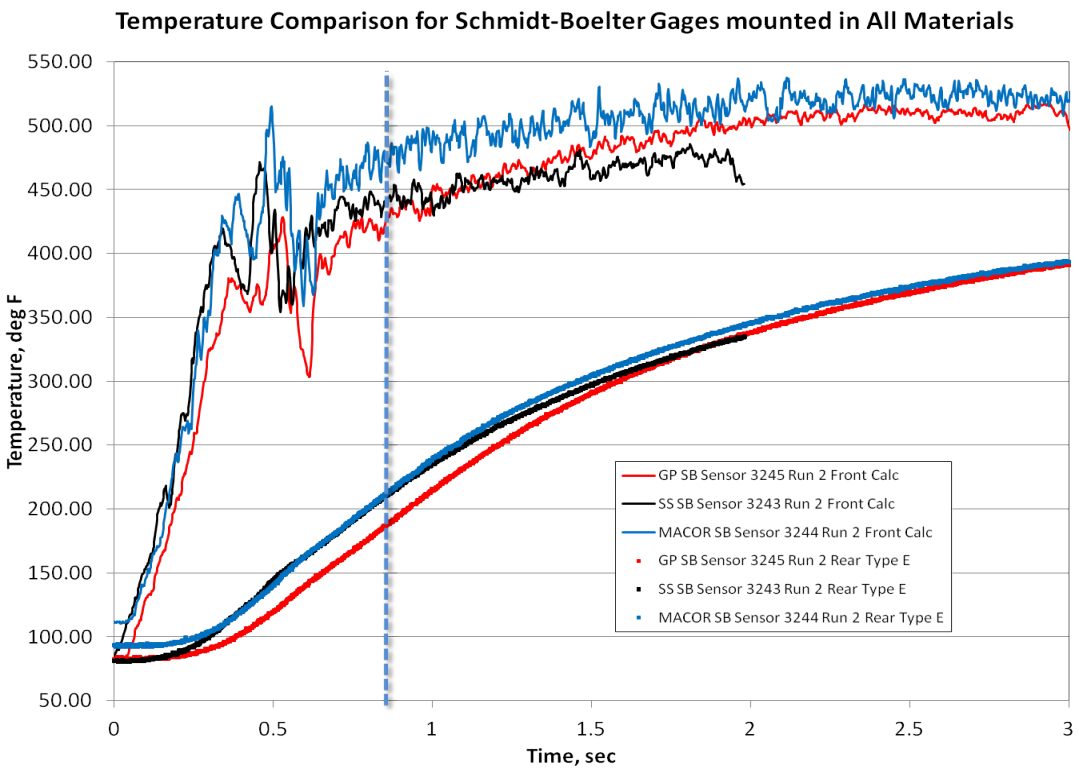

Figure 7-2. Schmidt-Boelter gage temperature comparison across different model materials.

This study used calibration in the test articles as a way to compare the sensors in their housing in a controlled environment. But, the calibration was a radiative environment with close to uniform heat flux spatially. The wind tunnel is a transient, spatially non-uniform, convective heat flux environment. The magnitude of these effects is seen in a comparison of Table 7-1 to Figure 7-1. While the Schmidt-Boelter gages performed extremely well in all test article materials during calibration, Figure 7-1 shows that they did not fare as well in the wind tunnel. Because of the wall temperature changes, the heat flux is greatest for the graphite hemispheres and lowest for the MACOR® in the wind tunnel. The measured data from the wind tunnel runs showed the opposite trend because of the material mismatch in a non-uniform heat flux environment, spatially and temporally.

Hemisphere Material	Measured Value	Difference from Calibration Gauges	Lamp Variation from Setting	Manufacturer's Uncertainty
	BTU/ft^2/s	%	%	%
Stainless Steel 3 BTU	2.9533	1.07%	2.09%	3.00%
MACOR 3 BTU	2.88822	-1.16%	-1.16%	3.00%
Graphite 3 BTU	2.90177	-0.70%	-0.92%	3.00%
Stainless Steel 12 BTU	12.0993	1.73%	0.73%	3.00%
MACOR 12 BTU	11.7068	-1.57%	-0.50%	3.00%
Graphite 12 BTU	11.9776	0.71%	-0.22%	3.00%

Table 7-1. Results for Schmidt-Boelter gages in all materials during static calibration at 3 and 12 BTU/ft^2/s.

The specific shape of both the object being measured, as well as that of the heat flux profile, has profound effects on the outcome of the measurements. Figure 7-3 shows that the planar assumption in the inverse method for heat flux calculation can radically change the answer given the correct environment. The differences between the planar and spherical inverse methods document the difference in an environment where the heat flux is near constant in time and in a planar dimension. When the inverse heat flux method was varied from planar to spherical and semi-infinite to finite in the VTHST as shown in Figure 7-4, the results were not promising. In fact, the heat flux environment combined was too non-linear spatially to be resolved with any one-dimensional inverse heat flux calculation. In an aerospace environment, the heat flux would rarely be constant in time, and almost never in space.

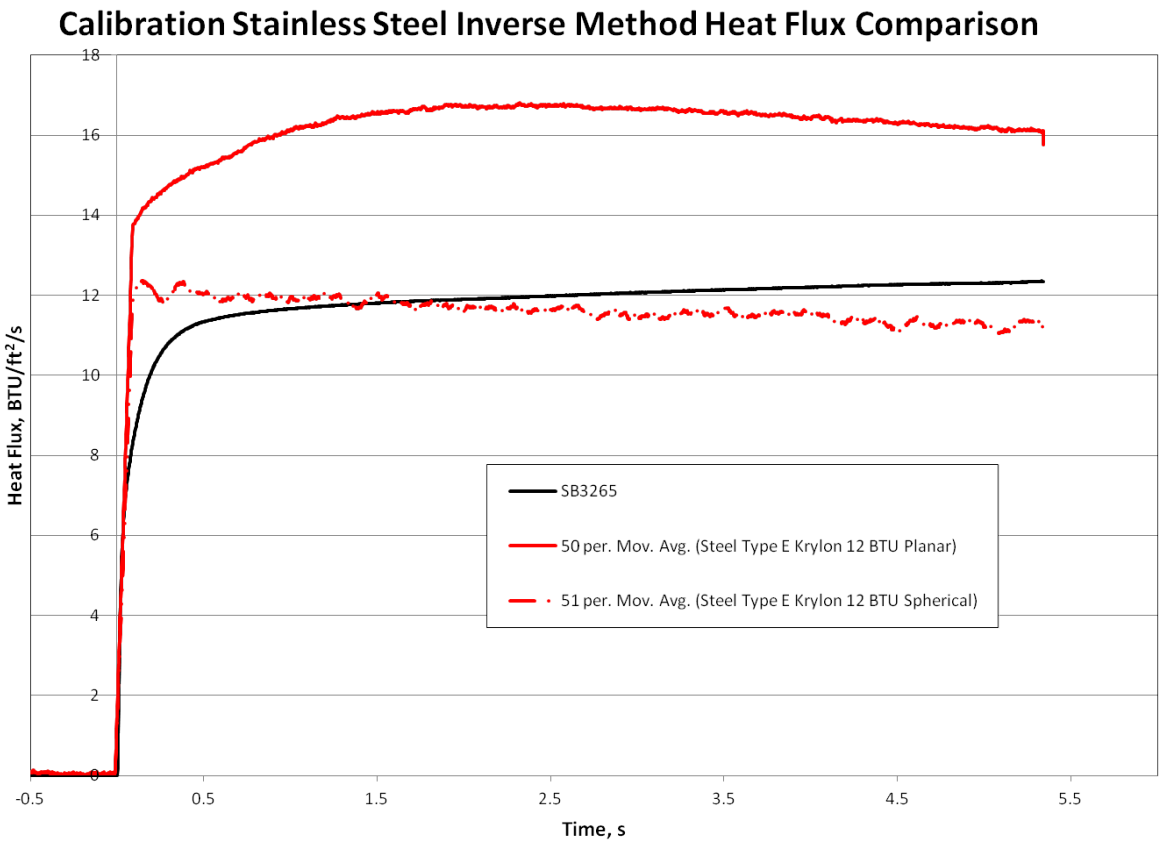

Figure 7-3. Temperature results for all materials during calibration at 12 BTU/ft^2/s.

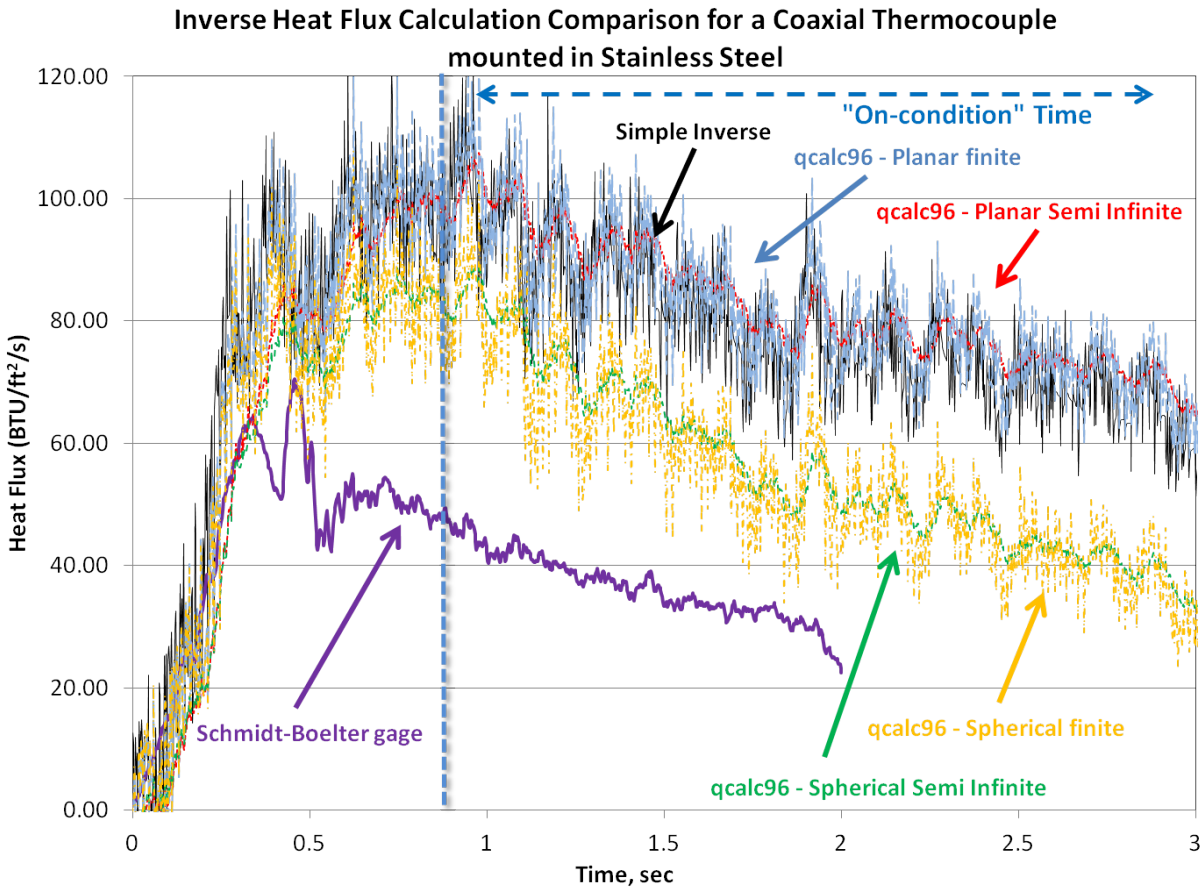

Figure 7-4. Spherical and Planar, Semi-infinite and finite inverse heat flux method comparison for the MedTherm coaxial thermocouple in a stainless steel hemisphere.

The wind tunnel proved that a thermal contact and thermal resistance can overwhelm material matching and test article thermal properties as shown in Figure 7-5. More illustrative though is Figure 7-6 showing the temperatures of the coaxial thermocouples in all materials.

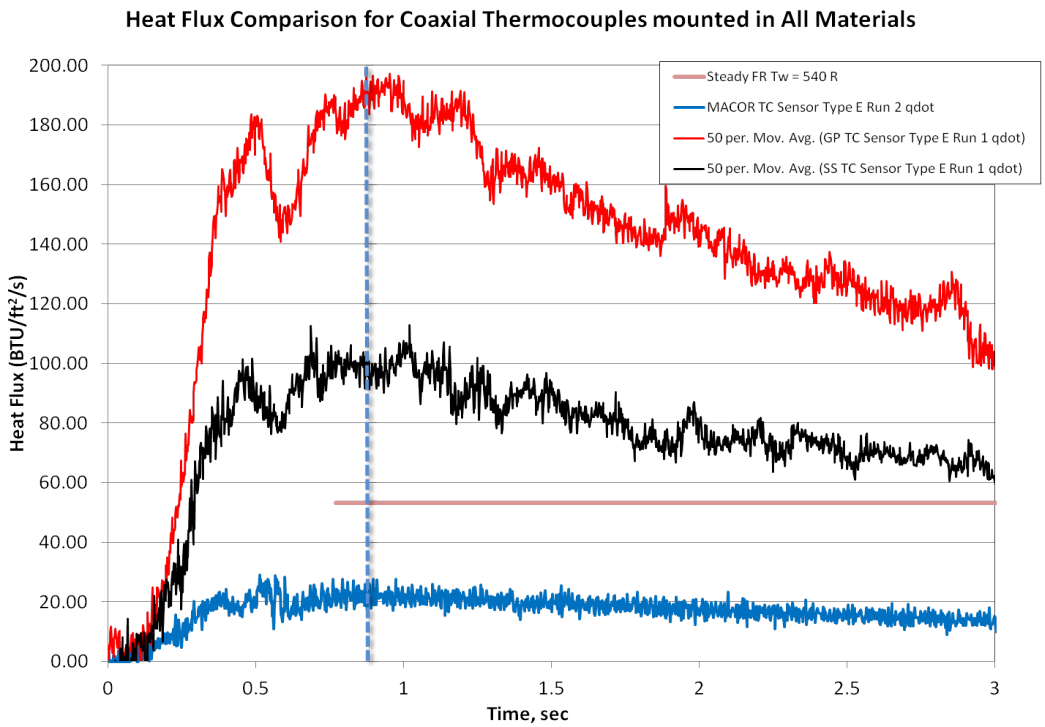

Figure 7-5. Coaxial thermocouple heat flux comparison across different model materials.

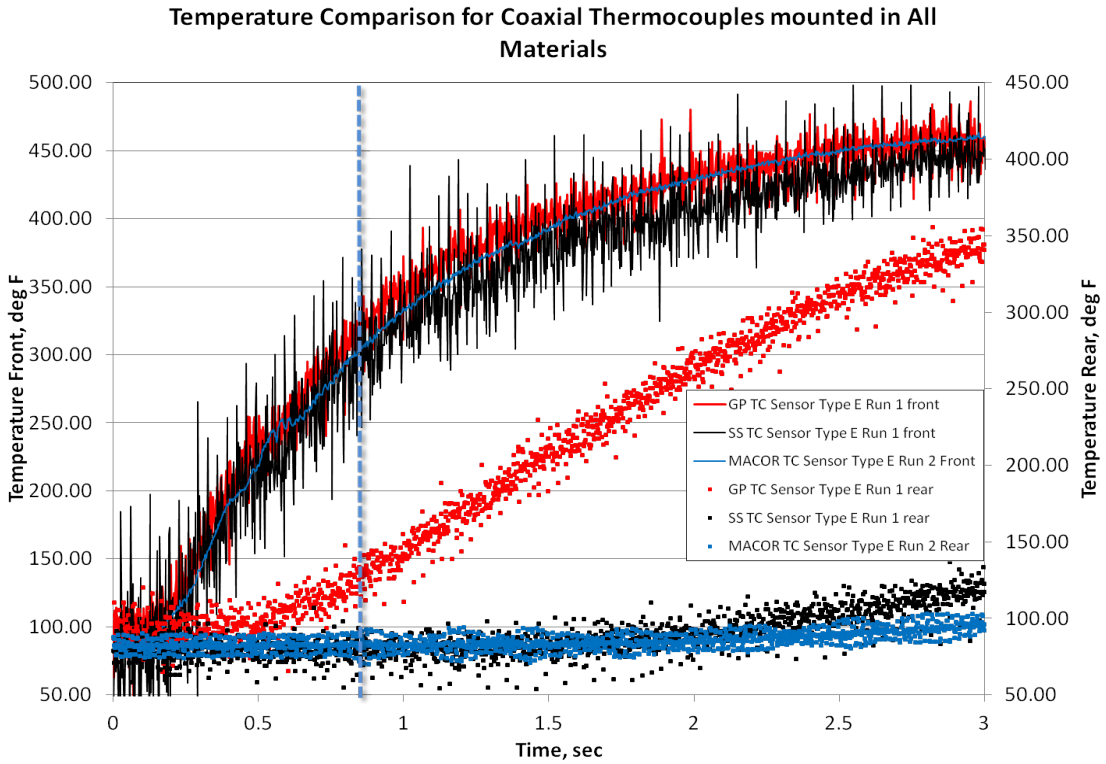

Figure 7-6. Coaxial thermocouple temperature comparison across different model materials.

In fact, the stagnation point temperature measured in each of the hemispheres was the same based on these different sensor outputs in extremely different materials. This means that not only is shape a concern, but thermal contact. These sensors were assembled in their housings by the same technicians that build the Schmidt-Boelter gages. The adhesive was wicked into the front of the sensor, and then the rear was potted to seal the sensor to the hemisphere fully. Yet, the thermal contact was apparently bad enough that the stagnation point was isolated from the surrounding material. This means that the differences in the inverse method calculations were solely based on the material properties used in the inverse method calculation itself. Furthermore, the rise in the temperature of the backface that happens so rapidly in the graphite hemisphere does not have the impact it should with non-perfect thermal contact. Added into the complexity of the thermal contact discussion is the fact that the Krylon® 1602 applied during calibration remained on the hemispheres into the wind tunnel tests. This paint did have an effect on the thermal contact, but the amount was not quantifiable.

Figure 7-1 and Figure 7-7 illustrate the same trend with the modeled and real Schmidt-Boelter gages. Even though the real Schmidt-Boelter gages performed well in the calibration as shown by Table 7-1, they did not accurately measure the heat flux on the hemisphere in the VTHST. The modeled Schmidt-Boelter gages were within the uncertainty of the measurement for all three materials. The results from the real Schmidt-Boelter gages are clearly an instance of poor thermal contact between the sensor and the test article.

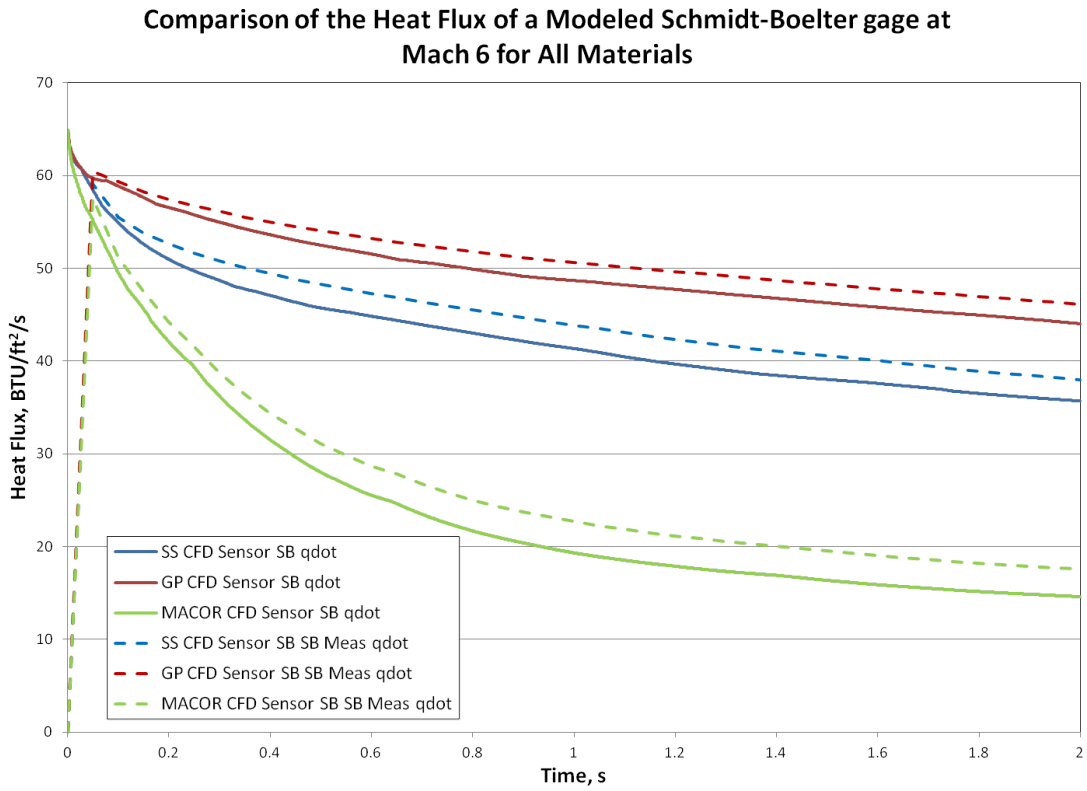

Figure 7-7. Simulated Mach 6 wind tunnel run heat flux profile for a modeled Schmidt-Boelter gage with different model materials.

More interestingly as shown in Figure 7-7, even though the Schmidt-Boelter gage was designed for stainless steel, its inherent design is to be isolated from the material, but to have global properties and thermal behavior similar to a slug of stainless steel. The isolated feature allowed the modeled Schmidt-Boelter gage to accurately measure heat flux in all materials even when the stagnation temperature of the modeled sensor was a factor of two higher than that of the modeled hemisphere without a sensor.

8. Conclusions

The initial goal of this study was to more thoroughly document the effects of material matching in various test environments. While the importance of proper material matching in thermal instrumentation, to include measurement of heat flux, can not be overstated, it is by no means the only consideration for accurate measurement of heat flux. In fact, many of the other issues can keep a properly matched heat flux sensor from measuring even close to the correct heat flux.

Due to the small scales present in many parts present on hypersonic test articles, model geometry has clearly always been a concern. In this study, the effects of internal and external model geometry on the accuracy of heat flux calibration and measurements were documented in multiple test and simulation environments.

When determining the heat flux instrumentation for a thermal study, adequate care needs to be used determining the spatial and temporal thermal environment before a single sensor is chosen. These variations can affect the accuracy of heat flux calibration and measurements no matter which type of sensor, direct or indirect, is used.

The overwhelming issue, if present, in the thermal instrumentation of a test article is thermal contact between sensor and test article. Without proper thermal contact the thermal resistance will completely change the measured heat flux. Part of the issue is how hard it is to diagnose the level of thermal contact so that it can be taken into account. Even when the other issues are solved, poor thermal contact will results in an invalid measurement.

Based on the simulations, a fiber optic thermocouple would be better than any of the other tested sensors at measuring the surface temperature of a MACOR®, or other

ceramic, test article. The advantages beyond the thermal properties similar to a ceramic include the extremely small size, very fast response, and high temperature capability.

Lastly, computer simulation is invaluable for sensor design and application. Much of the physics can not be separated in an experimental situation to determine the percentage of the overall effect. By using computer modeling, many of the issues above could be tested independently allowing for more insight into the actual heat transfer physics, and documenting problems such as thermal contact that would only have been hypotheses without the simulation.

In order to properly instrument an aerospace vehicle to determine heat flux, all of the above problems need to be addressed, and computer modeling should be relied upon heavily. No longer is material matching the only concern. The shape of the surface and the expected heat flux profile can vastly change the results and whether or not the measured or computed heat flux truly corresponds to the real value. While direct measurement methods can overcome some of the assumptions required for inverse methods, this study has proven that even a direct measurement technique like a Schmidt-Boelter sensor cannot measure heat flux correctly when the thermal contact is not good enough.

8.1 Future Work

This study has answered documented the phenomena that create heat flux measurement error, but it has also created new questions about heat flux measurement that are answered by theory and hypotheses for now. A more in-depth CFD study with the goal of accurately modeling contact resistance and subsurface geometry should be undertaken. Future work in this area should include wind tunnel testing with various hemisphere diameters to allow for heat flux that varies less along the radius. Real time surface temperature measurement using a high-speed infrared camera could also be used to compare the temperature on the surface of the hemisphere to the sensor temperature and

output. Further work into understanding which heat flux environments are ideal of r one-dimensional heat flux calculations should be undertaken. Most of all further, simulation should be used to try and ascertain the basic phenomena that are causing the various effects.

A. Appendix A: Uncertainty Analysis

The various uncertainties for the sensors and methods used in the test contribute to an overall uncertainty for the experiments in this study. An uncertainty analysis was performed to document the contribution of the various pieces to the overall experimental uncertainty. This analysis looks at the HST flow conditions uncertainly, the calculated inverse heat flux uncertainty, and the uncertainty of the analytic Fay-Riddell solution. Table A-1 lists the various pressure, temperature, and heat-flux sensors used in the VTHST. The uncertainty values for the individual sensors are from the manufacturers data, or in the case of the AEDC Schmidt-Boelter gages, from uncertainty studies on the sensors themselves[19]. In all cases this uncertainty analysis assumes a 95% confidence level which means that 95% of the measurements for any given value would fall within the calculated uncertainties.

Measurement	Parameter	Range/Thermocouple Type	Accuracy	Manufacturer
HST Plenum Pressure	$p_{0\infty}/p_{01}$	0-1500 psi	+/- 0.08% (+/- 1.2 psi)	Omega
Hemisphere Mount Stagnation Pressure Probe	p_{02}	0-100 psi	+/- 0.25% (+/- 0.25 psi)	Omega
Hemisphere Mount Stagnation Temperature Probe	$T_{0\infty}/T_{01}/T_{02}$	Type E	+/- 1 K	Omega
Hemisphere Coaxial Thermocouple	T_w	Type K	+/- 1.1 K	MedTherm
Hemisphere Coaxial Thermocouple	T_w	Dual Type E	+/- 1 K	MedTherm
Hemisphere Schmidt-Boelter Gage	q_w''/T_{w2}	3-100 BTU/ft^2/s (Over Temp failure, not q_w'')/Type E	+/- 3% (+/- 0.25 psi)	AEDC ATM Lab

Table A-1. Sensors used in the VTHST.

The technique used in this study to determine the uncertainties is described by Doebelin[31] as the root-sum-square formula. In the following sections the measurements that contribute to each global uncertainty are discussed and then combined as shown in the following equation:

$$U_{val} = \left(\left(\frac{\partial(\mathrm{val})}{\partial(\mathrm{x_1})} \delta(\mathrm{x_1}) \right)^2 + \left(\frac{\partial(\mathrm{val})}{\partial(\mathrm{x_2})} \delta(\mathrm{x_2}) \right)^2 + \cdots + \left(\frac{\partial(\mathrm{val})}{\partial(\mathrm{x_n})} \delta(\mathrm{x_n}) \right)^2 \right)^{1/2} \quad \text{(A.1)}$$

In this equation *val* is the desired quantity, U_{val} is the uncertainty of that quantity, and the various *x*s are the measurements that are part of *val*'s calculation. If *val* is a simple equations such as:

$$val = \mathrm{x^2 y + z^3} \quad \text{(A.2)}$$

The partial derivatives can be analytically derived. The $\delta(x_n)$ in equation 1 is the 95% uncertainty of the individual x_n measurement. Given the above example for *val* in equation A.2, a corresponding analytic expression for the uncertainty can be written:

$$U_{val} = \sqrt{(2\mathrm{xy}\delta x)^2 + (\mathrm{x^2}\delta y)^2 + (3\mathrm{z^2}\delta z)^2} \quad \text{(A.3)}$$

In cases where the partial derivatives cannot be analytically derived, a jitter analysis was used to calculate the partial derivative using an approximate numerical derivative[31].

In order to take into account the unsteady fluctuations in the measurements, the uncertainty of all of the measured flow variables was calculated using a combination of the manufacturer's uncertainty, and the unsteady fluctuations in the measured quantity. First the instantaneous uncertainty was calculated using equation A.4.

$$\delta x_i = \sqrt{(\delta_f x_i)^2 + (\delta_c x_i)^2} \quad \text{(A.4)}$$

In this case the *i* subscript is instantaneous, the *c* is the given value from the factory, and the *f* is the fluctuation uncertainty. The fluctuation value is equal to two standard deviations of the fluctuating property. Equation A.5 then shows how the instantaneous uncertainty is turned into an average uncertainty.

$$\delta\bar{x} = \frac{\delta x_i}{\sqrt{N}} \tag{A.5}$$

In equation A.5, N is the number of independent samples and is the minimum of the number of samples taken or the total sampling time divided by the integral time step, τ_m, as shown in equation A.6.

$$N = \min\left(\#\ of\ Samples, \frac{\Delta t_{sample}}{\tau_m}\right) \tag{A.6}$$

In this uncertainty analysis, the average uncertainty for all measured properties was calculated and is shown in Table A-2.

Measurement	Parameter	Average Uncertainty
HST Plenum Pressure	$p_{0\infty}/p_{01}$	0.56 psi
Hemisphere Mount Stagnation Pressure Probe	p_{02}	0.86 psi
Hemisphere Mount Stagnation Temperature Probe	$T_{0\infty}/T_{01}/T_{02}$	1.07° R
Hemisphere Coaxial Thermocouple	T_w	4.71° R
Hemisphere Schmidt-Boelter Gage	q_w''/T_{w2}	0.52 BTU/ft^2/s

Table A-2. Average uncertainty calculated for this study.

A.1 Flow Conditions Uncertainty

Three measurements were made in order to verify the conditions within the test section of the wind tunnel. The first condition was the stagnation temperature measured behind a normal shock on the total temperature probe of the VTHST test fixture as shown in Figure 2-5. This measurement was only used in the quasi-steady Fay-Riddell analytic calculations[33]. The uncertainty of the total temperature is calculated using the average uncertainty calculation documented above and is shown in Table A-2, 1.07° R, which is an uncertainty of 0.1%.

The Mach number for the wind tunnel runs was calculated by the ratio of total pressures, p_{02}/p_{01}, measured by the plenum pressure transducer and the Pitot probe pressure transducer of the VTHST test fixture as shown in Figure 2-5. The uncertainty of this ratio is calculated analytically using the following equation:

$$U_{\frac{p_{02}}{p_{01}}} = \sqrt{\left(\frac{d\frac{p_{02}}{p_{01}}}{dp_{01}}\delta\bar{p}_{01}\right)^2 + \left(\frac{d\frac{p_{02}}{p_{01}}}{dp_{02}}\delta\bar{p}_{02}\right)^2} \tag{A.7}$$

When the individual average sensor uncertainties were substituted in the total pressure ratio, the uncertainty was found to be 2.44%. From there the uncertainty on the calculation of the freestream Mach number was calculated using the average uncertainties for the plenum and Pitot tube pressure transducers. Equation 8 is the uncertainty for the calculation of Mach number. The third variable in the calculation is γ, the ratio of specific heats. Because this wind tunnel is on the edge of a perfect/imperfect gas condition as discussed in the experimental set-up, the uncertainty for γ is the percentage difference between the nominal assumed ratio of specific heats of 1.4, and the ratio of specific heats calculated assuming a vibrational heat capacity contribution. This yields an uncertainty of 4%.

$$U_M = \sqrt{\left(\frac{dM}{d\gamma}\delta\bar{p}_{01}\right)^2 + \left(\frac{dM}{dp_{02}}\delta\bar{p}_{02}\right)^2 + \left(\frac{dM}{d\gamma}\delta\gamma\right)^2} \tag{A.8}$$

When substituted into equation A.8 the uncertainty in the measurement of Mach number was found to be 4.53%. The uncertainties are illustrated in Figure A-1.

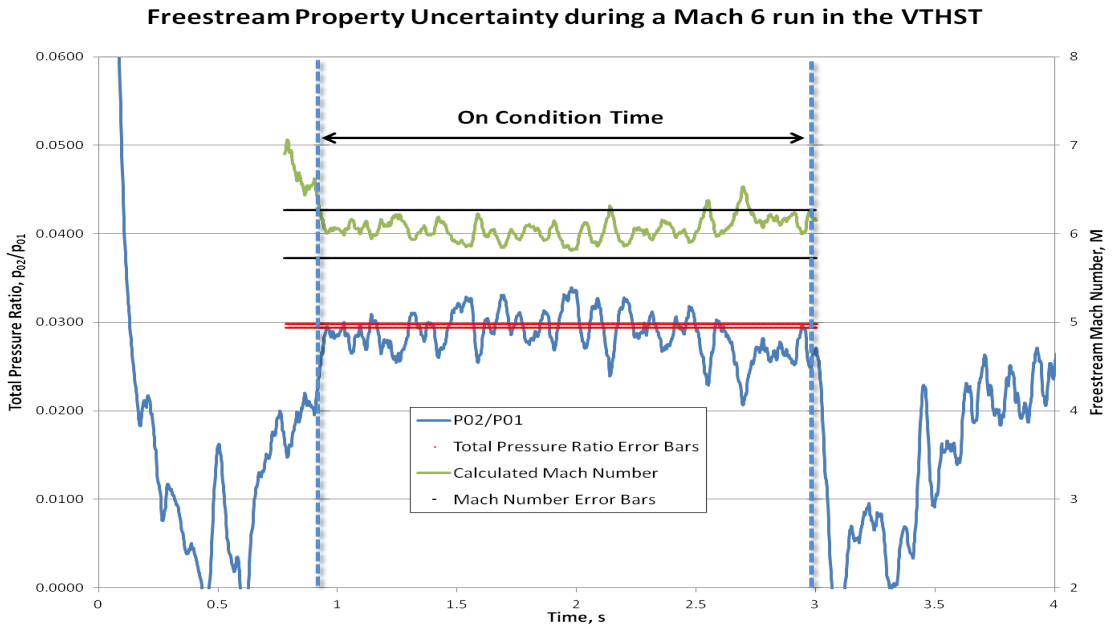

Figure A-1. Uncertainty of Flow properties during a VTHST Run at M = 6.

A.2 Inverse Method Heat Flux Prediction Uncertainty

In order to calculate the heat flux using temperature as a function of time, it is necessary to measure the wall temperature, T_w, and time step, Δt, accurately. The thermo-physical properties, ρ, c_p, and k, of the solid must be known as well. The uncertainty of these properties is assumed to be 10% based on Creel's work NASA Langley[37]. The following equation shows the contributions of the various parts to the inverse heat flux prediction uncertainty:

$$U_{q_w''} = \left(\left(\frac{dq_w''}{dT_w}\delta\bar{T}_w\right)^2 + \left(\frac{dq_w''}{d\Delta t}\delta\Delta t\right)^2 + \left(\frac{dq_w''}{d\rho}\delta\rho\right)^2 + \left(\frac{dq_w''}{dc_p}\delta c_p\right)^2 + \left(\frac{dq_w''}{dk}\delta k\right)^2 \right)^{1/2} \quad \text{(A.9)}$$

With the various pieces, the inverse heat flux data reduction code. An initial calculation of the heat flux for a wind tunnel run was made using the data for a MACOR® hemisphere with a coaxial thermocouple. Then, each of the properties was varied independently by 1% and the new heat flux was calculated. Once all modified runs were

calculated, the numerical derivatives could be calculated and then substituted into equation A.9. For the inverse heat flux calculations, the uncertainty was found to be 9.84%. If the uncertainty on the thermo-physical properties can be reduced to 5% by further testing of the actual materials at various temperatures and curve matching of property changes with high heat flux, the uncertainty would drop to 6.33%.

A.2.1 Inverse Heat Flux Data Reduction Code Validation

To verify the accuracy of the inverse heat flux data reduction code, the code was given $T_w(t)$ for a constant 1-D, heat flux into a semi-infinite solid (304SS) at a starting condition of 370° F which roughly corresponds to the temperature of the stainless steel hemisphere wall at the beginning of the on-condition time in a Mach 6 run. Equation A.10 calculates the wall temperature as a function of time for a given constant heat flux on a semi-infinite wall[38].

$$T_w = 2q_w{}'' \frac{\sqrt{\frac{\alpha(t - t_0)}{\pi}}}{k} + T_{w_i} \tag{A.10}$$

When the corresponding temperature profiles for two conditions heat flux settings were reduced in the inverse heat flux data reduction code, the code properly calculated the heat flux. Figure A-2 shows the input temperature and output heat flux for a q_w'' = 50 BTU/ft^2/s and 25 BTU/ft^2/s. Based on this study the inverse heat flux code was assumed to have no error as long as the assumptions used in its creation are valid.

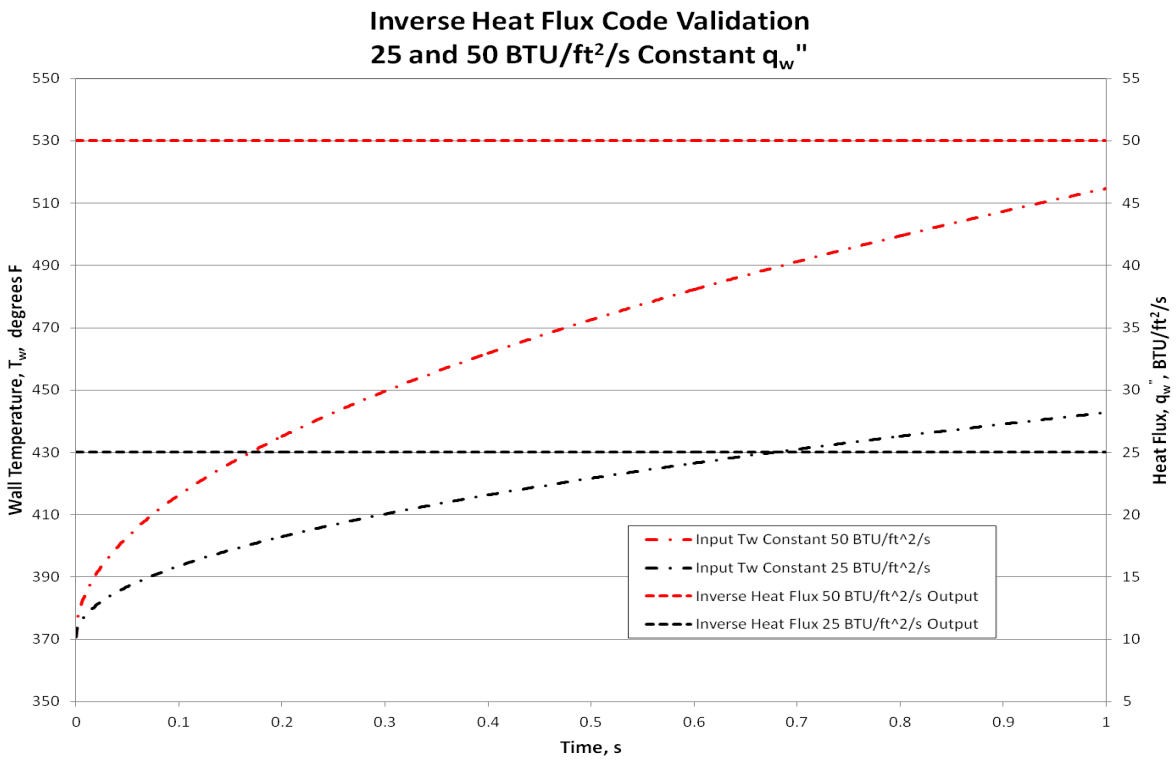

Figure A-2. Inverse Heat Flux Code Validation Plot.

A.3 Fay-Riddell Analytic Calculation Uncertainty

For calculations involving the quasi-steady analytic method, Fay-Riddell[33], as shown in the analytic set-up section, the uncertainty involved many pieces. The calculation of the heat flux at the stagnation point of a hypersonic hemisphere required the freestream total pressure, p_{01}, the freestream total temperature, T_{01}, the wall temperature, T_w, the ratio of specific heats, γ, the freestream Mach number, M_1, and the radius of the hemisphere, r. All other properties were calculated from these properties or generated from empirical data via these properties. The freestream total pressure, total temperature, and hemisphere wall temperature have uncertainties based on Table A-2. The uncertainty of the ratio of specific heats was again assumed to be the 2.2% as referenced in section A.1. The uncertainty for the freestream Mach number was also from the freestream uncertainty calculations and was found to be 4.53%. Lastly, the uncertainty for the radius was the tolerance from the Virginia Tech Shop for the hemispheres which was 0.001 in. Again using a jitter analysis to calculate the numerical partial derivatives, these values

were substituted into equation A.11. The uncertainty on the quasi-steady analytic method was found to be 13.14%.

$$U_{q_w{}''} = \left(\left(\frac{dq_w{}''}{dp_{01}} \delta\bar{\mathrm{p}}_{01}\right)^2 + \left(\frac{dq_w{}''}{dT_{01}} \delta\overline{\mathrm{T}}_{01}\right)^2 + \left(\frac{dq_w{}''}{dT_w} \delta\overline{\mathrm{T}}_w\right)^2 + \left(\frac{dq_w{}''}{d\gamma} \delta\gamma\right)^2 + \left(\frac{dq_w{}''}{dM} \delta\mathrm{M}\right)^2 + \left(\frac{dq_w{}''}{dr} \delta\mathrm{r}\right)^2 \right)^{1/2} \tag{A.11}$$

A.4 Heat Flux Measurement Uncertainty

When the heat flux for a given flow condition is measures, the uncertainty is a combination of the uncertainty of the flow condition and the uncertainty of the measured heat flux. This uncertainty is similar to the uncertainty for the Fay-Riddell calculation, but added in is the measurement uncertainty. For Schmidt-Boelter gage measurements, $q_{w_{SB}}{}''$, the uncertainty comes from Table A-2. For the coaxial thermocouples, $q_{w_{In}}{}''$, the uncertainty is folded in from the uncertainty of the inverse heat flux calculation from section A.2, 9.84%. As in the section A.3, the freestream total pressure and temperature have uncertainties based on Table A-2. The uncertainty of the ratio of specific heats was again assumed to be the 2.2% as referenced in section A.1. The uncertainty for the freestream Mach number was also from the freestream uncertainty calculations and was 4.53%. Lastly, the uncertainty for the radius was the tolerance from the Virginia Tech Shop for the hemispheres which was 0.001 in.. Again using a jitter analysis to calculate the numerical partial derivatives, these values were substituted into equation A.12 and A.13. The uncertainty on the measured heat flux values using the Schmidt-Boelter Gages was found to be 13.18% and using the combination of the coaxial thermocouple and the inverse heat flux method[9] was found to be 16.41%. Figure A-3 shows the calculated uncertainty on a plot of heat flux in the stainless steel hemispheres.

$$U_{q_{w_m}{}''} = \left(\left(\frac{dq_{w_m}{}''}{dp_{01}} \delta\bar{\mathrm{p}}_{01}\right)^2 + \left(\frac{dq_{w_m}{}''}{dT_{01}} \delta\overline{\mathrm{T}}_{01}\right)^2 + \left(\frac{dq_{w_m}{}''}{dT_w} \delta\overline{\mathrm{T}}_w\right)^2 + \left(\frac{dq_{w_m}{}''}{d\gamma} \delta\gamma\right)^2 + \left(\frac{dq_{w_m}{}''}{dM} \delta\mathrm{M}\right)^2 + \left(\frac{dq_{w_m}{}''}{dr} \delta\mathrm{r}\right)^2 + \left(\frac{dq_{w_m}{}''}{dq_{w_{SB}}{}''} \delta q_{w_{SB}}{}''\right)^2 \right)^{1/2} \tag{A.12}$$

$$U_{q_{wm}}{}'' = \left(\left(\frac{dq_{w_m}{}''}{dp_{01}}\delta\bar{p}_{01}\right)^2 + \left(\frac{dq_{w_m}{}''}{dT_{01}}\delta\bar{T}_{01}\right)^2 + \left(\frac{dq_{w_m}{}''}{dT_w}\delta\bar{T}_w\right)^2 + \left(\frac{dq_{w_m}{}''}{d\gamma}\delta\gamma\right)^2 \right. \\ \left. + \left(\frac{dq_{w_m}{}''}{dM}\delta M\right)^2 + \left(\frac{dq_{w_m}{}''}{dr}\delta r\right)^2 + \left(\frac{dq_{w_m}{}''}{dq_{w_{In}}{}''}\delta q_{w_{In}}{}''\right)^2 \right)^{1/2} \quad \text{(A.13)}$$

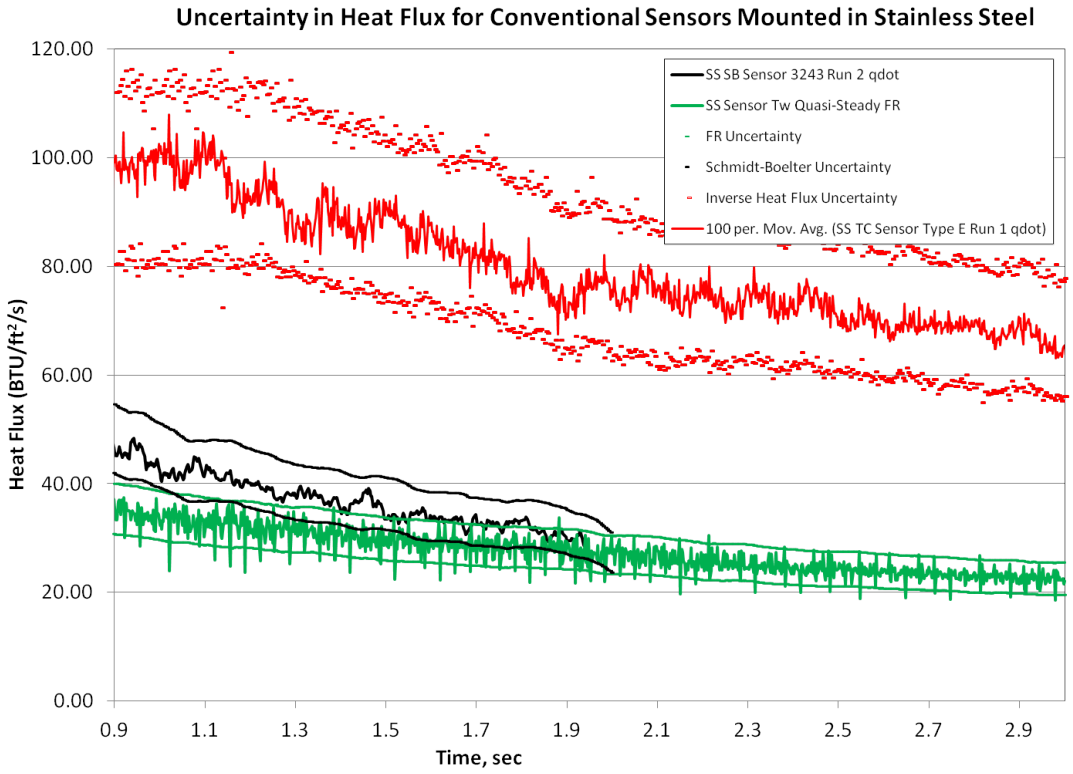

Figure A-3. Uncertainty in the heat flux data and calculations for the stainless steel hemispheres.

Table A-3 summarizes the uncertainties for this study.

Measurement	Parameter	Uncertainty
Flow Total Pressure Ratio	p_{02}/p_{01}	2.44%
Flow Mach Number	M_∞	4.53%
Inverse Heat Flux Calculation	q_w''	9.84%
Fay-Riddell Calculation	q_w''	13.14%
Schmidt-Boelter Gage Heat Flux	q_{wSB}''	13.18%
Coaxial Thermocouple Inverse Heat Flux	q_{wIn}''	16.41%

Table A-3. Calculated uncertainties for this study.

References

[1] T. E. Diller, "Heat Flux," in *The Measurement, Instrumentation and Sensors Handbook*, J. G. Webster, Ed., Boca Raton, Florida, CRC Press, 1999, pp. 34.1-15.

[2] B. Vick, ME 3304 Heat and Mass Transfer Course Notes, Blacksburg, VA: Virginia Tech, 2010.

[3] J. A. Schetz, Boundary Layer Analysis, New Jersey: Prentice Hall, 1993.

[4] D. O. Hubble and T. E. Diller, "A Hybrid Method for Measuring Heat Flux," *ASME Journal of Heat Transfer,* vol. 132, pp. 031602.1-8, 2010.

[5] C. T. Kidd and J. C. Adams, "Development of a Heat-Flux Sensor for Commonality of Measurement in AEDC Hypersonic Wind Tunnels," in *AIAA Paper No. 2000-2514*, 2000.

[6] W. J. Cook and E. M. Felderman, "Reduction of data from thin film heat-transfer gages: a concise numerical technique," *AIAA Lounal,* vol. 4, pp. 561-562, 1966.

[7] P. J. Seymour, Techniques for Numerical Evaluation of Unsteady Heat Flux from Thin Film Gauges, Buffalo, NY: State University of New York at Buffalo, 1987.

[8] D. G. Walker and E. P. Scott, "Evaluation of Estimation Methods for High Unsteady Heat Fluxes from Surface Measurements," *Journal of Thermophysics and Heat Transfer,* vol. 12, no. 4, pp. 543-551, 1998.

[9] D. G. Walker and E. P. Scott, "One Dimensional High Heat Flux Estimation from Discrete Temperature Measurements," *ASME 1995 International Congress and Symposium,* Vols. 317-1, p. 175, 1995.

[10] R. D. Neumann, "Special Course on Aerothermodynamics of Hypersonic Vehicles," AGARD R-761, Neuilly Sur Seine, France, 1989.

[11] R. D. Neumann, "Thermal Instrumentation A State-of-the-Art Review," Wright Labs, WR-TR-96-2107, WPAFB, 1996.

[12] R. D. Neumann, P. J. Erbland and L. O. Kretz, "Instrumentation of Hypersonic Structures A Review of Past Applications and Needs of the Future," in *AIAA Paper No. 88-2612*, 1988.

[13] T. E. Diller, "Advances in Heat Flux Measurement," *Advances in Heat Transfer,* vol. 23, pp. 279-368, 1993.

[14] P. R. Childs, J. R. Greenwood and A. C. Long, "Heat Flux Measurement Techniques," *Proceedings of the Institute of Mechanical Engineers,* vol. 213, no. C, pp. 655-677, 1999.

[15] D. L. Schultz and T. V. Jones, "Heat Transfer Measurement in Short Duration Facilities," AGARD AG-165, London, 1973.

[16] J. J. Singh and R. R. Antcliff, "Measurement Technology forAerospace Applications in High Temperature Environments," in *NASA Conference Publication 3161*, Hampton, VA, 1992.

[17] T. E. Diller and C. T. Kidd, "Evaluation of Numerical Methods for Determining Heat Flux with a Null Point Calorimeter," in *Proceedings of the 42nd International Instrumentation Symposium, ISA*, Research Triangle Park, NC, 1997.

[18] J. J. Coblish, S. M. Coulter and J. D. Norris, "Aerothermal Measurement Improvements

using Coaxial Thermocouples at AEDC Hypervelocity Wind Tunnel No. 9," in *AIAA 2007-1467*, 2000.

[19] C. T. Kidd, "Determination of the Uncertainty of Experimental Heat-Flux Calibrations," AEDC Technical Report 83-13, Arnold AFB, TN., 1983.

[20] C. T. Kidd and W. T. Scott, "New Techniques for Transient Heat-Transfer Measurement in Hypersonic Flow at the AEDC," in *AIAA 99-0823*, 1999.

[21] S. Stefanescu, R. G. DeAnna and M. Mehregany, "Experimental Performance of a Micromachined Heat Flux Sensor," in *AIAA 97-3034*, 1997.

[22] C. G. Miller III, "Comparison of Thin-Film Resistance Heat-Transfer Gages With Thin-Skin Transient Calorimeter Gages in Conventional Hypersonic Wind Tunnels," NASA Technical Memorandum 83197, Hampton, VA, 1981.

[23] American Society for Testing and Materials, "Standard Test Method for Measuring Extreme Heat-Transfer Rates from High-Energy Environments Using a Transient, Null-Point Calorimeter," *ASTM,* vol. E 598, no. 77, pp. 491-497, 1990.

[24] J. J. Bezuidenhout, J. A. Schetz and D. G. Walker, "Heat Flux Determination Using Surface and Backface Temperature Histories and Inverse Methods," in *AIAA 2001-3530*, 2001.

[25] R. S. Fielder and K. L. Stinson-Bagby, "High-Temperature Fiber Optic Sensors for Harsh Environment Applications," *Industrial and Highway Sensors Technology,* vol. Proceedings of SPIE 5272, pp. 190-196, 2004.

[26] T. M. Hightower, R. A. Olivares and D. Philippidis, "Thermal Capacitance (Slug) Calorimeter Theory Including Heat Losses and Other Decaying Processes," NASA Technical Memorandum 2008-215364, Moffett Field, CA, 2008.

[27] M. N. Inci, S. R. Kidd, J. S. Barton and J. D. Jones, "High Temperature Miniature Fiber Optic Interferometric Thermal Sensors," *Measurement Science and Technology,* vol. 4, pp. 382-387, 1993.

[28] S. R. Kidd, J. S. Barton, J. D. Jones and K. S. Chana, "Heat Flux and Unsteady Temperature Measurements in Turbomachinery Using Miniature Fiber Optic Interferometers," *International Society for Optics and Photonics,* vol. 2005, pp. 570-581, 1993.

[29] M. J. Tonks, Modeling and Testing of Fast Response, Fiber-Optic Temperature Sensors, Blacksburg, VA: Virginia Polytechnic Institute and State University, 2006.

[30] Y. Zhu, Miniature Fiber-Optic Sensors for High-Temperature Harsh Environments, Blacksburg, VA: Virginia Polytechnic Institute and State University, 2007.

[31] E. O. Doebelin, Measurement Systems Application and Design 5th ed., Boston: McGraw Hill, 2004.

[32] D. M. Bourg, Excel Scientific and Engineering Cookbook, 1st Ed., Beijing: O'Reilly Media, Inc., 2006.

[33] F. M. White, Viscous Fluid Flow, 2nd Ed., Boston: McGraw Hill, 1991.

[34] C. A. Rock, Experimental Studies of Injector Array Configurations for Circular Scramjet Combustors, Blacksburg, VA: Virginia Polytechnic Institute and State University, 2010.

[35] AMES Research Staff, "NACA Report 1135," AMES Aeronautical Laboratory, 1953.

[36] R. Neel, A. Godrey and W. McGrory, "Low-Speed, Time-Accurate Validation of GASP Version 4," in *AIAA Paper No. 2005-0686*, 2005.

[37] T. R. Creel, "A Device for Rapid Determination of Thermophysical Properties of Phase-Change Wind Tunnel Models," NASA Technical Memorandum X3421, Hampton, VA, 1976.

[38] J. P. Holman, Heat Transfer, 6th ed., New York: McGraw-Hill, 1986.